3D Additive Manufacturing, Microstructure, and Mechanical Properties of High Performance Materials

January 2018

James Mutuku Mutua

Contents

Chapter 1 Introduction

1.1 Background review

3D printing, fundamentally known as additive manufacturing (AM) is a process where products are monotonically build layer by layer through computer aided controlled operations. A virtual model is first designed with suitable computer aided design (CAD) software, then translated into standard tessellation language (.stl) electronic data understandable by the printer. The electronic data is then used to control the motion and trajectory of the printing head fitted with focused heat source. This selectively melts and consolidates commonly used feedstock material (usually in powder or filament form) to create 3D parts. 3D printing provides real-time rapid prototyping of product models making it possible to visualize the design prior to actual production. It also eliminates trial and error, reduces cost and time implications during manufacturing process. These virtual manufacturing techniques speeds up design iterations and allow designers, researchers, and manufacturers to generate prototypes within the shortest time possible, obtain feedback and refine designs through early error detection and correction.

3D printed components offer a high degree of geometrical flexibility and accuracy without almost any loss of material. This leads to resource savings and eco-design optimization. This state-of-the-art manufacturing technology produce not only functional research prototypes in order to enhance product quality, process parameters, and material universalisation during design process but also full scale components for actual applications.

The history of additive manufacturing dates back to late 19^{th} century in the fields of topography and photo sculpture [1]. Although experiments occurred as far back as the 1960s in the photo-glyph recording technique that selectively exposed layers of a transparent photo emulsion while scanning cross sections of the object to be replicated [2], it was not until 1983 when pioneers Charles Hull (founder of 3D Systems) and Scott Crump (founder of Stratasys)

developed modern day range of technologies now known as 3D printing [3]. They worked on additive processes such as Stereolithography (SLA) and selective laser sintering (SLS) that created solid objects layer by layer using 3D CAD data and ultra violet light to cure photo polymeric resins. As the processes evolved, they became known as additive manufacturing (AM) [4]. Additive manufacturing began with limited set of processes and materials with a primary goal of producing prototypes. However, the early 1990s saw an era of spontaneous emergence of new AM technologies and materials. Fast forward to date, sophisticated AM technologies have been developed and extensive research on materials is being conducted [5]. In addition, the focus has shifted from prototyping to fabrication of full scale functional parts [1]. Fig. 1.1 illustrates the progressive developments in AM technologies and materials that have taken place through time.

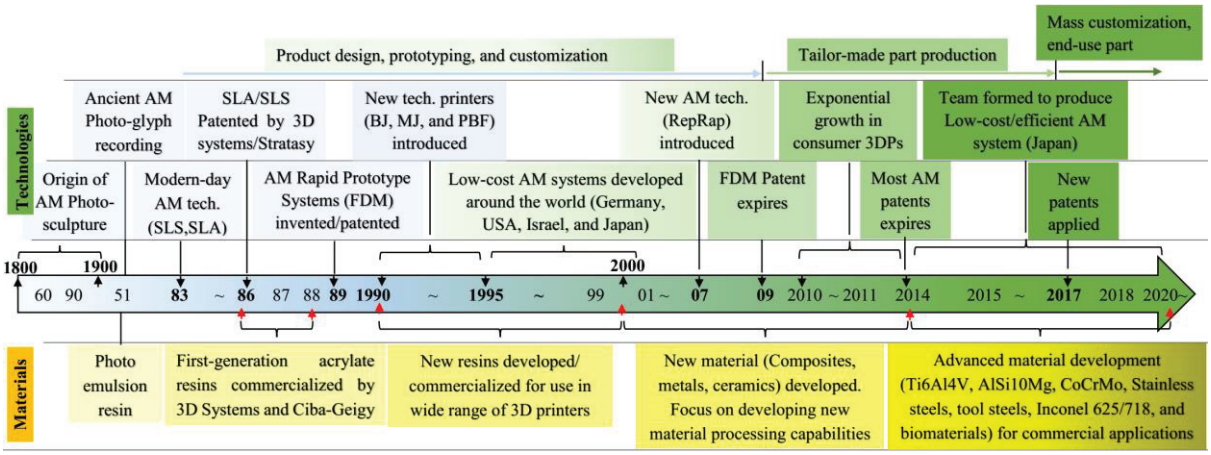

Fig. 1.1 Progressive development in AM technologies and material.

Additive manufacturing has been categorized into seven broad techniques depending on the nature and aggregate level of feedstock material as well as the binding mechanism between joined layers [6]. For the past three decades, establishment and advancements in these techniques relied heavily on curiosity and inventiveness rather than problem-solving [7].

VAT photopolymerization is the oldest of all AM processes where an ultraviolet (UV) light is used to selectively cure a vat of liquid photopolymer resin layer by layer. The UV light is moved on the X-Y plane (using motor controlled mirrors) chemically hardening the resin onto a build platform. The substrate is then lowered a specified z distance and a new layer is cured. This process is repeated one cross-section at a time until the 3D part is completed. The vat is then drained and the model removed [4, 8]. Support structures may at times be necessary and are therefore added to provide support to thin sections and overhangs during the process. Post processing curing is done to instil high level accuracy, good surface finish, and necessary strength on the parts for structural applications.

In Material jetting method, droplets of liquid monomers are selectively deposited layer after layer generating 3D objects. Material is jetted from a thermally or piezoelectrically heated print head onto a build platform using either a continuous or drop on demand (DOD) approach. Using photopolymer material for building and waxes for support, 3D structures are created and exposed to UV light for curing [9-11]. Since material must be deposited in drops, the number of materials available for use is limited. Photopolymers and waxes are suitable and commonly used materials, owing to their viscous nature and ability to form drops. However, dedicated research on ceramics and metals has been carried out as they are more promising for future applications [12-15]. Through this process, high accuracy parts with multi-colour schemes can be produced using multiple materials in a single part.

The binder jetting process uses a set of nozzles to systematically print liquid bonding agents between and within powder layers to create 3D parts. Normally, the process starts by spreading a thin layer of metal or ceramic powder on the build platform followed by selective deposition of the binder material as dictated by the CAD model to form the first layer. This process is repeated until the entire part is completed. In addition, post-processing of the green 3D part is mandatory [16] where curing, de-powdering, sintering, infiltration, heat treatment

and finishing operations are carried out to instil superior mechanical properties on the finished part [17]. As the build part lie on the loose powder bed, binder jetted 3D parts can be produced without support structures. However, a major drawback to this process is the prolonged post-processing times which may incur significant costs and delays in delivery of parts [18]. Specific binder jetting processes include polyjet, smooth curvature printing, and multi-jet modeling. Typical materials used in this processes are powdered plastics, metal, ceramics, glass, and sand.

Another key AM process is the material extrusion method. In this technique, a thermoplastic material (filament) is constantly fed through a heated nozzle or orifice, melted and extruded in tracks or beads which combine to form a layer. As the material solidifies, the build platform moves down and the nozzle traverses the x and y axes depositing additional layers to create multi-layer models [4, 10]. This is the most commonly used AM technique for making research/design models, domestic and consumer products [7-11]. However, its adoption in fabricating functional prototypes is limited due to the inferior mechanical properties of the materials. Fused deposition modelling (FDM) and fused filament fabrication (FFF) are commonly used material extrusion processes [17]. See Fig. 1.2 for the schematic illustration of material extrusion process.

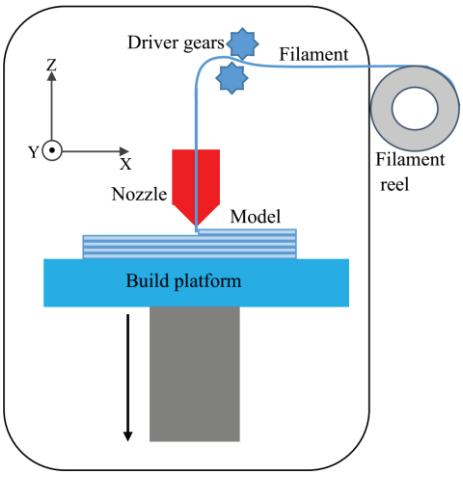

Fig 1.2 Material extrusion process.

The powder bed fusion (PBF) process use either laser or electron beam to melt and consolidate material powder together layer by layer [4, 18]. In all PBF processes, the powder is uniformly spread on a substrate and high power laser or electron beam directed thereby selectively sintering the powder into a layer. The build platform is moved a unit layer distance downwards and more powder fed from replenishing reservoirs or hoppers, spread using rollers or squeegeeing blades and the process of selective sintering repeated [4, 6, 9], see Fig. 1.3. Loose and un-sintered powder material is used to support the object being produced, thus reducing the need for support systems. After the process, the excess/residue powder is recovered and recycled back to the system for utilization. Examples of PBF processes are direct metal laser sintering (DMLS), electron beam melting (EBM), selective heat sintering (SHS), selective laser melting (SLM) and selective laser sintering (SLS) [9, 11, 19, 20]. Of these processes, selective laser melting (SLM) and electron beam melting (EBM) are the most popular for additive manufacture of metals and ceramics [6]. These methods have been very instrumental in fabricating fully functional parts for aerospace, medical, automobile applications, and prototypes among other products for in-house use [3].

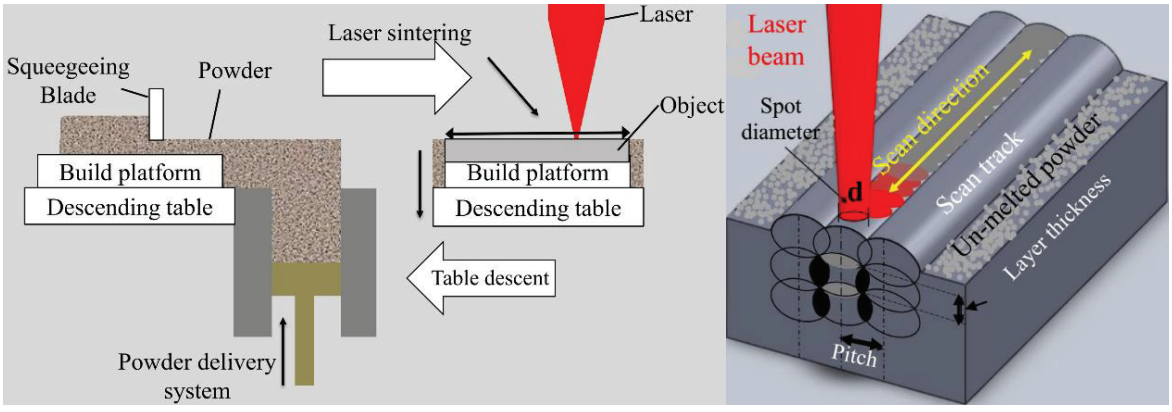

Fig. 1.3 Schematic overview of the select laser melting process both at machine and powder scales.

Direct energy deposition process is another laser based AM process where metallic material usually in powder or wire form is melted with a laser or other energy source and simultaneously deposited. This process is similar to material-extrusion except that, the nozzle is mounted on a multi-axis arm that can move in multiple directions melting and depositing the wire or powder feed material onto a part. Direct energy deposition processes include laser engineered net shaping (LENS), directed light fabrication (DLF), direct metal deposition (DMD), 3D laser cladding. They are used primarily to add features to an existing structure (such as adding strengthening ribs onto a plate) or for repair of damaged or worn parts [4, 10].

The sheet lamination method is a three-step AM process where a laminate is placed on a substrate, bonded by heated rollers to form a layer, and then cut according to slice contour. Then another sheet of laminate material is placed over previous layer and bonded. After each layer bonding, a laser or knife continuously cuts the border around the desired part and excess material is removed [4]. This process is repeated until the part is completed. Examples of sheet lamination technologies include laminated object manufacture (LOM), selective deposition lamination (SDL), and ultrasonic additive manufacturing (UAM). Typical materials used in these processes are plastic sheets, paper, and metal foils.

The hybrid system is an AM technique in which either selective laser melting (a form of PBF) or laser metal deposition (a form of DED) is combined with CNC machining, which allows additive manufacturing and subtractive machining to be performed in a single machine to fabricate 3D part [21]. This system utilizes the strength of both AM and subtractive processes to minimize post-processing operations such as machining. The process is associated with excellent surface finish and accurate dimension of the final parts. An example of hybrid system currently in use is metal laser sintering hybrid machining (MLSHM).

The current demand in customized intricate parts, reduced product cycle times, and cost has given impetus to the recent exponential growth in AM technologies. Recent studies by

Wohler associates in *Wohler's report 2017* indicate that, AM industry grew by 17.4% in worldwide revenues, for a total of $6.063 billion [22]. Although this growth was slightly lower compared to an increase of 25.9% in 2015, vibrant activities in the AM industry were recorded. For example, 97 manufacturers sold AM systems in 2016 – an increase from 62 in 2015 and 49 in 2014 [22, 23]. This positive trend was expected to continue in the future.

As mentioned in the different categories of AM processes, a wide variety of material is available for AM technologies. These includes polymers, metals, ceramics, and composites [24]. From the statistics on AM service providers [22], as indicated in Fig. 1.4, polymers are the dominant materials providing half of material requirement in AM applications. Clearly, nearly half of 3D printing service providers are now offering metal additive manufacturing capabilities. One of the reason for such a trend is the heightened shift of AM focus to generate fully functional parts.

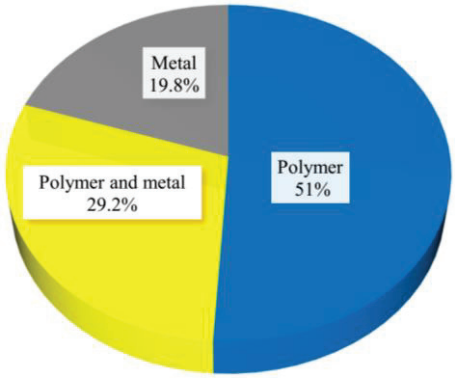

Fig. 1.4 Chart showing material utilization in AM processes. *Source: Wohlers Report 2017*.

These materials come in different states (resin, filament, pellets, granules, powder etc.) and have different properties. AM technology was first used to produce plastic prototypes from liquid photopolymer resins. Since then, the technology has advanced and become more capable of producing complex, near-net shaped objects from a wide variety of materials. As a

matter of fact, specific materials have been developed and used directly to make functional parts. However, there are as many materials for 3D printing as the number of 3D printer manufacturers [23]. This is due to competition and lack of standards governing 3D printing material development.

The success of additive manufacturing (AM) technologies in complementing conventional manufacturing processes is overwhelming. Numerous industrial sectors such as aerospace, automotive, medical, energy, and tool and die making have tapped into the imminent potential in AM technologies to produce geometrically complex parts [6]. Contrary to conventional manufacturing where parts are fabricated by subtracting material, AM processes fabricate parts by adding material layer by layer. This elicits remarkable reduction in production time and cost through reduced machine set-up and tooling, potential part count reduction, and associated assembly time reduction [25, 26]. AM processes were first limited to rapid manufacturing of prototypes and porous structures using polymer materials [27-30]. Ever since, the technology has seen tremendous breakthroughs and has risen through ranks; from making prototypes to parts with improved density, applications in making tool inserts, and conformal cooling channels [2, 6]. Currently, AM has ventured into the high-end applications (in aerospace and medicine) which demand the manufacture of reliably dense parts with a number of high-performance engineering materials such as steel, aluminium, titanium, CoCrMo alloys, and nickel-super alloys such as Inconel 625 and 718 etc. [6, 26, 31]. It is therefore crucial for the stakeholders in AM to have not only profound knowledge of the process itself, but also of the microstructure resulting from the process parameters and consequently of the properties of the manufactured parts [32]. Out of the numerous metal AM processes available [4, 11, 21], powder bed fusion (PBF) has the greatest potential in meeting the prevailing demand on end-use AM parts. Consequently, there has been more research in

PBF than any other metal AM processes [26]. However, FDM process remains indispensable in making prototypes for design visualization and is therefore being pursued to date [33].

In order to contribute positively to the ultimate understanding of the processing-structure-property-performance in AM processes, fused deposition modelling process and powder bed fusion process (specifically selective laser melting) were investigated in this study.

1.2 Fused deposition modelling (FDM)

This is one of the most frequently used additive manufacturing technology for fabricating thermoplastic parts that are mainly used as rapid prototypes for industrial purposes [33-36]. The interest in FDM has been fuelled by availability of a wide range of materials [8] (for example PLA, ABS, PEEK etc.), expired patents [23, 34], compact and cheap machines, and recyclability of FDM models [33, 36] making the whole process ecologically friendly. Just like any other AM process, FDM has the potential to save cost and time by saving costs on raw material and shortening the time from design to manufacture. Furthermore, with advancement in 3D FDM machines, this technique has become more promising in the manufacture of large customized end-use products [23]. However, some technicalities on the compatibility of presently available materials and a wide range of processing parameters have hindered full scale implementation of FDM technology. These limitations may be overcome by developing new materials with superior characteristics and highly compatible with this technology. Another convenient approach may be to suitably adjust the process parameters in order to improve the as-built part properties [35]. As the properties of FDMed parts depend to a large extend on the process parameter and partly on the materials used, there is a need for process parameter optimization from both technological and economic point of view [27] as well as material development and universalization.

Tensile strength and surface finish are the two main properties that dictate the engineering applications of FDMed parts. The strength of FDMed component primarily depends on five important process parameters. These are, layer thickness, building orientation, raster direction, raster to raster gap (air gap), and extrusion temperature [35]. As a consequence, many scientists have delved into optimization of these select process parameters in relation to a specific evaluation criterion, for instance surface quality, geometrical accuracy, processing time, repeatability, and mechanical properties [27, 33, 35-39]. To date, conclusive relations between FDM process parameters and part properties are not yet fully established. Even though extensive experimental determinations have been made, realization of full characteristics of these relations remains an open research problem [33]. This research sought to investigate and optimise select process parameters in order to contribute improved parts and resource-efficient FDM process.

1.3 Selective laser melting (SLM)

Selective laser melting (SLM) is one the leading powder based fusion additive manufacturing (AM) process where components are fabricated by fusing loose powder layer by layer. Through this process, near-net shape, geometrically complex parts with elaborate internal features can be produced at reduced time, cost, and inventories [5]. SLMed parts have similar or superior mechanical properties compared to those produced by conventional means. Moreover, SLM promotes the possibility of producing large customized products and is currently a promising technique to manufacture functionally graded multi-material parts [40]. The process allows the efficient use of material due to the possibility to recycle and reuse un-melted metal powder [6]. Unlike many other conventional manufacturing processes, SLM does not require specialized tooling and therefore, it is a convenient process for short production runs. This process has found a lot of applications in the automotive, aerospace,

medical, tool and die making industries [6, 18-20, 22]. A good example is in the aerospace industry where SLM has become an alternative to conventional machining of complex metallic parts whose “buy to fly ratio” is critical. In addition, lightweight components similar to cellular structures have been fabricated using SLM as an inspiration from natural systems. These cellular metal structures have been used in various industrial applications such as heat exchangers (in automotive and aerospace industries) owing to their valuable characteristics of low density, high strength, good energy absorption and good thermal properties [5].

To date, SLM is regarded as the most versatile AM process because of its ability to process virtually any material. Indeed, a wide spectrum of materials including Al-based alloys, Ti-based alloys, Fe-based alloys, Ni-based alloys, Co-based alloys, Cu-based alloys, and their composites have been processed using SLM [5, 18, 39, 41-43]. Moreover, previous studies also show that SLM is capable of producing amorphous materials because of the rapid cooling rates exhibited during the process [44, 45]. The surface integrity, microstructure, and mechanical properties of SLMed products have been shown to rely heavily on the process parameters during the process [18]. A plethora of process parameters including scan speed, laser power, hatch spacing, spot diameter, overlap rate, layer thickness, scan strategy, etc., provide a large process window for generating SLMed parts with a wide range of properties. However, these process parameters have to be carefully adjusted in order to fabricate defect-free parts [46].

Many approaches have been adopted towards optimal process parameters. For example, single track experiments performed by combining and controlling the process parameters to obtain suitable melt pool formation [47], and parts with maximum relative density [48]. In addition, design of experiment (DOE) methods, as well as simulation approach, has been used for the optimization process [49, 50]. However, two or more of these approaches must be used to increase the effectiveness of the optimization process.

1.4 Carbon fiber reinforced plastic composites in AM technology

Composites are often paraded as the materials of the future. Their strength properties offer an incredible advantage over any other material. Some leading composites that can be produced using AM technology include polymer matrix, metal matrix, ceramic matrix, fiber and particulate reinforced composites [24]. Their high strength and stiffness properties combined with low weight results in specific-strength and specific-stiffness several times greater than those of steel or aluminum. Therefore, offering an incredible advantage over most structural and sub-structural materials. Fiber reinforced composite is one of the most extensively used composite in the industry for high-performance applications [51]. Indeed, CFRP composites constitute about 50% of the material requirement during the construction of Boeing 787 [28, 52]. In addition, the material is at the forefront in the manufacture of Airbus A320 aircrafts and BMW i-series automobiles among others [28]. Among the numerous AM techniques, fused deposition modelling (FDM) and laminated object modelling (LOM) are the most suited AM methods used to process fiber reinforced composites. A pre-prepared mixture of proper material (usually carbon fiber in a determined matrix such as ABS, PLA, PC, PA etc.,) in filament form for FDM is extruded through a preheated nozzle layer after layer forming a 3D part, and in laminate form for LOM followed by laminate to laminate bonding up until a 3D part is generated. Fully functional carbon fiber 3D printers have been able to produce intricate, detailed, and strong parts greatly surpassing or matching the capabilities of conventionally manufactured counterparts at a reduced cost and at the same time allowing users to tailor their properties with entirely new carbon fiber reinforced polymer (CFRP) structures [28, 51]. However, the full potential in carbon fiber reinforced composites (such as cheap feedstock compared to costly powdered alloys used in some metal 3D printers, and much lower energy required to heat a thermoplastic or reactive

polymer than the energy required to fuse metals) is yet to be realized. This is due, in part, to limited investment in this area and overzealous concern in the inherent physical limitations associated with processing parameters. In addition, challenges of surface quality, strength and retaining the long or continuous fibers rather than short fibers in the matrix during AM processes have stalled the full implementation of additive manufacturing of fiber reinforced composites. Process parameter optimization has been proposed as a means of controlling the surface quality and strength of AM processed CFR composites. In addition, the problem of carbon fiber length reduction in the filament during production process has been counteracted by developing a big area additive manufacturing (BAAM) style printer that uses pellets as feedstock instead of a filament [28]. The composite industry is bound to gain most from the improvement of 3D printing technologies in order to meet the needs of high-performance industries. Indeed, optimization of process parameters especially in FDM of CFR-plastic composites will provide a pool of standardized information which will be vital in propelling the AM technology-CFRP material union as the future frontier in the manufacturing industry.

1.5 Steels in AM technology

Steel remains the dominant engineering material for structural and sub-structural applications [53]. Indeed, its unique versatility makes it inevitable in virtually every phase of our lives from housing, food supply and transport to energy delivery, machinery, and healthcare [54]. Their array of properties including high strength, corrosion resistance, good ductility, low cost, and recyclability etc., is due to existence of many grades of steels [6]. These properties have put steel in the forefront among other metal materials [24] in AM industry. Some leading grades of steel that have been processed using AM technologies include austenitic stainless steels, maraging steel, precipitation hardenable stainless steels, martensitic cutlery grade, and tool steels [6, 55-57]. Electron beam melting (EBM) and

selective laser melting (SLM) are the two leading metal AM techniques used to process steel materials. These techniques share the same approach where the starting point is a 3D CAD model which is virtually sliced into thin layers. Then based on this data, the physical part is built by repetitive deposition of single layer and locally melting of the powder material by a heat source.

Metal 3D printing of maraging steel and austenitic stainless steel has taken a leap into commercialisation at a fast rate. This is because the materials process relatively easily compared to others and due to the fact that SLM has the potential of producing no wastage during processing minimizing on cost. Besides, these alloys satisfy typical requirements of general-purpose applications, as well as increased requirements on strength and hardness, e.g. for die and tool applications [3]. On the one hand, the allotropy of iron based alloys in combination with the high temperature gradients involved in SLM offers the potential to generate unique microstructures which influence the resultant mechanical properties.
However, because of their nature and SLM process conditions, these alloy materials produce different phase compositions which must be carefully controlled to yield best mechanical properties. As such, process parameter optimization is necessary. Part of the current research focussed on investigating the process parameters and their influences on microstructure and mechanical properties of SLMed 18Ni (300-grade) maraging and SUS316L stainless steels.

1.6 Post heat treatment of additively manufactured (AMed) parts

Additively manufactured metal parts are characterized by unique microstructure due to the complex thermal cycles involving continuous re-heating of already solidified layers followed by rapid cooling. This often generates stresses that must be relieved after the process (SLM or LBM) is completed. In addition, an in-situ heat treatment occur which at times foster desired and/or undesired effects such as decomposition of brittle phases into

more ductile variants, segregation of alloying elements and grain growth [6]. The fine microstructure exhibited in as-built AM parts provide considerably high levels of strength and hardness [58] although undeniably inferior to heat treated conventionally manufactured counterparts. To optimise on the parts' performance, the microstructure and properties of the final part may however be adjusted in a wide range by a subsequent post process heat treatment. A series of heat treatments that SLMed parts may be subjected to include solution treatment, annealing, and precipitation hardening [24, 59]. Since the mechanical properties of AM parts depend partly on the densification levels and resultant microstructure, the combined effect of the densification behavior and post process heat treatment must be established if optimum mechanical properties are to be obtained. Previous studies show that, heat treatment alters the microstructure and hardness but has no measurable effect on the porosity in terms of pore quantity as well as size and shape [6, 59]. This is because, some material properties such as porosity and/or density are independent of any form of heat treatment and the only way to control them is by manipulating the process parameters. As this research focussed on optimizing the SLM process parameters, post process heat treatment remained an important component of the manufacturing process that was considered for all SLMed parts in order to instil better mechanical properties. The choice of the post process heat treatment adopted depended largely on the specific type of AM method and materials used, and the required mechanical property of the finished part.

1.7 Challenges facing AM technologies

Many researchers have reported machine, material, operations, and maintenance costs as the leading challenges towards the adoption of AM technologies [24, 60, 61]. Another shortfall of the technology is the scope of materials available or lack of universal material that can be used by all AM machines [61]. Indeed, each machine manufacturer has a specific

material for their machines [62, 63]. As such, material standardization has lagged behind. A glaring lack of standards for AM processes, machines, calibration, testing, and financial interest of machine manufacturers hinder the uptake of AM processes [60]. Many AM machine developers instituted bidding patents that restricted the improvement of existing machine technologies as well as development of new approaches to improve their performance [23]. Challenges of intellectual property rights infringement rose after the emergence of 3D printing marketplaces and downloadable open-source projects challenging the current legal landscape and social regulations that safeguard inventors against infringement. The inability of organizations and researchers to manufacture products that are consistent [61] across machines, operators, and manufacturing facilities has caused stagnation of the process. The existing AM systems are limited (the size of parts) to ‘‘in the box’’ manufacturing of parts. This makes it difficult to produce large components for aerospace, marine, and other industrial applications. Additional fundamental challenges are in material processing, the control of localized microstructure to instil requisite properties, attainment of fine feature size and dimensional tolerances, improved surface finish, and accelerating processing speed [7].

1.8 Problem statement

In as much as additive manufacturing technologies offers cost, material, and time saving opportunities over conventional manufacturing, and have a remarkable potential in the aerospace, automotive, and medical device markets to produce near-net-shape metallic components, it is not enough for the AMed 3D parts to have the same shape as conventionally fabricated ones. In these demanding applications, they must also have material properties that meet or exceed their conventionally processed counterparts. Therefore, AM process parameters and any subsequent thermal processing must be optimized

in order to obtain the required mechanical properties. In addition, there is also a demand to develop a better understanding of the basic physics of AM processes to capture the complexity in the multiple interacting physical phenomena [64]. A predictive triple helix (process-structure-property) relationship integrated with CAD, CAE, and CAM tools must be established [60]. Challenges of poor quality surfaces, residual stresses, uncontrolled localized composition and microstructure, failure to attain fine feature sizes and dimensional tolerances, and low processing speed have significantly hindered AM part property optimization, adoption and commercialization.

To exploit the unique AM characteristics and potential of producing epitaxial metallic structures, fabricating multiple and functionally graded materials, and embedded components during fabrication processes, a suitable processing window for the material and process must be established. However, such processing window is very wide [18, 55] making it difficult to optimise the processing conditions. In addition, each process, machine type and powder material potentially creates a new set of design rules and restrictions [62]. A one-size-fits all rule is yet to be arrived at, designers come to learn of the critical design-process rule while building a deliverable AM component [63].

To this end, understanding the effects of processing parameters on the microstructure evolution and mechanical properties during SLM has been the impetus of most research in AM technologies [26, 40-42, 47, 49, 55, 58]. However, there is limited literature on surface roughness and process parameter optimization on super alloys and Ni, Co rich alloy materials processed by laser sintering. In addition, a process map for SLMed maraging steel is yet to be established. As such, this study keenly investigated the influences of different processing parameters on CFR-ABS composite, and 18Ni (300-grade) maraging and SUS316L stainless steels respectively processed through FDM, and selective laser melting (SLM) with a view to optimise them. Thereafter, the optimized process parameter were used to generate a process

map for maraging steel and contribute new knowledge towards a comprehensive material property database and testing methodology on FDM and SLM as key AM processes.

1.9 Objectives of the study

The main objective of this study was to determine the effects of the various 3D printing process parameters on the quality of the product, and to identify the optimum process parameters and material properties during FDM of carbon fiber reinforced plastic composites and metal 3D printing of 18Ni (300-grade) maraging and SUS316L stainless steels.

To achieve this, the following specific objectives had to be accomplished.

1. Determine the effects of process parameters such as printing speed, layer thickness, and raster direction on the microstructure and mechanical properties of 3D printed CFR-ABS materials.
2. Determine the effects of laser power, scan speed, pitch, and spot diameter on the microstructure of 18Ni (300-grade) maraging steel and SUS316L stainless steel.
3. Determine optimum processing parameters that foster optimum relative density and microstructure for both maraging steel and SUS316L stainless steel.
4. Determine the optimum mechanical properties from the resultant optimum microstructure conditions that would give the material a near-net-shape and optimum performance characteristics during SLM.
5. Determine the optimum heat treatment conditions that would foster maximum mechanical properties for maraging steel.
6. Generate process maps for SLM of maraging and SUS316L steels.

1.10 Thesis outline

This research focused on 3D additive manufacturing and characterization of high-performance materials, and is organized in six Chapters.

In Chapter 1, the background of the current work and the literature which covers different additive manufacturing technologies, processes/methods, materials, challenges, and gaps have been discussed. In addition, clarifications on the context of this research and the objectives of the study have also been laid out.

The effects of process parameters on the microstructure and mechanical properties of CFR-plastic composites is fully described in Chapter 2.

Chapter 3 describes the process parameter optimization and the corresponding microstructure evolution, phase transformations, and mechanical property variations during SLM of 18Ni (300-grade) maraging steel with the optimized process parameters being summarized into a process map.

In order to improve the mechanical properties of the as-built SLMed maraging steel parts, Chapter 4 presents post process heat treatment processes and the corresponding microstructure evolution, phase transformations, hardness and mechanical property optimization.

Process parameter optimization and their effects on the microstructure, and mechanical properties of SLMed SUS316L stainless steel are fully described in Chapter 5. Furthermore, the corresponding optimized process parameters are summarized into a process map.

Finally, in Chapter 6, general conclusions and summary of the current work, recommendations for future work and some achievements pegged on this work are presented.

References

[1] Gao, W., Zhang, Y., Ramanujan, D., Ramani, K., Chen, Y., Williams, C.B., Wang, C.C., Shin, Y.C., Zhang, S. and Zavattieri, P.D., 2015. The status, challenges, and future of additive manufacturing in engineering. *Computer-Aided Design*, *69*, pp.65-89.

[2] Weber, C., Peña, V., Micali, M., Yglesias, E., Rood, S., Scott, J.A. and Lal, B., 2013. The role of the national science foundation in the origin and evolution of additive manufacturing in the United States. *Science & Technology Policy Institute*, *1*.

[3] Srinivasan, V. and Bassan, J., 2012. 3D printing and the future of manufacturing. In *CSC Leading Edge Forum*.

[4] Gibson, I., Rosen, D., and Stucker, B., 2014. Additive manufacturing technologies: 3D printing, rapid prototyping, and direct digital manufacturing. Springer.

[5] Manfredi, D., Calignano, F., Krishnan, M., Canali, R., Ambrosio, E.P., Biamino, S., Ugues, D., Pavese, M., and Fino, P., 2014. Additive manufacturing of Al alloys and aluminium matrix composites (AMCs). In *Light metal alloys applications*. InTech.

[6] Herzog, D., Seyda, V., Wycisk, E., and Emmelmann, C., 2016. Additive manufacturing of metals. *Acta Materialia*, *117*, pp.371-392.

[7] Cooper, K.P., 2003. *Layered Manufacturing: Challenges and Opportunities*. NAVAL RESEARCH LAB WASHINGTON DC MATERIAL SCIENCE AND TECHNOLOGY DIV.

[8] Monzón, M., Ortega, Z., Hernández, A., Paz, R. and Ortega, F., 2017. Anisotropy of photopolymer parts made by digital light processing. *Materials*, *10*(1), p.64.

[9] Yang, H., Lim, J.C., Liu, Y., Qi, X., Yap, Y.L., Dikshit, V., Yeong, W.Y. and Wei, J., 2017. Performance evaluation of projet multi-material jetting 3D printer. *Virtual and Physical Prototyping*, *12*(1), pp.95-103.

[10] Stucker, B.R.E.N.T., 2012, September. Additive manufacturing technologies: technology introduction and business implications. In *Frontiers of Engineering: Reports on Leading-Edge Engineering From the 2011 Symposium, National Academies Press, Washington, DC, Sept* (pp. 19-21).

[11] http://www.lboro.ac.uk/research/amrg/about/the7categoriesofadditivemanufacturing/materialjetting/

[12] Tay, B.Y. and Edirisinghe, M.J., 2001. Investigation of some phenomena occurring during continuous ink-jet printing of ceramics. *Journal of Materials Research*, *16*(2), pp.373-384.

[13] Wang, T. and Derby, B., 2005. Ink-Jet Printing and Sintering of PZT. *Journal of the American Ceramic Society*, *88*(8), pp.2053-2058.

[14] Yamaguchi, K., Sakai, K., Yamanaka, T. and Hirayama, T., 2000. Generation of three-dimensional micro structure using metal jet. *Precision Engineering*, *24*(1), pp.2-8.

[15] Lewis, J.A., 2006. Direct ink writing of 3D functional materials. *Advanced Functional Materials*, *16*(17), pp.2193-2204.

[16] Xu, X., Meteyer, S., Perry, N. and Zhao, Y.F., 2015. Energy consumption model of Binder-jetting additive manufacturing processes. *International Journal of Production Research*, *53*(23), pp.7005-7015.

[17] Wong, K.V. and Hernandez, A., 2012. A review of additive manufacturing. *ISRN Mechanical Engineering*, *2012*.

[18] Gokuldoss, P.K., Kolla, S. and Eckert, J., 2017. Additive Manufacturing Processes: Selective Laser Melting, Electron Beam Melting and Binder Jetting—Selection Guidelines. *Materials*, *10*(6), p.672.

[19] Gong, H., Rafi, K., Gu, H., Starr, T. and Stucker, B., 2014. Analysis of defect generation in Ti–6Al–4V parts made using powder bed fusion additive manufacturing processes. *Additive Manufacturing*, *1*, pp.87-98.

[20] King, W.E., Anderson, A.T., Ferencz, R.M., Hodge, N.E., Kamath, C., Khairallah, S.A. and Rubenchik, A.M., 2015. Laser powder bed fusion additive manufacturing of metals; physics, computational, and materials challenges. *Applied Physics Reviews*, *2*(4), p.041304.

[21] Merklein, M., Junker, D., Schaub, A. and Neubauer, F., 2016. Hybrid additive manufacturing technologies–an analysis regarding potentials and applications. *Physics Procedia*, *83*, pp.549-559.

[22] Wohlers, T., 2017. Wohlers report. *3D Printing and Additive Manufacturing state of the Industry, Fort Collins, Colorado, USA*. http://lup.lub.lu.se/record/ac880c85-f9ef-477b-b5db-3a7d2d575ea5

[23] Wohlers, T., 2014. Wohlers report. *Wohlers Associates Inc*.

[24] Guo, N. and Leu, M.C., 2013. Additive manufacturing: technology, applications and research needs. *Frontiers of Mechanical Engineering*, *8*(3), pp.215-243.

[25] Paritala, P.K., Manchikatla, S. and Yarlagadda, P.K., 2017. Digital Manufacturing-Applications Past, Current, and Future Trends. *Procedia Engineering*, *174*, pp.982-991.

[26] Townsend, A., Senin, N., Blunt, L., Leach, R.K. and Taylor, J.S., 2016. Surface texture metrology for metal additive manufacturing: a review. *Precision Engineering*, *46*, pp.34-47.

[27] Anitha, R., Arunachalam, S. and Radhakrishnan, P., 2001. Critical parameters influencing the quality of prototypes in fused deposition modelling. *Journal of Materials Processing Technology*, *118*(1), pp.385-388.

[28] Chapiro, M., 2016. Current achievements and future outlook for composites in 3D printing. *Reinforced Plastics*, *60*(6), pp.372-375.

[29] Khairallah, S.A., Anderson, A.T., Rubenchik, A. and King, W.E., 2016. Laser powder-bed fusion additive manufacturing: Physics of complex melt flow and formation mechanisms of pores, spatter, and denudation zones. *Acta Materialia*, *108*, pp.36-45.

[30] Mumtaz, K.A., Vora, P. and Hopkinson, N., 2011. A method to eliminate anchors/supports from directly laser melted metal powder bed processes. In *Proc. Solid Freeform Fabrication Symposium* (pp. 55-64). Sheffield.

[31] Murr, L.E., Gaytan, S.M., Ramirez, D.A., Martinez, E., Hernandez, J., Amato, K.N., Shindo, P.W., Medina, F.R. and Wicker, R.B., 2012. Metal fabrication by additive manufacturing using laser and electron beam melting technologies. *Journal of Materials Science & Technology*, *28*(1), pp.1-14.

[32] Appleyard, D., 2015. Powering up on powder technology. *Metal Powder Report*, *70*(6), pp.285-289.

[33] Górski, F., Wichniarek, R., Kuczko, W., Zawadzki, P. and Buń, P., 2015. Strength of ABS parts produced by Fused Deposition Modelling technology–a critical orientation problem. *Advances in Science and Technology Research Journal*, *9*(26), pp.12-19.

[34] Santoso, S.M., Horne, B.D. and Wicker, S.B., 2013. Destroying by creating: exploring the creative destruction of 3D printing through intellectual property.

[35] Sood, A.K., Ohdar, R.K. and Mahapatra, S.S., 2010. Parametric appraisal of mechanical property of fused deposition modelling processed parts. *Materials & Design*, *31*(1), pp.287-295.

[36] Ning, F., Cong, W., Qiu, J., Wei, J. and Wang, S., 2015. Additive manufacturing of carbon fiber reinforced thermoplastic composites using fused deposition modeling. *Composites Part B: Engineering*, *80*, pp.369-378.

[37] Thrimurthulu, K., Pandey, P.M. and Reddy, N.V., 2004. Optimum part deposition orientation in fused deposition modeling. *International Journal of Machine Tools and Manufacture*, *44*(6), pp.585-594.

[38] Levy, G.N., Schindel, R. and Kruth, J.P., 2003. Rapid manufacturing and rapid tooling with layer manufacturing (LM) technologies, state of the art and future perspectives. *CIRP Annals-Manufacturing Technology*, *52*(2), pp.589-609.

[39] Kimura, T., Nakamoto, T., Mizuno, M. and Araki, H., 2017. Effect of silicon content on densification, mechanical and thermal properties of Al-xSi binary alloys fabricated using selective laser melting. *Materials Science and Engineering: A*, *682*, pp.593-602.

[40] Yadroitsev, I., Bertrand, P., Antonenkova, G., Grigoriev, S. and Smurov, I., 2013. Use of track/layer morphology to develop functional parts by selective laser melting. *Journal of Laser Applications*, *25*(5), p.052003.

[41] Thijs, L., Verhaeghe, F., Craeghs, T., Van Humbeeck, J. and Kruth, J.P., 2010. A study of the microstructural evolution during selective laser melting of Ti–6Al–4V. *Acta Materialia*, *58*(9), pp.3303-3312.

[42] Zhu, Y., Zou, J., Chen, X. and Yang, H., 2016. Tribology of selective laser melting processed parts: stainless steel 316L under lubricated conditions. *Wear*, *350*, pp.46-55.

[43] Lu, Y., Wu, S., Gan, Y., Huang, T., Yang, C., Junjie, L. and Lin, J., 2015. Study on the microstructure, mechanical property and residual stress of SLM Inconel-718 alloy manufactured by differing island scanning strategy. *Optics & Laser Technology*, *75*, pp.197-206.

[44] Pauly, S., Löber, L., Petters, R., Stoica, M., Scudino, S., Kühn, U. and Eckert, J., 2013. Processing metallic glasses by selective laser melting. *Materials Today*, *16*(1), pp.37-41.

[45] Jung, H.Y., Choi, S.J., Prashanth, K.G., Stoica, M., Scudino, S., Yi, S., Kühn, U., Kim, D.H., Kim, K.B. and Eckert, J., 2015. Fabrication of Fe-based bulk metallic glass by selective laser melting: a parameter study. *Materials & Design*, *86*, pp.703-708.

[46] Laakso, P., Riipinen, T., Laukkanen, A., Andersson, T., Jokinen, A., Revuelta, A. and Ruusuvuori, K., 2016. Optimization and simulation of SLM process for high density H13 tool steel parts. *Physics Procedia*, *83*, pp.26-35.

[47] Yadroitsev, I., Gusarov, A., Yadroitsava, I. and Smurov, I., 2010. Single track formation in selective laser melting of metal powders. *Journal of Materials Processing Technology*, *210*(12), pp.1624-1631.

[48] Sander, J., Hufenbach, J., Giebeler, L., Wendrock, H., Kühn, U. and Eckert, J., 2016. Microstructure and properties of FeCrMoVC tool steel produced by selective laser melting. *Materials & Design*, *89*, pp.335-341.

[49] Averyanova, M., Cicala, E., Bertrand, P. and Grevey, D., 2011, September. Optimization of selective laser melting technology using design of experiments method. In *Innovative Developments in Virtual and Physical Prototyping: Proceedings of the 5th International Conference on Advanced Research in Virtual and Rapid Prototyping, Leiria, Portugal, 28 September-1 October, 2011* (p. 459). CRC Press.

[50] Denlinger, E.R., Irwin, J. and Michaleris, P., 2014. Thermo-mechanical modeling of additive manufacturing large parts. *Journal of Manufacturing Science and Engineering*, *136*(6), p.061007.

[51] Ning, F., Cong, W., Hu, Y. and Wang, H., 2017. Additive manufacturing of carbon fiber-reinforced plastic composites using fused deposition modeling: Effects of process parameters on tensile properties. *Journal of Composite Materials*, *51*(4), pp.451-462.

[52] Lindbäck, J.E., Björnsson, A. and Johansen, K., 2012. New Automated Composite Manufacturing Process: Is it possible to find a cost effective manufacturing method with

the use of robotic equipment? In *The 5th International Swedish Production Symposium 6th-8th of November 2012 Linköping, Sweden* (pp. 523-531).

[53] Quader, M.A., Ahmed, S., Ghazilla, R.A.R., Ahmed, S. and Dahari, M., 2015. A comprehensive review on energy efficient CO 2 breakthrough technologies for sustainable green iron and steel manufacturing. *Renewable and Sustainable Energy Reviews*, *50*, pp.594-614.

[54] Pellegrino, J. and Jamison, K., 2015. *US DOE Roundtable and Workshop on Advanced Steel Technologies: Emerging Global Technologies and R&D Opportunities* (No. ORNL/TM--2015/742). Oak Ridge National Laboratory (ORNL), Oak Ridge, TN (United States).

[55] Gao, G. and Cui, X., 2016. Three-dimensional bio-printing in tissue engineering and regenerative medicine. *Biotechnology letters*, *38*(2), pp.203-211.

[56] Abd-Elghany, K. and Bourell, D.L., 2012. Property evaluation of 304L stainless steel fabricated by selective laser melting. *Rapid Prototyping Journal*, *18*(5), pp.420-428.

[57] Badrossamay, M. and Childs, T.H.C., 2007. Further studies in selective laser melting of stainless and tool steel powders. *International Journal of Machine Tools and Manufacture*, *47*(5), pp.779-784.

[58] Kempen, K., Thijs, L., Van Humbeeck, J. and Kruth, J.P., 2012. Mechanical properties of AlSi10Mg produced by selective laser melting. *Physics Procedia*, *39*, pp.439-446.

[59] Maskery, I., Aboulkhair, N.T., Corfield, M.R., Tuck, C., Clare, A.T., Leach, R.K., Wildman, R.D., Ashcroft, I.A. and Hague, R.J., 2016. Quantification and characterisation of porosity in selectively laser melted Al–Si10–Mg using X-ray computed tomography. *Materials Characterization*, *111*, pp.193-204.

[60] Liu, Q., Leu, M.C. and Schmitt, S.M., 2006. Rapid prototyping in dentistry: technology and application. *The international journal of advanced manufacturing technology*, *29*(3-4), pp.317-335.

[61] Onuh, S.O. and Yusuf, Y.Y., 1999. Rapid prototyping technology: applications and benefits for rapid product development. *Journal of intelligent manufacturing*, *10*(3), pp.301-311.

[62] Thompson, M.K., Moroni, G., Vaneker, T., Fadel, G., Campbell, R.I., Gibson, I., Bernard, A., Schulz, J., Graf, P., Ahuja, B. and Martina, F., 2016. Design for Additive Manufacturing: Trends, opportunities, considerations, and constraints. *CIRP Annals-Manufacturing Technology*, *65*(2), pp.737-760.

[63] Caitlin, O., 2017. Designing for Additive Manufacturing, Part II: Consideration for Manufacturability. *Precision Metal Forming Association, 3D Metal Printing Magazine,* winter 2017 *2(1),* pp. 26-28.

[64] Bourell, D.L., Beaman, J.J., Leu, M.C. and Rosen, D.W., 2009. A brief history of additive manufacturing and the 2009 roadmap for additive manufacturing: looking back and looking ahead. *Proceedings of RapidTech*, pp.24-25.

Chapter 2 Microstructure and Mechanical Properties of 3D Printed Carbon Fiber Reinforced Plastic Composites

2.1 Introduction

3D printing is a fused deposition modelling (FDM) additive manufacturing (AM) technology that is used to generate unique products from technically developed CAD models. Special design softwares are used to design and transfer point cloud data to a 3D printer. The process entails a collection of settings including speed, size, support, material, and quality control which must be set to ensure desired output is realized. Based on the process parameters selected, the digital model is translated into line-by-line printer instructions often termed as the G-code. The electronic data (G-code) control the toolpath, position, and speed thereby ensuring the execution of predetermined motions. The material usually in filament form is conveyed from a reel to the preheated nozzle by motorized gears. It is then heated to some temperatures slightly above the melting point and immediately deposited onto the build platform. Once a layer is completed, the build platform is moved a unit layer distance downwards and a subsequent layer laid. This process is repeated layer after layer until the entire product is completed. Since the material undergoes repeated heating and cooling, it is important to select a material that is capable of withstanding this complicated thermal variations. 3D printing can produce prototypes and end-use parts with intricate geometries that are difficult or impossible to manufacture by conventional methods at reduced cycle time, inventory, and cost [1].

A limited scope of material (including polymers, metals, ceramics, and composites) is available for the additive manufacturing of functional parts. Among them, composites are often paraded as the materials of the future. Their high strength and stiffness properties combined with low weight results in strength-to-weight and stiffness-to-weight ratios several

times greater than those of steel or aluminum. Therefore, offering an incredible advantage over most structural and sub-structural materials. Some leading composites include polymer matrix, metal matrix, ceramic matrix, fiber and particulate reinforced composites. Fiber reinforced composites are used for many applications in the aerospace and automotive industry due to their high specific strength. Indeed, with the Boeing 787, carbon fiber reinforced composites constitute about 50% of the material requirement during their construction [2]. In addition, the material is taking a mainstream stronghold in the manufacture of Airbus A320 aircrafts and BMW i-series among others [3]. Traditional manufacturing methods for composites (for example injection molding, pultrusion processes, and machining) are time consuming and labor intensive, which leads to high costs. To remedy this, manufacturers have emphasized on paradigm shift to automated composite manufacturing i.e., automated tape layup (ATL), automated fiber placement (AFP), filament winding (FW), and additive manufacturing technology in order to improve process and cost efficiency [4]. The adoption of additive manufacturing is anchored on its ability to produce CFR-ABS products with complex geometries that are difficult or impossible to manufacture by conventional methods at reduced cycle time and costs. In addition, design visualization as a proof of concept and modification prior to actual fabrication is possible [1].

Over the last three decades, AM technology has progressed from simple 3D printers used for rapid prototyping in non-structural resins to refined rapid manufacturing systems that can be used to create fully functional parts in different engineering materials directly without the use of additional tooling [5]. Most work to date has been conducted using polymer materials, but the development of AM processes such as selective laser melting (SLM), electron beam melting (EBM), and laser engineered net shaping (LENS) have enabled fabrication of 3D parts from metals, ceramics, and metal-matrix composites [6].

Unlike in the conventional manufacturing processes where the properties of the finished parts are predictable, 3D-printed parts have dynamic and unpredictable properties which depend more on the manufacturing process than the material [7]. Many researchers have investigated the influences of process parameters on mechanical properties of 3D printed products. The effects of parameters such as build orientation, layer thickness, air gap (overlap), and build platform/nozzle temperature on surface quality have been investigated [8-12]. The authors reported that layer thickness and build orientation were the significant factors in determining the surface quality of built parts. They concluded that small layer thickness results in higher surface quality at increased building time. Moreover, the part surface which is perpendicular to the building direction has smoother structure as compared to the other (parallel to building direction) surfaces [13].

Onwubolu *et al.* [14] used the group method for data modelling to predict the anisotropic characteristics of FDM parts. In their study, the authors found that tensile strength was greatest for parts with fibers aligned along the axis of the tension force. They concluded that, minimum layer thickness, negative air gap, and 0° part orientation (with the part orientation parallel to the direction of lading) result in maximum tensile properties. The complexity and challenges associated with FDM limit experimental process parameter-anisotropic property optimization.

The main objective of this research was to investigate the influence of process parameters on the microstructure and mechanical properties of 3D printed CFR-ABS material. In this study, an experimental approach (design of experiment) was adopted in order to optimize layer thickness, printing speed, and raster direction. ABS material reinforced with 15 wt% carbon fibers (CFR-ABS) in a nano-scale was printed, iterative adjustments on these parameters were done, and the changes in their intrinsic properties with respect to the process parameters were investigated. In addition, ABS samples were printed for comparison

purposes. Microstructure evaluation and mechanical tests were carried out on the 3D printed CFR-ABS samples with a view to optimize and enhance final product performance.

2.2 Experimental procedure

2.2.1 Sample preparation

ABS and CFR-ABS filament materials (3DXTECH, MI, USA) with a diameter of 1.75 mm were used in preparing the test samples. Bellolu-200 series 3D printer was used to print standard tensile test samples with a gauge section of 34 mm in length, 6 mm in width, and 3 mm in thickness as per the D638-2a ASTM standards [15]. The samples were designed using Solidworks design software and the CAD data transferred into the 3D printer. The nozzle was first preheated and the filament fitted. Kaptone tape was stuck on the build platform and ABS slurry smeared to ensure the sample adhered properly during the entire printing process. As shown in Fig. 2.1, the filament is fed into the preheating nozzle with the help of driver gears and grooved bearing which provide sufficient feeding and extrusion pressure once the material is melted. 3D parts are build layer after layer with the filament material heated to glass transition state and extruded through the nozzle at a constant temperature [6]. The nozzle moves on the X-Y plane as the tool path dictated by the 3D CAD data depositing a pre-determined layer onto the build platform. When the layer is completed, the build platform moves down (a specified z) for one layer height to allow for the successive layer deposition. This process is repeated until the final 3D part is completed.

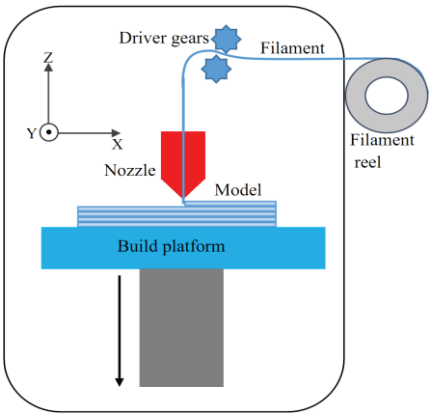

Fig. 2.1. Schematic illustration of FDM 3D-printing process.

The effect of process parameters, including nozzle and bed temperatures, layer thickness, printing speed, and raster direction (see Table 2.1), on surface morphology, geometrical shape, and mechanical properties of printed samples were investigated and the optimum printing conditions were determined.

Table 2.1 Materials and process parameters used in the experiments.

Materials	ABS, CFR-ABS (Carbon X ™)
Bed temperature (°C)	90 - 110
Nozzle temperature (°C)	235, 243
Printing speed (mm/min)	2000, 3200, 4000
Layer thickness (mm)	0.1, 0.2, 0.3
Raster direction (degrees)	0°, 45°, 90°

For each set of process parameters (layer thickness and printing speed), three samples were printed in three different raster directions (Fig. 2.2). No post processing was performed for printed test samples.

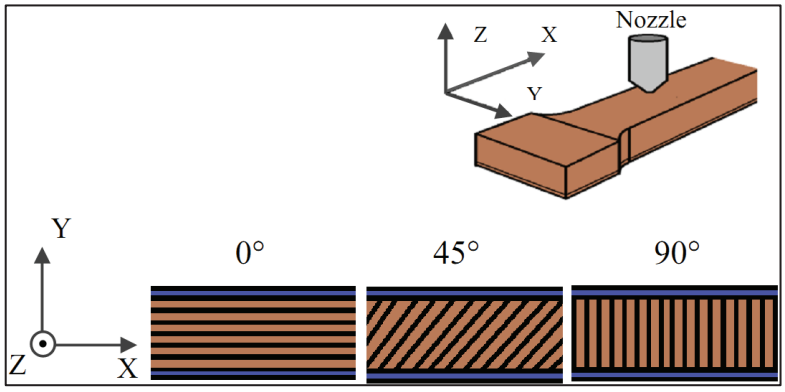

Fig. 2.2 Raster directions.

2.2.2 Characterization

The microstructure was observed using optical microscopy (OM) and scanning electron microscopy (SEM). A non-contact laser reflectance VHX-5000 digital microscope (Keyence, Japan) was used to evaluate the surface roughness (Ra) of the samples. An average of three Ra measurements was taken at each processing condition. The tensile tests were performed at room temperature with a crosshead speed of 1 mm/min (corresponding to an initial strain rate of $4.9 \times 10^{-4} s^{-1}$) using a 50 kN Shimadzu universal testing machine. The strain was determined by measuring machine crosshead displacement during the tensile tests, and at least three samples for each condition were tested. In addition, fractographic examinations on the tensile tested samples were done to evaluate the failure behavior.

2.3 Results and discussion

2.3.1 Effects of process parameters on surface morphology and geometrical shape

The surface quality and sample geometry are primarily influenced by layer thickness, printing speed, and raster direction or building orientation. As the layer thickness increased, the accuracy of the overall finished sample geometry decreased and the outline more readily displayed the ‘staircase’ phenomenon (coarse and wavy surface/edge). As shown in Fig. 2.3

(a)-(c), the surface roughness was relatively low at the smallest layer thickness of 0.1 mm, and increased with the increase in layer thickness irrespective of the raster direction used. Furthermore, it is evident that 3D printed CFR-ABS samples had relatively higher values of surface roughness compared to ABS samples. Processing the samples at low printing speed (2000 mm/min) and high printing speed (4000 mm/min) resulted in poor surface quality. Therefore, an intermediate printing speed seems to be beneficial to the surface quality of the printed samples. In this study, the best surface quality with a roughness value of 14.32 µm was achieved at a printing speed of 3200 mm/min and small layer thickness of 0.1 mm (Fig. 2.3 (a)). Indeed, increasing the layer thickness from 0.1 to 0.3 mm, the surface apparently transformed into a rough surface characterized by clearly visible threads of deposed material as shown in Fig. 2.4.

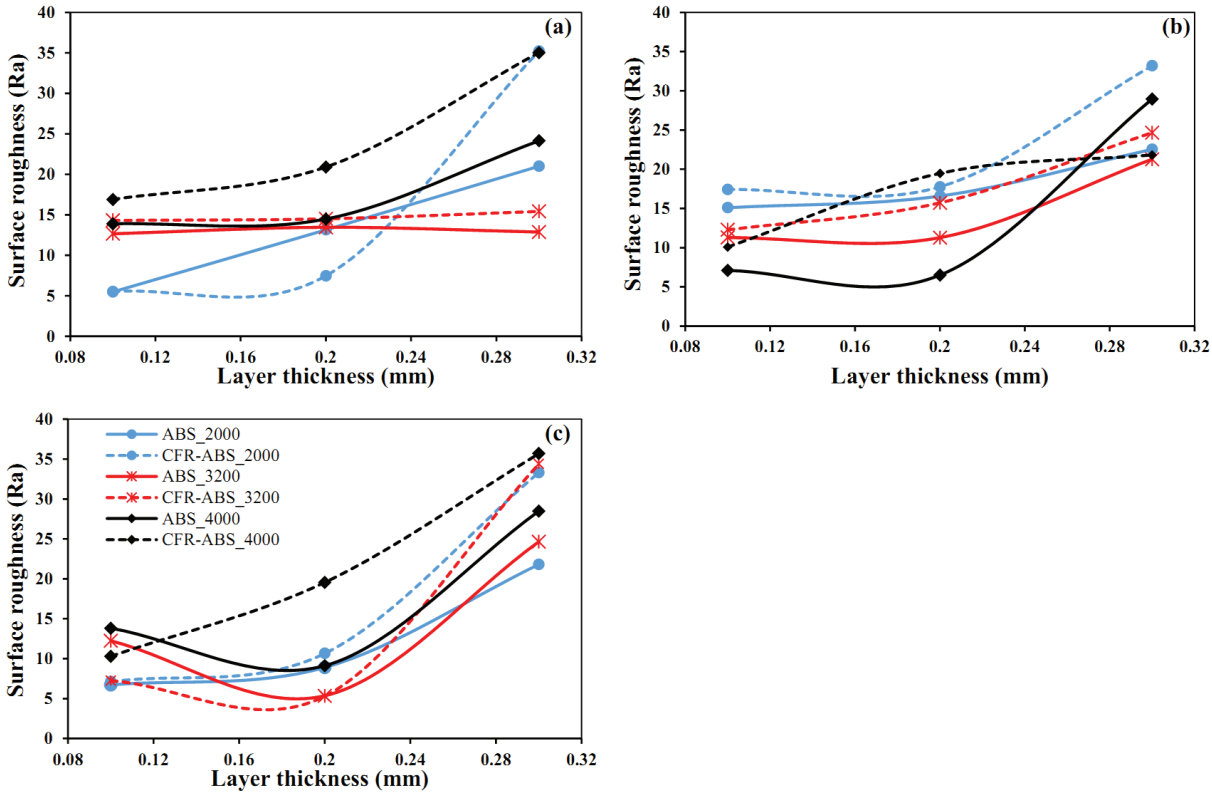

Fig. 2.3 Surface roughness of 3D printed ABS and CFR-ABS samples at raster angles of (a) 0°, (b) 45°, and (c) 90° under different layer thicknesses and printing speeds.

As shown in Fig. 2.3, the raster direction significantly affected the surface accuracy. Good surface quality was obtained on samples processed at raster directions of 0° and 90°. At a raster angle of 45° (Fig. 3 (b)), relatively poor surface ($21.81 \leq Ra \leq 33.2$) was obtained for CFR-ABS samples processed at a layer thickness of 0.3 mm due to heightened 'staircase phenomenon' (high degree of surface waviness). Similar phenomena have been reported by numerous researchers [16-20], they deduced that surface accuracy was maximized by minimizing average weighted layer thickness, maximizing the area of non-stepped surfaces, and orienting the surface either horizontally (0° raster direction) or vertically (90° raster direction). However, in complex surfaces, this is not always achievable, so it is then preferable to orient it as near vertical as possible.

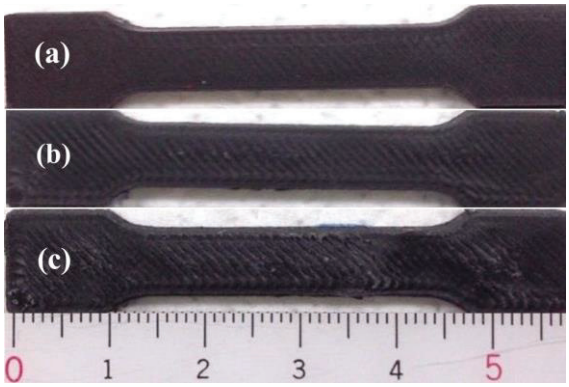

Fig. 2.4. Tensile test samples showing the variations in the surface quality with different layer thicknesses of (a) 0.1mm, (b) 0.2 mm, and (c) 0.3 mm. All the samples were printed at printing speed of 3200 mm/min.

2.3.2 Microstructure characterization

Figs 2.5 and 2 6 respectively show the OM and SEM images on the vertical cross sections (parallel to the building direction) revealing the integrity of bonding as well as distributions of pores and carbon fibers under different conditions of layer thickness and printing speed. Clearly, continuous body of deposited material without visible layers (Sample 4 in Fig.2.5) and uniformly distributed carbon fibers (Fig. 2.6 (a)) were observed in the

sample printed at a small layer thickness of 0.l mm and intermediate printing speed of 3200 mm/min. This demonstrates that high-quality bonding occurred during printing. However, microscopic gaps, randomly distributed carbon fibers (Fig. 2.6(b)), and layer/layer intersection lines were found in the samples processed at high (4000 mm/min) and low (2000 mm/min) printing speeds (Samples 1 and 7 in Fig. 5). When the layer thickness was increased to 0.2 and 0.3 mm, a lot of gaps remained as seen in Fig. 2.5 (Samples 2, 3, 5, 6, 8, and 9). It seems that the size and number of these irregularly shaped gaps increase with increase in layer thickness and printing speed. In addition, discrete layers are visible with most carbon fibers discharged randomly (Fig. 2.6(c)) in the ABS matrix.

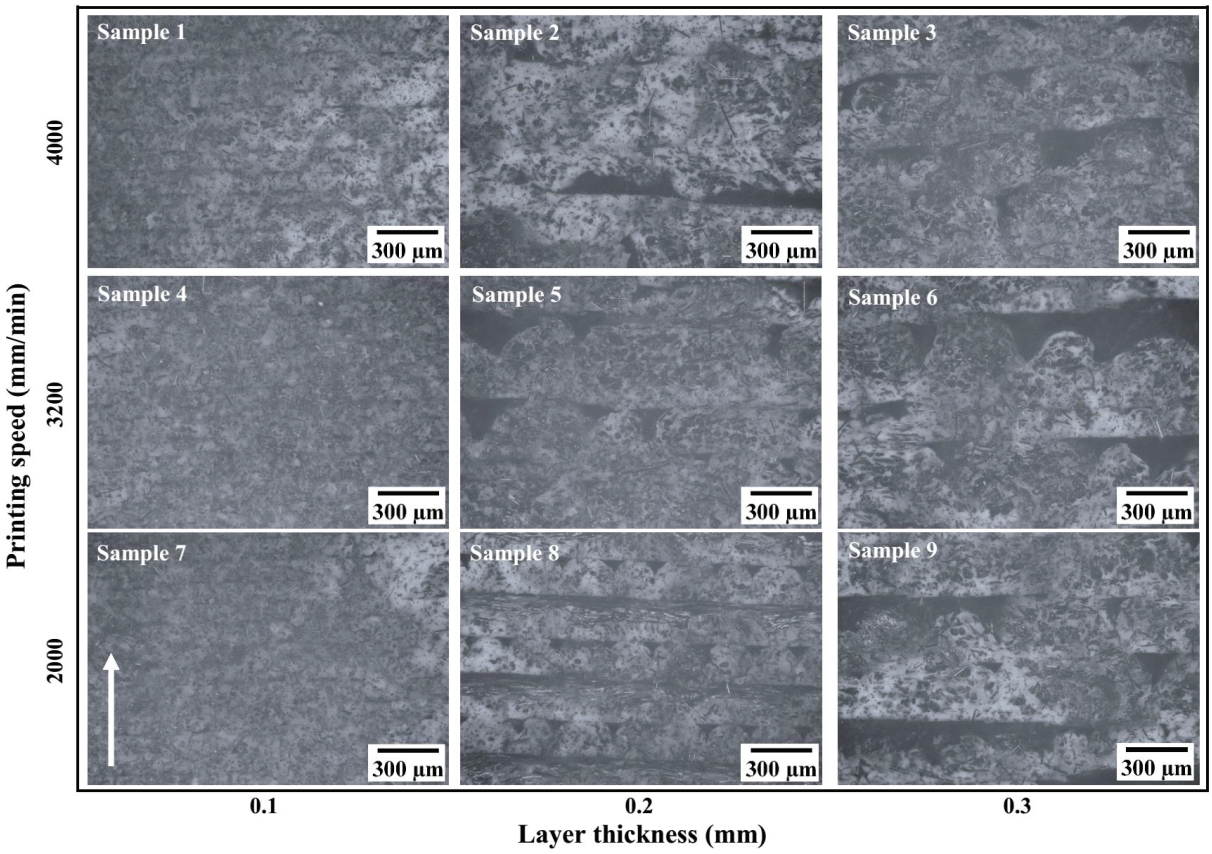

Fig. 2.5 Optical microscopy images on the vertical cross sections parallel to the building direction of 3D printed sample showing the effects of layer thickness and printing speed on inter-layer bonding and pore distributions. The arrow indicates the building direction.

Indeed, large layer thickness results in poor inter-layer bonding regardless of the printing speed. This is because large layer thickness (large nozzle diameter) provides a larger surface area exposing the extrudate to the atmosphere. This makes the semi-melted material to experience slight cooling before the start of the fusion process due to the high thermal gradient between the already solidified layers and the cooling extrudate. Reduced fluidity of the extrudate causes insufficient filling resulting in gaps and poor inter-layer bonding. Further SEM observations shown in Fig. 2.7 revealed the inclinations of reinforcing fibers, pore shape and distribution with respect to the raster direction. The short carbon fibers, displayed in grayish dots in the ABS matrix, appeared out of /into the plane for samples processed at a raster direction of 0° (Fig. 2.7(a) and (b)).

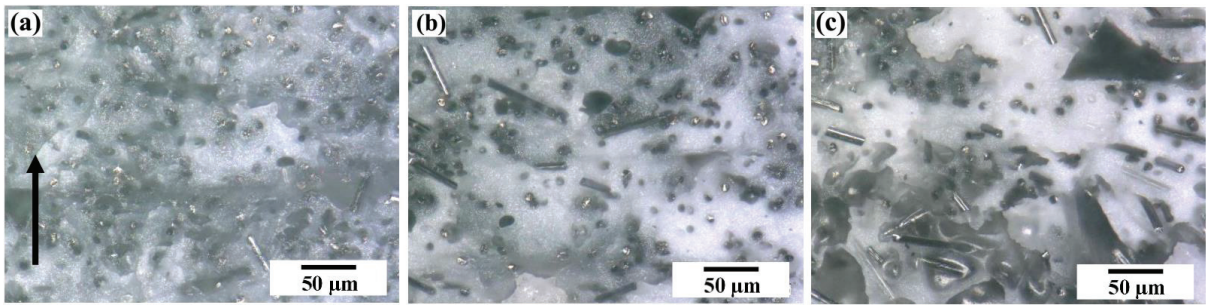

Fig. 2.6. SEM images on the vertical cross sections parallel to the building direction of 3D printed sample at layer thickness and printing speed of (a) 0.1 mm and 3200 mm/min (b) 0.1 mm and 2000 mm/min, and (c) 0.3 mm and 4000 mm/min, respectively. The arrow indicates the building direction.

Some voids (dark dots) are believed to be attributed to pull-out of fibers during failure of the samples in the tensile test. Moreover, other triangular shaped pores which are not due to fiber pull-out are also noticeable. The appearance of such pores may result from gas escaping during printing. For samples processed at a raster direction of 45° shown in Fig. 2.7(b), the reinforcing carbon fibers were seen in the crossed deposition directions and the pores left by fiber pull-out and other pores were also observed. The lateral deposition lines, carbon fibers, and pores resembling cylinders are observed in sample (Fig. 2.7(c)) fabricated at a raster

direction of 90°. The latter are as a result of the fiber pull-out during failure of the samples, while tested by a tensile load applied perpendicularly to the material deposition direction. Other pores, which are not due to fiber pull-out, are also noticed in other SEM images in Fig 2.7. It is clear that, the short carbon fibers dispersed in the ABS matrix was highly oriented to the printing directions. This is because the extrusion nozzle melts the ABS and the fibers inside the deposited material have a tendency to become aligned to the extrusion direction of the molten thermoplastic during 3D printing. Moreover, the quantity of the pull-out fibers in the fracture surface is determined by the adhesion at the interface of the carbon fiber and ABS matrix. Poor adhesive bond results in many pull-out fibers. Otherwise, few or no pull-out is exhibited. In this study, samples processed at a printing speed of 3200 mm/min, layer thickness of 0.1 mm, and at a raster direction of 0° had fewer pull-out fibers and hardly any pores.

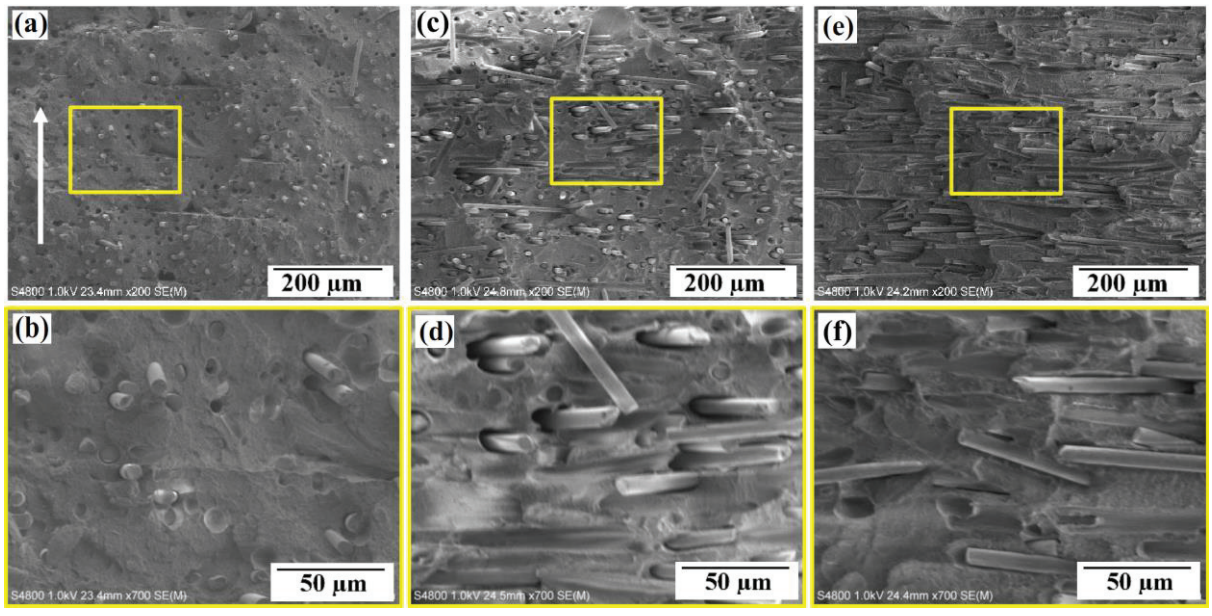

Fig. 2.7 Fracture surfaces of CFR-ABS samples printed at raster angles of (a) and (b) 0°, (c) and (d) 45°, and (e) and (f) 90° under the conditions of printing speed of 3200 mm/min and layer thickness of 0.1 mm. The arrow indicates the building direction.

2.3.3 Effect of process parameters on mechanical properties of CFR-ABS composites

The tensile test results shown in Fig. 2.8 clearly reveal that, 3D printed CFR-ABS composites have lower tensile strength and smaller amount of ductility compared to ABS samples. In addition, samples printed at small layer thickness possess higher tensile strength compared to those produced at large layer thickness. One of the probable reasons for this variations in tensile strength with layer thickness is that, small layer thickness may allow sufficient residual heat energy to activate the surfaces of the adjacent regions causing good inter-layer bonding. In this way, properly bonded layers offer high resistance to deformation, giving rise to high tensile strength at small layer thickness. Conversely, insufficient preheating may occur when printing at large layer thickness thereby reducing the degree of inter-layer bonding. The distinct boundaries between new and previously deposited material are possible fracture origins where the layers can be easily separated, hence reducing yield and tensile strength.

The rate of material solidification after deposition is critical in determining the resultant properties. Epitaxial solidification is necessary to ensure material bond instantaneously upon deposition. Due to solidification inefficiencies, the 3D printed ABS and CFR-ABS samples are subject to flaws consisting of both extensive pores (volume error), weak inter-layer bonding (see Fig. 2.5), and insufficient bonding between the carbon fibers and the matrix. These defects make the effective area (supporting the load) smaller than in case of the injection molded parts, which increases the overall stress and decreases strength thereby limiting the tensile strength of the printed samples.

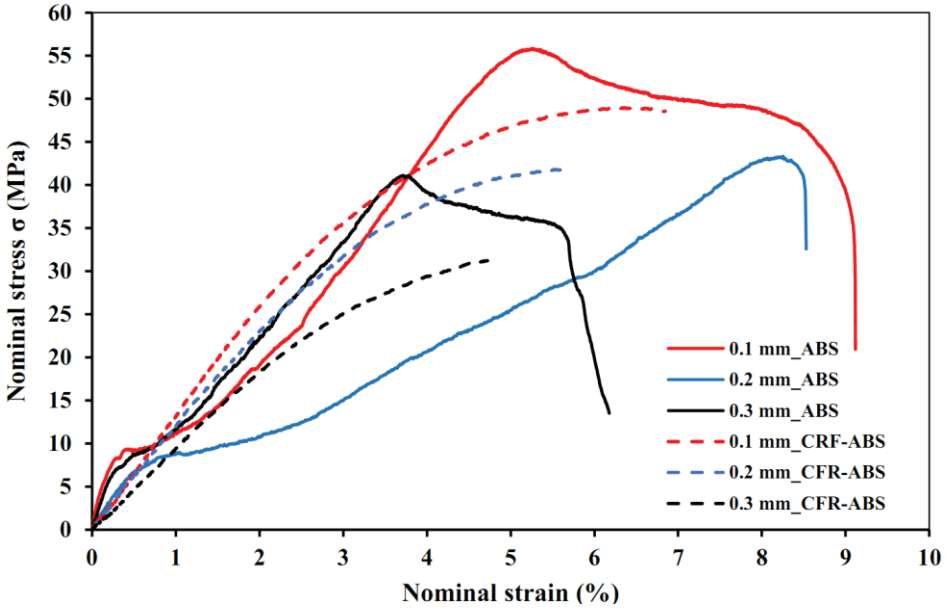

Fig. 2.8 Nominal stress-strain curves of ABS and CFR-ABS composites printed at 3200 mm/min and layer thickness ranging from 0.1 to 0.3 mm.

As shown in Table 2.2, samples printed from 15 wt% CFR-ABS material had reduced tensile strength compared to their ABS counterparts. This reduction in tensile strength may be associated with the presence of weak bonding at the interface between the carbon fiber and the ABS matrix. According to Fig. 2.9(a) and (b), considerable gaps are visible between the ABS matrix and carbon fibers indicating the poor interfacial adhesion between the matrix and carbon fibers. When such weakly bonded CFR-ABS samples are subjected to tensile loads, the carbon fibers do not rupture with the fracture of matrix due to disrupted transfer of shear from the matrix to the carbon fibers limiting the strength of the material. Excess shear between the matrix and carbon boundary causes failure of the samples with fracture surfaces having pull-out fibers and pull-out complementary holes, respectively as indicated by the complete and dotted arrows in Fig. 2.9. Clearly, maximum tensile strength of 49.03 MPa was obtained in the CFR-ABS sample printed at a medium speed of 3200 mm/min. On the other hand, samples printed from ABS material at this speed displayed the highest tensile strength (55.86 MPa). Decreasing or increasing the printing speed led to reduction in tensile strength

of the 3D printed ABS and CFR-ABS samples. It can be deduced that, this intermediate printing speed provided better bonding conditions, minimal formation of microscopic gaps, and enhanced mechanical properties of both ABS and CFR-ABS composites.

Raster direction is the angle at which the layers are deposited with respect to the x-axis of the build table. The typical raster directions are 0°/90°, 30°/60°, and 45°/45° [21]. It can also be regarded as the angle between the loading force and the layer slicing plane [22]. From the tensile test results, it is clear that samples printed at orientations other than zero degree (0°) exhibited reduced tensile strength. Indeed, the higher the raster direction angle, the lower the tensile strength, see Table 2.2. If this angle is higher than zero, the applied force is carried not only by the material threads but also a certain portion of the load is applied to layer bonds, which are very weak due to lack of material fusion between adjacent layers[13]. As shown in Table 2.2, CFR-ABS samples printed at 0° had higher tensile strength while those printed at raster direction perpendicular to the loading direction (90°) had lower tensile strength. Beyond the critical raster direction angle range (5-30°) [13], the layer bond maximal strength is reached faster than strength of the material itself causing disjoint of the layers.

Table 2.2. Tensile test results of ABS and CFR-ABS composites printed at different conditions.

Raster direction (degree)	Layer thickness (mm)	Low speed (2000 mm/min)		Medium speed (3200 mm/min)		High speed (4000 mm/min)	
		Tensile strength (MPa)					
		ABS	CFR-ABS	ABS	CFR-ABS	ABS	CFR-ABS
0	0.1	44.18	47.80	55.86	49.03	53.58	44.95
	0.2	40.72	32.18	42.77	41.85	37.06	40.62
	0.3	41.25	31.56	41.12	31.24	37.33	33.13
45	0.1	43.08	43.33	48.15	36.76	45.34	34.35
	0.2	42.11	40.66	47.28	26.85	41.65	31.75
	0.3	43.59	34.35	43.43	22.88	38.27	29.81
90	0.1	41.63	39.10	48.11	30.40	40.60	37.09
	0.2	40.80	35.02	45.56	28.24	41.89	34.08
	0.3	35.97	31.07	36.36	27.60	35.52	32.47
		Young's Modulus (GPa)					
0	0.1	1.55	4.79	1.65	1.99	1.72	2.22
	0.2	1.46	4.34	1.62	2.41	1.58	2.33
	0.3	1.66	4.01	1.67	1.92	1.51	1.84
45	0.1	1.72	4.67	1.71	1.40	1.75	1.58
	0.2	1.68	3.93	1.82	1.18	1.84	1.39
	0.3	1.85	4.36	1.75	1.56	1.65	1.40
90	0.1	1.88	3.71	1.96	1.35	1.60	1.61
	0.2	1.91	3.61	1.86	1.87	1.67	1.28
	0.3	1.65	3.35	1.78	1.24	1.68	1.62

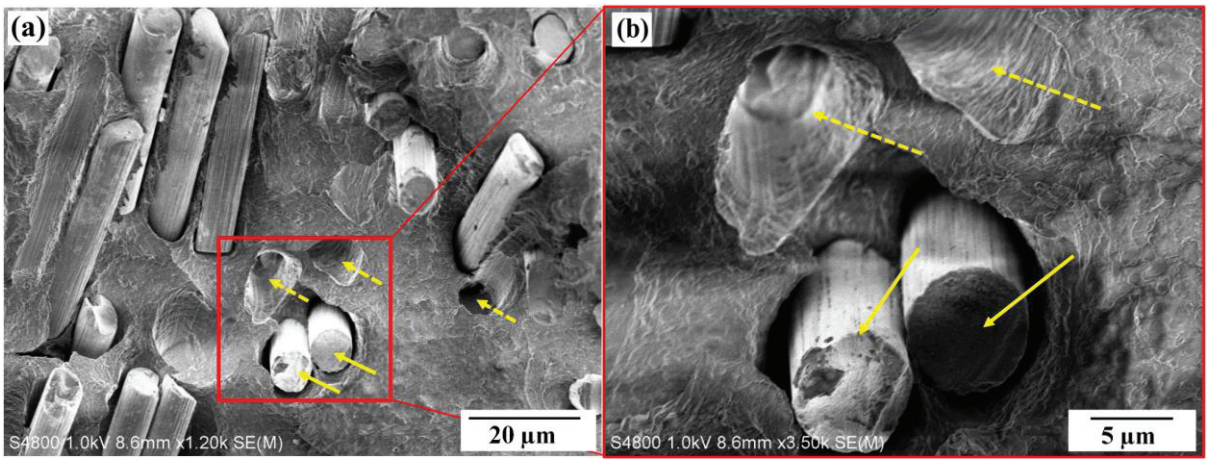

Fig. 2.9 FESEM images of fracture surfaces of CFR-ABS composite printed at 3200 mm/min, 0^0, and layer thickness of 0.1 mm showing "pullout" phenomenon and weak adhesive bonding between carbon fibers and ABS matrix. The complete arrows indicate "pullout" fibers, while dotted arrows indicate "pullout" complementary holes.

As shown in Fig. 2.10, samples loaded in the direction perpendicular to the 90° raster direction had lower tensile ductility than those loaded parallel to 0° raster direction. This is because, in the latter failure occurred due to layer shearing at significantly high elongation offering more load bearing capabilities unlike in the former, where failure was due to layer separation at minimal elongation. The results show that, CRF-ABS samples printed at 3200 mm/min and a raster direction of 45° exhibited tremendous ductility. Moreover, small layer thickness and higher printing speed on 3D printed ABS samples resulted in enhanced ductility. Samples printed with CFR-ABS material had high values of Young's modulus, this value decreased with increase in layer thickness and printing speed. The raster direction which determines the carbon fiber deposition direction adversely affected the stiffness of the samples. As shown in Table 2.2, the value of Young's modulus was high for CFR-ABS composites processed at raster direction of 0° and low printing speed. This value decreased with increase in layer thickness and printing speed. It can be concluded that the 3D printed CFR-ABS composite has a stiffness behavior similar to unidirectional fiber reinforced composites, as indeed a composite reinforced with short fibers ends up highly oriented along

the 3D printing direction. The higher values of Young's modulus of the carbon fiber material accounts for the increased stiffness in CFR-ABS samples.

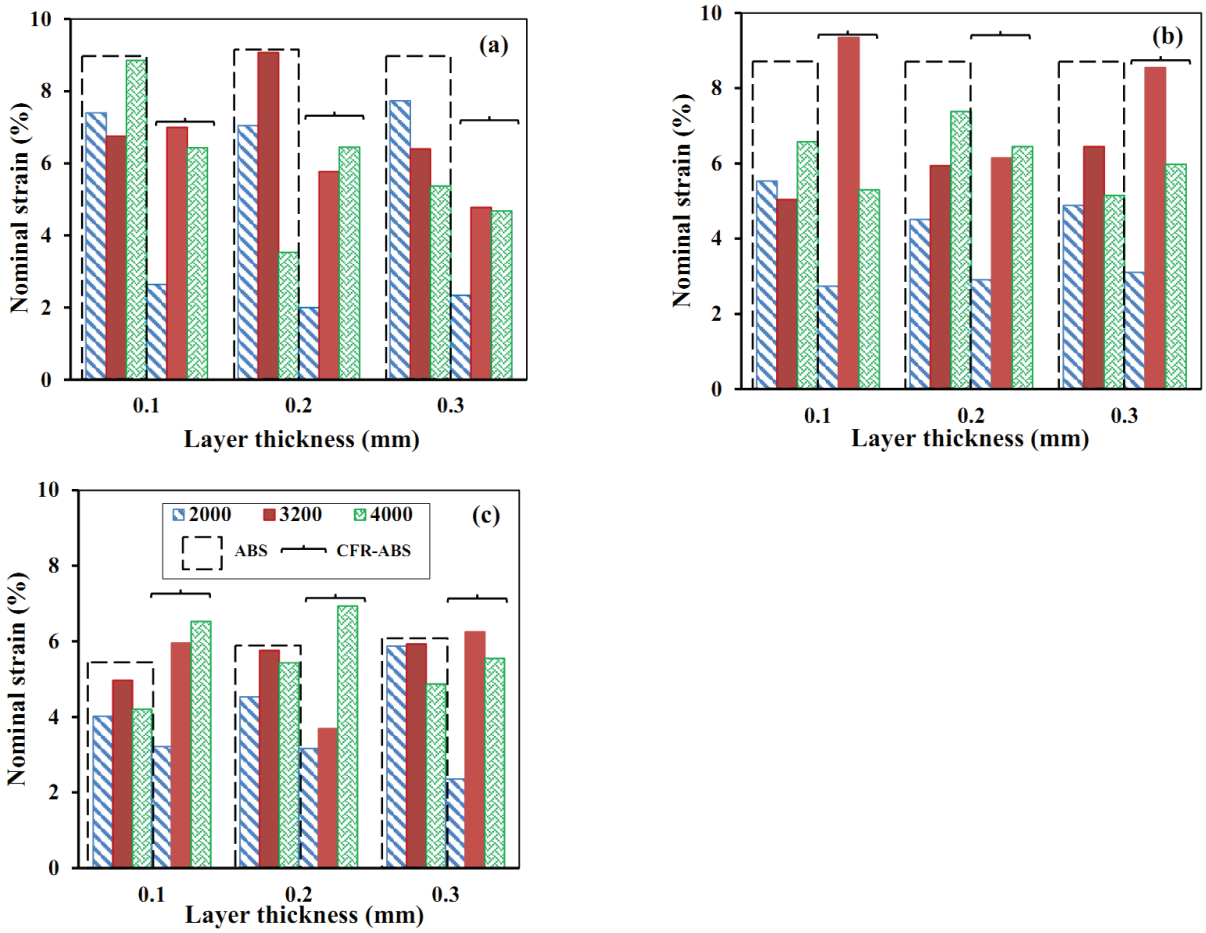

Fig. 2.10 Effects of raster direction (a) 0° (b) 45° (c) 90°, layer thickness and printing speed (2000, 3200, 4000 mm/min) on percentage elongation of 3D printed ABS/CFR-ABS samples.

The fracture of 3D-printed CFR-ABS composites occurs mainly via damage to the raster with the staircase effect immensely contributing to the failure. As the tensile load increases, the failure begins at the weakest raster specifically at the cusp point (Fig. 2.11) and next weakest raster will break, in sequence, this fissure propagates through weak inter-layer bond (as shown in Fig. 2.12) until total failure of the sample occurs. Fractographic observations on the tensile test fracture surfaces (of 3D printed ABS samples) as shown in Fig. 2.13 revealed that samples printed at a raster direction of 0° exhibited ductile rupture dominated by dimples

while those printed at raster directions of 45° and 90° had brittle rupture characterized by quasi-cleavages and cleavage facets respectively. This observation is in agreement with the percentage elongation findings shown in Fig. 2.10. Entirely brittle fracture is observed for all the samples printed with CFR-ABS composite. Carbon fiber threads are seen to break without any considerable elongation. Quasi-cleavages are seen on the fracture surfaces (Fig. 2.7(b), (d), and (f)) depicting a brittle rupture mode.

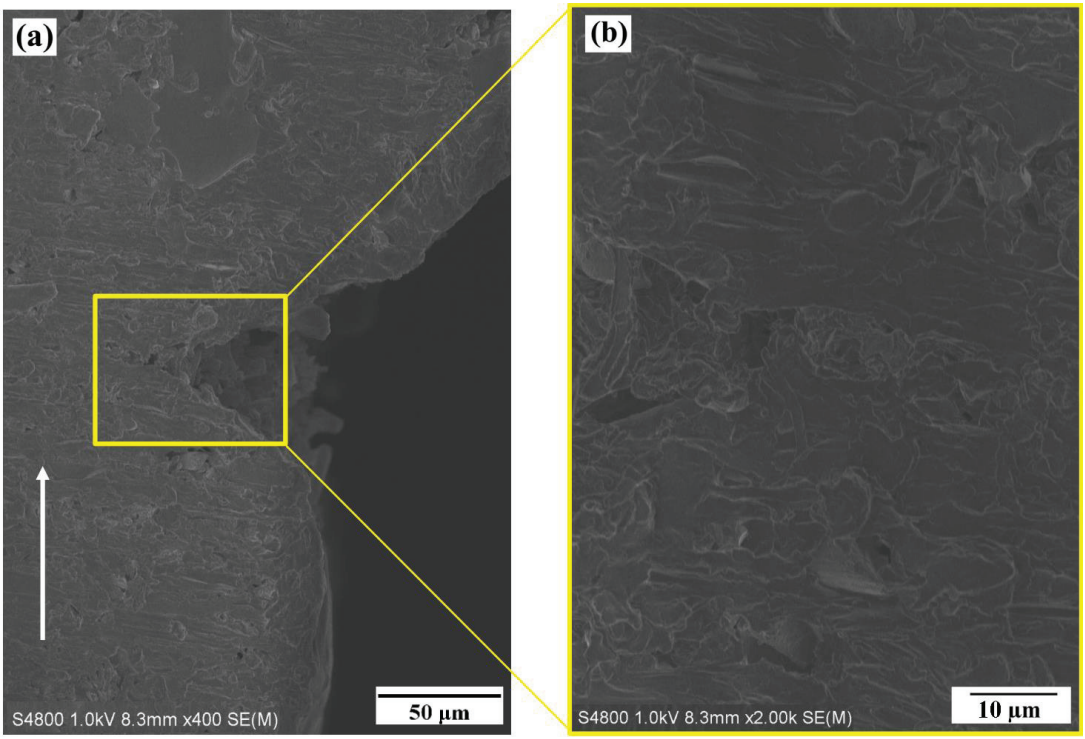

Fig. 2.11. FESEM image of vertical cross section (parallel to the building direction) showing the staircase effect with the cusp point (enclosed in a bright rectangle). The arrow indicate the building direction.

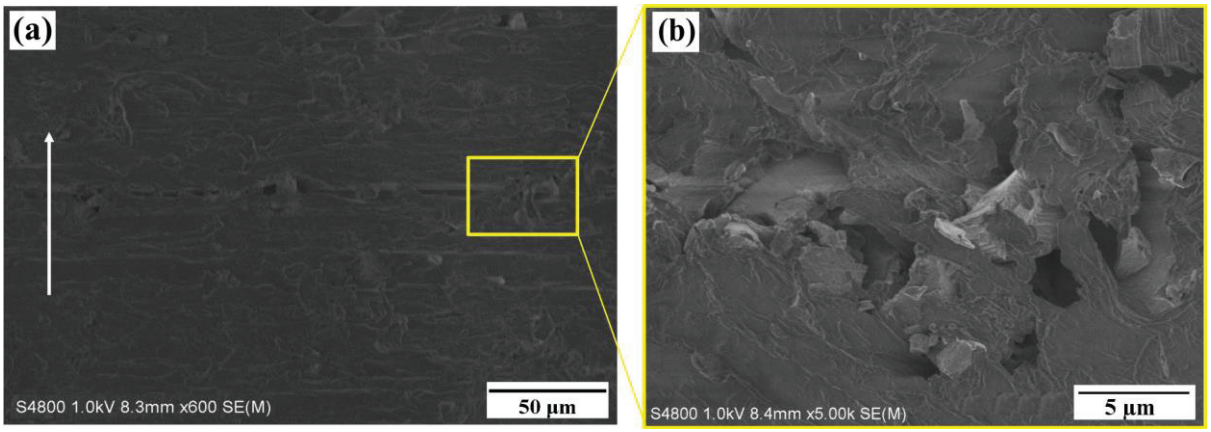

Fig. 2.12. FESEM image of vertical cross section (parallel to the building direction) showing the weak inter-layer bonding. The arrow indicate the building direction.

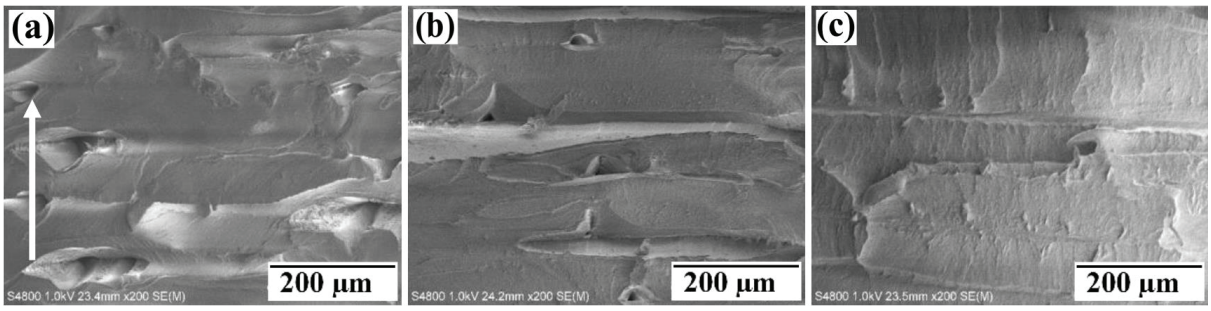

Fig. 2.13. Fracture surfaces of ABS samples printed at; printing speed (3200 mm/min), layer thickness (0.1 mm) and raster direction of (a) 0^0, (b) 45^0, and (c) 90^0. The arrow indicate the building direction.

2.4 Conclusions

In this study, the influence of process parameters such as layer thickness, printing speed, and raster direction on the surface quality, microstructure, and mechanical properties has been investigated. Minimum layer thickness promotes better surface quality and improved tensile strength for both ABS and CFR-ABS materials. Processing the samples at the optimum printing speed of 3200 mm/min and a layer thickness of 0.1 mm resulted in high tensile strength of 55.86 MPa and 49.03 MPa for 3D printed ABS and CFR-ABS samples respectively. Increase in layer thickness from 0.1 to 0.3 mm led to a decrease in tensile strength at all printing speeds. Samples printed with 15 wt% CFR-ABS material had reduced

tensile strength compared to those from ABS material. This may have been due to weak adhesion bond between the carbon fiber and the ABS matrix. Maximum tensile strength of 49.03 MPa was obtained for the 3D printed CFR-ABS samples at medium speed of 3200 mm/min. On the other hand, samples printed with ABS material at this speed (3200 mm/min) displayed the highest tensile strength (55.86 MPa). It can be deduced that, this intermediate printing speed combined with small layer thickness provides better bonding conditions and enhanced mechanical properties for both ABS and CFR-ABS composites. However, increasing or decreasing the printing speed leads to reduction in their tensile strength.

The raster direction has a great influence on the tensile strength of 3D printed ABS/CFR-ABS samples. Indeed, the 0° raster direction produced the strongest samples for all printing speeds and layer thicknesses. This is mainly because the layers are parallel to the direction in which the load is applied and could sustain more shearing loads. Conversely, parts with a raster direction of 90° were the weakest.

Samples printed at a raster direction of 0° exhibited ductile rupture dominated by dimples while those printed at raster direction of 45° and 90° had brittle rupture with the fracture surfaces characterized by quasi-cleavages and cleavage facets respectively. Entirely brittle fracture is observed for all samples printed with CFR-ABS material because, extruded carbon fiber threads within the ABS matrix break without any considerable elongation.

References

[1] Mutua, J., Nakata, S., Onda, T. and Chen, Z.C., 2017. Optimization of selective laser melting parameters and influence of post heat treatment on microstructure and mechanical properties of maraging steel. *Materials & Design*. Vol. 139, 5 Feb. 2018, Pages 486-497.

[2] Lindbäck, J.E., Björnsson, A. and Johansen, K., 2012. New Automated Composite Manufacturing Process: Is it possible to find a cost effective manufacturing method with the use of robotic equipment? In *The 5th International Swedish Production Symposium 6th-8th of November 2012 Linköping, Sweden* (pp. 523-531).

[3] Chapiro, M., 2016. Current achievements and future outlook for composites in 3D printing. *Reinforced Plastics*, *60*(6), pp.372-375.

[4] Frketic, J., Dickens, T. and Ramakrishnan, S., 2017. Automated manufacturing and processing of fiber-reinforced polymer (FRP) composites: An additive review of contemporary and modern techniques for advanced materials manufacturing. *Additive Manufacturing*, *14*, pp.69-86.

[5] Cantrell, J., Rohde, S., Damiani, D., Gurnani, R., DiSandro, L., Anton, J., Young, A., Jerez, A., Steinbach, D., Kroese, C., and Ifju, P., 2017. Experimental Characterization of the Mechanical Properties of 3D Printed ABS and Polycarbonate Parts. In *Advancement of Optical Methods in Experimental Mechanics, Volume 3* (pp. 89-105). Springer International Publishing.

[6] Ning, F., Cong, W., Qiu, J., Wei, J., and Wang, S., 2015. Additive manufacturing of carbon fiber reinforced thermoplastic composites using fused deposition modelling. *Composites Part B: Engineering*, *80*, pp.369-378.

[7] Mutua, J., Nakata, S., Akao, T., Onda, T., and Chen, Z., 2017. Influences of processing parameters on microstructure and mechanical properties of SLMed maraging steel. In *4th*

International Conference on Powder Metallurgy in Asia APMA2017 Proceedings. Hsinchu, Taiwan.

[8] Montero, M., Roundy, S., Odell, D., Ahn, S.H. and Wright, P.K., 2001. Material characterization of fused deposition modeling (FDM) ABS by designed experiments. *Society of Manufacturing Engineers*, *10*(13552540210441166).

[9] Ahn, D., Kweon, J.H., Kwon, S., Song, J., and Lee, S., 2009. Representation of surface roughness in fused deposition modelling. *Journal of Materials Processing Technology*, *209*(15), pp.5593-5600.

[10] Vasudevarao, B., Natarajan, D.P., Henderson, M., and Razdan, A., 2000, August. Sensitivity of RP surface finish to process parameter variation. In *Solid Freeform Fabrication Proceedings* (pp. 251-258).

[11] Bakar, N.S.A., Alkahari, M.R., and Boejang, H., 2010. Analysis on fused deposition modelling performance. *Journal of Zhejiang University-Science A*, *11*(12), pp.972-977.

[12] Anitha, R., Arunachalam, S., and Radhakrishnan P., 2001. Critical parameters influencing the quality of prototypes in fused deposition modelling. *Journal of Materials Processing Technology*, *118*(1–3), pp. 385–388.

[13] Bual, G.S., 2014. Methods to improve surface finish of parts produced by fused deposition modeling. *Manufacturing Science and Technology*, *2*(3), pp.51-55.

[14] Onwubolu, G. C., and Rayegani, F., 2014. Characterization and optimization of mechanical properties of ABS parts manufactured by the fused deposition modelling process. *International Journal of Manufacturing Engineering,* pp.1-13.

[15] ASTM D638- 2a: Standard Test Method for Tensile Properties of Plastics.

[16] Alexander, P., Allen, S. and Dutta, D., 1998. Part orientation and build cost determination in layered manufacturing. *Computer-Aided Design*, *30*(5), pp.343-356.

[17] Thrimurthulu, K., Pandey, P.M. and Reddy, N.V., 2004. Optimum part deposition orientation in fused deposition modeling. *International Journal of Machine Tools and Manufacture*, *44*(6), pp.585-594.

[18] Das, P., Chandran, R., Samant, R. and Anand, S., 2015. Optimum part build orientation in additive manufacturing for minimizing part errors and support structures. *Procedia Manufacturing*, *1*, pp.343-354.

[19] Moroni, G., Syam, W.P. and Petrò, S., 2015. Functionality-based part orientation for additive manufacturing. *Procedia CIRP*, *36*, pp.217-222.

[20] Wu, W., Geng, P., Li, G., Zhao, D., Zhang, H., and Zhao, J., 2015. Influence of layer thickness and raster angle on the mechanical properties of 3D-printed PEEK and a comparative mechanical study between PEEK and ABS. *Materials*, *8*(9), pp.5834-5846.

[21] Impens, D. and Urbanic, R.J., 2015. Assessing the impact of post-processing variables on tensile and compression characteristics for 3D printed components. *IFAC-PapersOnLine*, *48*(3), pp.652-657.

[22] Górski, F., Wichniarek, R., Kuczko, W., Zawadzki, P. and Buń, P., 2015. Strength of ABS parts produced by Fused Deposition Modelling technology–a critical orientation problem. *Advances in Science and Technology Research Journal*, *9*(26), pp.12-19.

Chapter 3 Optimization of Selective Laser Melting Parameters and their Influences on Microstructure and Hardness of Maraging Steel

3.1 Introduction

Selective laser melting (SLM) is one of the additive manufacturing (AM) technologies where 3D parts are generated by monotonic and selective deposition of thin layers of material through computer aided operations. This process employs 3D CAD data as a digital information source and energy in the form of high power laser beam to create 3D parts by fusing fine metallic particles together layer by layer [1]. It can produce products with complex geometries that are difficult or impossible to manufacture by conventional methods at reduced cycle time and costs. In addition, design visualization as a proof of concept and modification prior to actual fabrication is possible.

In this technique, it is required to produce parts with mechanical properties superior to or comparable with those produced by conventional processes. The mechanical properties of AM parts depend on the materials and process parameters. Improper combination of process parameters results in less dense and porous products which do not meet design specifications. Unlike conventional manufacturing techniques where the properties of finished parts are predictable, selective laser melted (SLMed) products are characterized by dynamic and unpredictable properties which are influenced by both process parameters and post treatment conditions [2]. The recent focus of AM technologies is no longer in rapid prototyping but in the generation of end-use parts. With SLM, almost 100 % dense functional parts can be produced using low cost powders such as brass, copper, Ti alloys, and stainless steels [3].

Maraging steels belong to a special class of low-carbon ultra-high-strength steels which derive their high strength not from carbon, but from precipitation of intermetallic compounds [4, 5]. Due to high strength, high toughness, good weldability, and excellent dimensional

stability, maraging steels find widespread applications in automotive, aircraft and aerospace, and tool and die industries, such as rocket motor casings and landing gears, conformal cooling channels, shafts, and fasteners [6]. SLMed maraging steels exhibit relatively lower mechanical properties in their as-built state. However, superior mechanical properties can be obtained through precipitation hardening of intermetallic compounds by aging heat-treatment [7].

The mechanical properties of SLMed parts depend to a large extent on the microstructure inherited from rapid cooling and any subsequent heat treatment subjected to them [8]. The process is governed not only by laser and scan related parameters, but also by surface morphology given by the pre-deposited layers and the stochastic particle distribution on the powder bed [9]. The solidification process and the resulting microstructure assume an important role that still needs a deeper understanding and control. Therefore, much effort is being dedicated towards demystifying the process and improving end-use part properties. To this end, SLM process parameters ought to be carefully manipulated to yield optimum conditions for desired mechanical properties.

A suitable processing window for maraging steels has not so far been established. As reported by several researchers [6, 10], the combination of process parameters is normally very wide, making it difficult to optimise the processing conditions. In addition, each process, machine type and powder material potentially creates a new set of design rules and restrictions [11]. An one-size-fits-all rule is not yet arrived at [12]. Designers come to learn of the critical design- process rule while building a deliverable AM component. This has the potential to lose money from scrapping a build, extend lead times by having a rework thus affecting customer relationship by not delivering to expectations.

In this chapter, the process parameters including laser power, scan speed, pitch, and spot diameter were varied and their effects on surface quality, relative density, microstructure, and

hardness of SLMed 18Ni maraging steel were investigated. The purpose was to optimize the process parameters and generate a process map, so as to obtain high-quality SLMed products and contribute new knowledge towards SLM of maraging steels. Therefore, a process map for the SLM of maraging steel was constructed and it was established that there existed a relatively large processing window, where sound products with relatively high relative density and good surface quality can be obtained. The optimum process conditions which resulted in maximum relative density of 99.8% and good surface roughness of 35 μm were found to be laser power of 300 W, scan speed of 700 mm/sec, and energy density of 71.43 J/mm^3 which falls within the identified processing window.

3.2 Experimental procedure

3.2.1 Sample preparation

Nitrogen gas-atomized 18Ni (300-grade) maraging steel powder (supplied by Sandvik Osprey LTD (Neath, UK)) with an average particle size of 20 μm as shown in Fig.3.1 was used as the starting material. The chemical composition of the alloy is shown in Table 3.1.

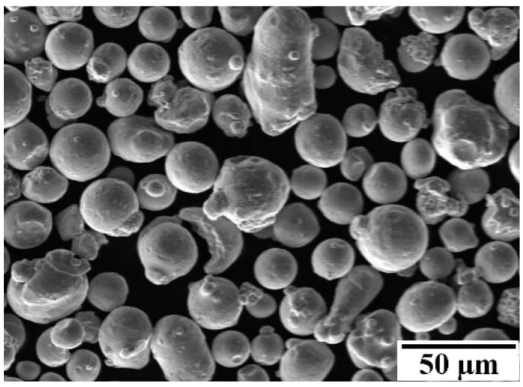

Fig. 3.1 SEM image of 18Ni (300-grade) maraging steel powder.

Table 3.1 Chemical composition of maraging steel powder used in the experiment.

Alloying element	Ni	Co	Mo	Ti	Cr	Si	Mn	Al	C	P	Fe
wt %	18.5	9.0	5.2	0.62	0.20	0.01	0.08	0.07	0.02	0.02	Balance

Matsuura LUMEX Avance-25 hybrid machine (Matsuura Machinery Corporation, Japan) equipped with Yb fiber laser was used to prepare test specimens measuring 10 mm × 10 mm × 3 mm for microstructural examinations. The design of experiment (DOE) approach was adopted in the optimization of the process parameters. Using different sets of laser power (*P*: 100 - 400 W), scan speed (*v*: 400 - 1000 mm/sec), pitch (*h*: 0.025 - 0.2 mm) and spot diameter (*d*: 0.05 - 0.3 mm), the powders were selectively melted layer after layer until the final 3D specimens were completed. For the simultaneous study of the effects of primary process parameters and derived parameters on relative density, surface roughness, hardness, and mechanical properties two separate DOE: full factorial designs; three primary factors including laser power, scan speed, and pitch with three levels resulting in 27 experimental combinations; and two derived parameters i.e., energy density and overlap rate with three levels resulting in 9 experimental combinations. The layer thickness (*t*) was maintained at 0.05 mm. The as-built specimens were removed from the steel base plate by wire EDM cutting.

3.2.2 Characterization

Before microstructure characterization, the specimens were ground using sand paper (grit size 150-1500), followed by polishing with a set of decreasing size alumina suspensions and emery cloth (3 - 1 μm) in a Doctor-lap grinding machine (Maruto Instrument Co., Ltd., Japan) and finally polished in a VibroMet® 2 vibratory polisher (Buehler, US) for 1-2 h. A non-contact laser reflectance VHX-5000 digital microscope (Keyence, Osaka, Japan) was used to evaluate the surface roughness (Ra) of the specimens. An average of six Ra

measurements was taken after filtering to eliminate background noise at each processing condition. The relative density of the specimens was determined using the Archimedes method and the results were presented as the arithmetic means of three different measurements at each processing condition. Nital solution was used to etch polished specimens for 3 - 45s. The microstructure was observed using Olympus BX60M optical microscope (OM) and JEOL JXA-8900RL (JEOL Ltd., Japan) Electron Probe Microanalyzer (EPMA)/ scanning electron microscope (SEM). Orientation imaging microscopy (OIM) analysis was performed using JOEL JSM-7001FA (JEOL Ltd., Japan) SEM equipped with an electron backscattered diffraction (EBSD) system. In order to obtain high resolution EBDS maps, vibration polishing was carried out for 2 h, and an acceleration voltage of 15 kV and scan step size of 0.1 μm were used. The OIM maps were obtained from analysis of EBSD data by the software TSL-OIM analysis 6.2. The micro-hardness (HV) values of the as-built specimens were measured using HMV-2000 micro-Vickers tester (Shimadzu Corporation, Japan) at 19.61 N and the results presented as the arithmetic means of twelve measurements at each processing condition.

3.3 Results and discussion

3.3.1 Effects of process parameters on relative density and surface morphology

The densification level is a fundamental property that determines the resultant mechanical properties of SLMed parts and influences their performance. Laser power, scan speed, pitch, and spot diameter were identified to greatly affect the relative density of SLMed specimens. Fig. 3.2 shows variations of relative density of the as-built specimens with various process parameters. At a laser power of 100 W, the relative density of the specimen was 97.9% (Fig. 3.2(a)). As the laser power increased, the relative density gradually increased, and a maximum value of 99.8% was obtained at 300 W. Beyond 300 W, the relative density

decreased to 99.2% at the maximum laser power of 400 W. It can be seen from Fig. 3.2(b) that the relative density increased from 98.4 to 99.8% as the scan speed increased from 400 to 700 mm/sec. Above 700 mm/sec, the relative density was reduced to 98.7% at the maximum scan speed of 1000 mm/sec. As shown in Fig. 3.2(c), setting the pitch at 0.025 mm resulted in a low relative density (97.0%) while increasing the pitch to 0.12 mm, the relative density rapidly increased to 99.8%. Further increase in the pitch led to small changes in relative density, for example, a slightly lower value of 99.5% was attained when the pitch equalled the spot diameter (0.2 mm).

Overlap rate, which relates to spot diameter (d) and pitch (h) as expressed by Eq. (1) [13], was used to evaluate the influences of pitch and spot diameter on relative density of as-built specimens.

$$Overlap\ rate\ (\%) = (1 - h/d) \times 100 \quad (1)$$

The results shown in Fig. 3.2(c) were obtained under the condition of d=0.2mm. When the pitch is below 0.1 mm, adjacent scan tracks are constantly intersecting (intra-layer overlapping). This track overlapping configuration produces a continuous layer as well as a continuous entity responsible for SLM powder consolidation [14]. When laser power, scan speed, and layer thickness keep constant, the absorbed energy per unit volume increases with decreasing pitch (see Eq. (2)). Therefore, too small pitch implies too much energy input, which may deteriorate surface quality as well as decrease relative density [13, 14]. On the other hand, large pitch deters proper melting of powder bed due to reduced intra-layer overlapping. Pores and separation zones (space between adjacent scan tracks when the pitch is greater than the spot diameter) may develop resulting in the decrease in relative density. At a pitch of 0.12 mm, mixed overlapping including both intra-layer and inter-layer overlapping dominates leading to increase in energy absorption between adjacent tracks and neighbouring layers. Consequently, high degree of powder fusion takes place resulting in optimum melting

regime and very high relative density (99.8%). Fig. 3.2(d) shows that, a spot diameter of 0.025 mm (less than the pitch) resulted in a low relative density (95.9%). This is because, small spot diameter fused narrower scan tracks (with gaps between adjacent tracks) constituting pores and the reduced relative density. Increase in the spot diameter led to increase in the relative density to 98.8% at d= 0.075 mm. The relative density remained almost constant with increase in spot diameter up to 0.2 mm (default spot diameter) where it peaks at 99.8%. However, further increase in spot diameter led to a drop in relative density. Critically low relative density of 92.7% was obtained at a spot diameter of 0.3 mm. This is because as the spot diameter increases, the powder-laser contact area is increased yet the energy delivered to melt the powder remains constant. This tends to lower the melting efficiency and may compromise on the fusion process leading to intra-layer and/or inter-layer porosity. These findings are confirmed further by considering the relationship between relative density and overlap rate shown in Fig. 3.2(e).

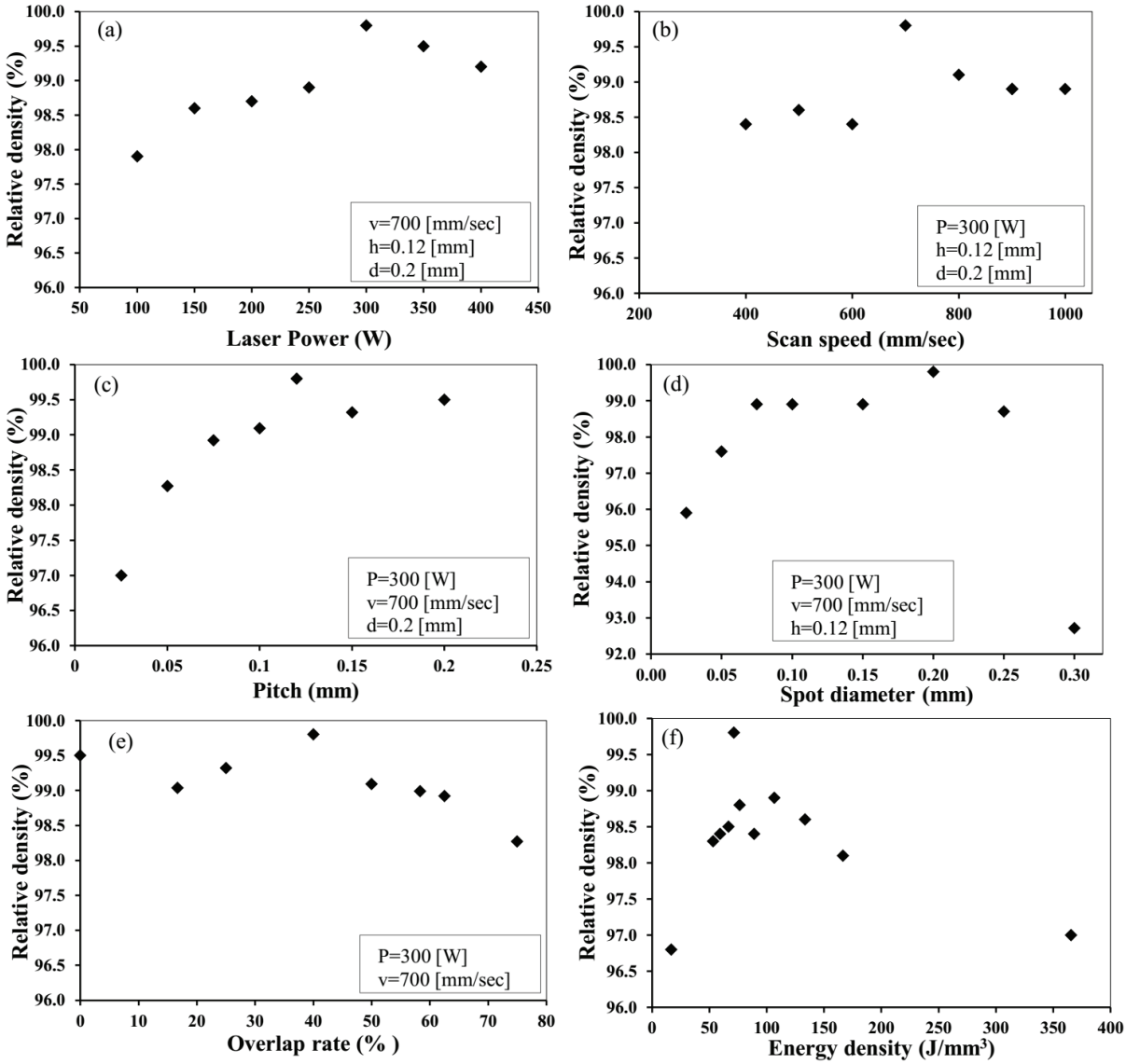

Fig. 3.2 Effects of process parameters on relative density of as-built SLMed specimens.

When the spot diameter is equal to the pitch (0% overlap), a high relative density (99.5%) was obtained (Fig. 3.2(e)). This is because even at zero percent overlap, the width of the laid track is larger than the focused laser spot diameter due to the heat transferred to the powder bed. This may produce good track-to-track merging characterized by fewer pores (high relative density) and better surface for the finishing passes in the SLM process. It is evident that increase in overlap rate to 16.7% leads to a slight decrease in relative density before increasing to a maximum of 99.8% at 40% overlap. It is likely that some pores and

separation zones are formed along the length of the scan tracks causing the reduction in relative density. Similar phenomenon has also been reported by Pupo *et al* [15] at an overlap rate of (20±11.99) %. A maximum relative density of 99.8% was obtained at 40% overlap (Fig. 3.2(e)). This is occasioned by optimal re-melting of scan tracks, which ensures effective molten powder consolidation and conversion into tracks each perfectly cohesive with one another resulting in the maximum relative density. However, further increase in overlap rate resulted in drastic reduction in relative density. Low relative density (98.3%) was obtained at 75% overlap, because a larger overlap rate may cause multiple re-melting of scan tracks due to large energy density. As such, some elements with low melting points may vaporize leaving blow holes or pores hence the reduction in relative density.

Energy density (E) is an important parameter in SLM. It relates to laser power (P), scan speed (v), pitch (h), and layer thickness (t) and can be calculated using Eq. (2) [2, 16].

$$E = P/(vht) \tag{2}$$

The amount of laser energy delivered should be large enough for the powders to completely melt, undergo epitaxial solidification, and form fully dense parts. As shown in Fig. 3.2(f), higher energy density resulted in higher relative density. However, excessively high energy density caused reduction of relative density of the SLMed specimens. The maximum relative density attained was 99.8% at an energy density of 71.43 J/mm^3, which corresponds to scan speed of 700 mm/sec and laser power of 300 W. Processing the specimens at very low energy density (16.67 J/mm^3) and exceedingly high energy density (365.71 J/mm^3) resulted in low values of relative density.

Fig. 3.3 shows the optical microscopy (OM) images on the horizontal (top views perpendicular to the building direction) and vertical (side views parallel to the building direction) cross sections of as-built specimens, revealing the pore distributions and relative density values under different conditions of energy density and laser power. Clearly, a lot of

pores remained in the specimen built at low energy density and laser power. The pores are larger and more irregular in the horizontal cross section than in the vertical section (Sample 7 shown in Fig. 3.3(a) and (b) respectively).

It seems that the irregularly shaped pores are oriented along the scanning direction in the horizontal section (Fig. 3.3(a)), and along the building direction in the vertical section (Fig. 3.3(b)). At high energy density and laser power, numerous pores still persisted. The excessive energy per unit volume may cause the formation of large melt pool, vaporization of some elements with low melting points, and escaping of entrapped gases during the cooling cycle. These result in almost round pores as shown in Sample 3 (Fig. 3.3(a) and (b)). Samples 3, 7, and 9 in Fig. 3.3(a) and (b) had relative density values of less than 98% and showed large and irregular shaped pores. On the other hand, both cross sections as shown in Samples 1, 2, 4, 6, and 8 had relative density of 98.4 - 98.9% and displayed small closed and homogenously distributed pores with almost regular shape. Sample 5 had the maximum relative density of 99.8% and had hardly any pores.

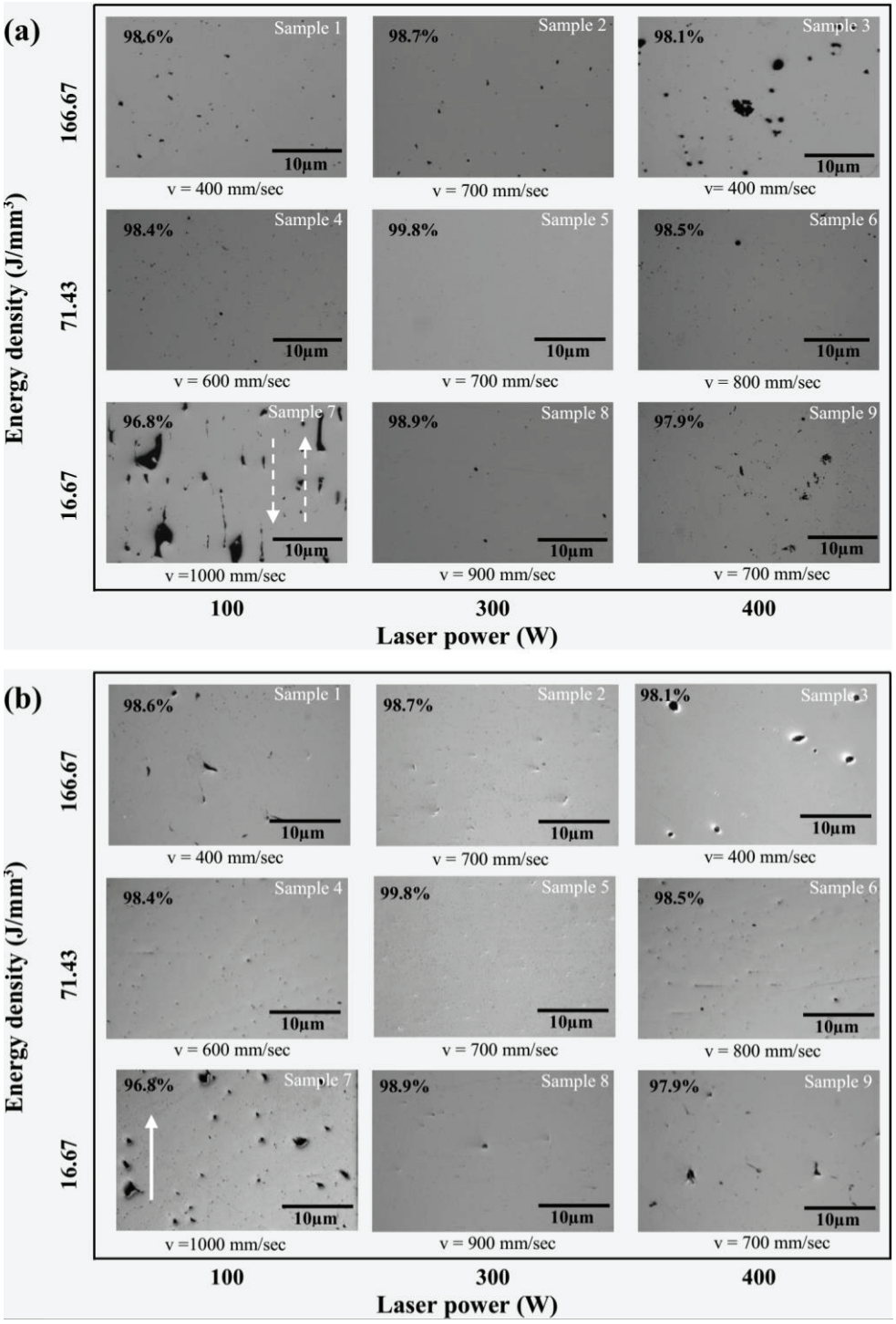

Fig. 3.3 OM images on (a) horizontal (b) vertical cross sections of as-built specimens showing the distribution of pores and changes in relative density with variations in energy density, laser power, and scan speed. The dotted arrows indicate laser scanning direction while the solid arrow indicates the building direction.

The SEM images in Fig. 3.4 show the top-surface morphologies of the as-built

specimens. Rougher surfaces were observed at the minimum (16.67 J/mm^3) and maximum (166.67 J/mm^3) values of energy density, as shown in Fig. 3.4(a) and (c), respectively. At lower energy density, insufficient fusion causes the formation of distinct scan tracks with visible gaps (as indicated by the arrows in Fig. 3.4(a)) between two neighboring scan tracks. Moreover, some powder particles (marked by a rectangle) can be seen on the surface. These particles are believed to arise from un-melted powder due to lower energy density, which results in low relative density of the as-built specimen. On the other hand, some larger spherical particles (balls) remained on the surface (Fig 3.4(c)) under the conditions of high energy density. Similar particles appear small in both size and number on the as-built specimen processed at optimum condition (Fig. 3.4(b)). The formation of spherical particles/balls during SLM process, termed as balling phenomenon, is believed to result from shrinkage of melted track so as to reduce surface energy under the action of surface tension [17]. It has been categorized as a typical microstructural defect in SLMed parts [17, 18] and is inevitable in most powder bed fusion methods of additive manufacturing technologies. The main causes of balling include low energy density and high thermal gradient, capillarity instabilities, poor wettability of molten powder, and large melt pool accompanied by prolonged cooling time [18-22].

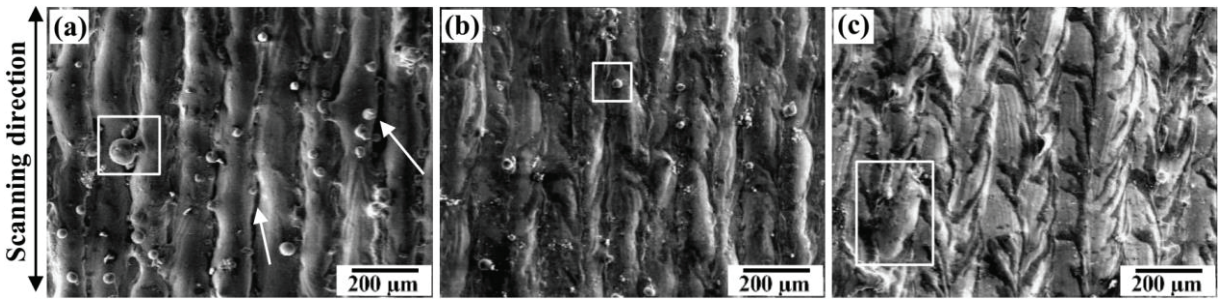

Fig. 3.4 SEM images on top surfaces of as-built specimens processed at (a) minimum (16.67 J/mm^3), (b) optimum (71.43 J/mm^3), and (c) maximum (166.67 J/mm^3) energy density. The arrows indicate gaps between scan tracks while the rectangles show resultant surface balling.

As depicted in Fig. 3.4(c), newly formed larger particles appear on the surface, which is believed to be due to the formation of large melt pool and prolonged cooling time at the maximum energy density resulting in spheroidization (balling) of the melt pool. Proper fusion was attained at the optimum energy density (71.43 J/mm^3) accounting for the reduced balling and well spread scan tracks (Fig. 3.4(b)). Accordingly, relatively smooth surface with a roughness value of Ra= 35 μm was obtained under this optimum condition while poor surface qualities were attained at low and high values of energy density (Fig. 3.5).

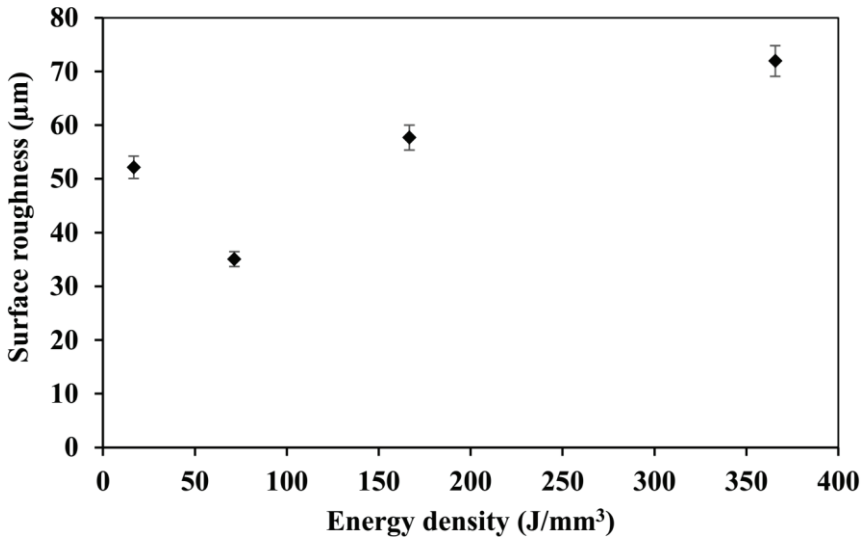

Fig. 3.5 Variations of surface roughness of as-built specimens with energy density.

3.3.2 Process parameter optimization and processing window demarcation

According to the above results in Section 3.3.1, a process map with schematic illustration of the SLM process for maraging steel powders can be obtained as shown in Fig. 3.6. The intra-layer (dark ovals at the intersections between two adjacent scan tracks) and inter-layer (bright ovals at the intersections between neighboring layers) overlapping phenomena that cause powder fusion is also highlighted. Clearly, there exist several processing regions which correspond to different relative density values, microstructure, and hence mechanical properties of the SLMed products. Significantly low energy input is

experienced in Region I due to low laser power and scan speed. As a result, insufficient melting gives rise to low quality products with high porosity and poor mechanical strength. Slight increases in both laser power and scan speed cause an increase in the energy input in Region II. This causes limited fusion of the powders resulting in distinct scan tracks and pronounced surface balling as shown in Fig. 3.4(a). A relatively large processing window is obtained in Region III (forming zone) where adequate powder fusion occurs. The laser power and scan speed in this region are high enough to cause proper fusion of the powders resulting in sound products with relatively high density, flatter scan tracks, and improved surface finish. Our experimental results revealed that the relative density values of the samples obtained range from 98 to 99% in this region. Within Region III, there is a limited zone, Region IV, which provides optimum processing region where the SLM products have high density and good surface quality. The relatively high laser power and scan speed in this region enable proper fusion of the powders, thus leading to high relative density values of more than 99% and well-spread scan tracks with good surface quality. In fact, the as-built specimens with very high relative density (99.8%) and good surface roughness (35 μm) (Fig. 3.4(b)) were obtained at a laser power of 300 W, scan speed of 700 mm/sec, and energy density of 71.43 J/mm^3 which falls within this region. Regions V and VI represent high energy input zones, where high energy density is delivered causing excessive powder fusion. This may result in well-spread scan tracks, large melt pools, and large surface balling due to the rapid cooling cycle during SLM process (see Fig. 3.4(c)). At a laser power of larger than 400 W, the energy input is so high that the product surfaces are burnt.

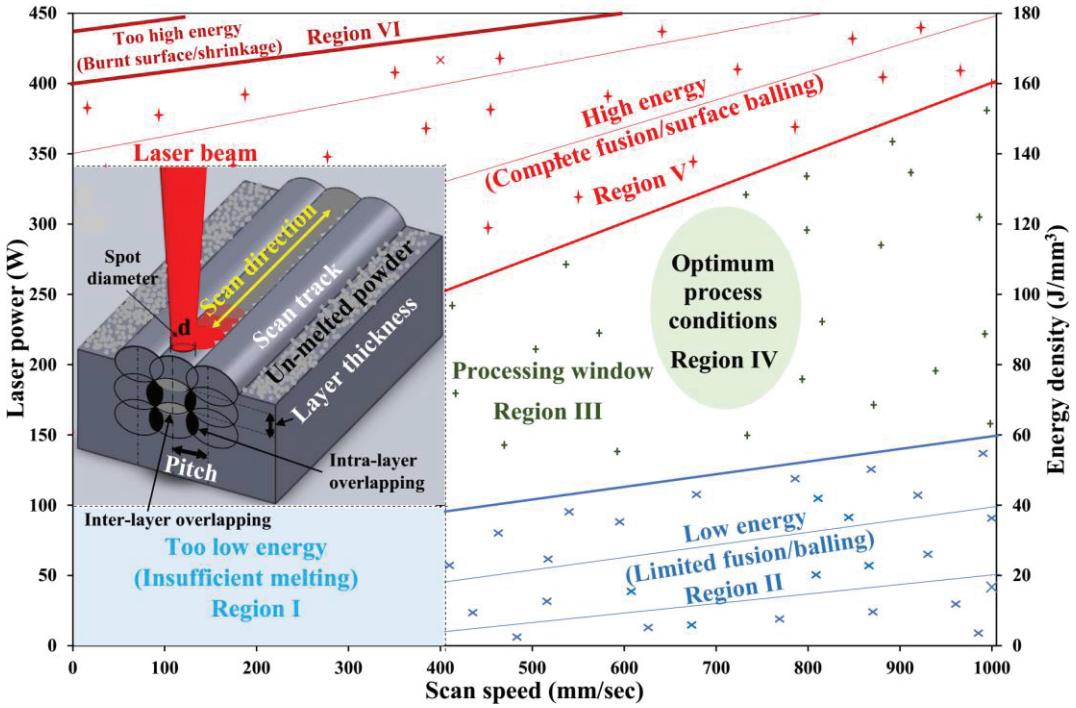

Fig. 3.6 Schematic illustration of SLM process integrated with a process map that relates laser power, scan speed, and energy density.

3.3.3 Effects of process parameters on microstructure and hardness of as-built specimens

The horizontal cross-sectional OM image of polished/etched as-built specimen shown in Fig. 3.7(a) revealed clear scan tracks and discontinuous nature of the melting process induced by pulsating laser beam. Typical semi-elliptical scan tracks of solidified melt pools with long axis parallel to the building direction (due to deep melt pool), and the overlapping among different scan tracks were observed on the vertical cross section (parallel to the building direction) shown in Fig. 3.7(b). During SLM, thermal gradient is maximum at the leading edge of the laser beam and the scan track growth is proportional to thermal gradient. Therefore, scan tracks cool faster at the leading edge of the laser beam resulting in their semi-elliptical shape. The dark regions between scan tracks reveal the heterogeneous distributions of the alloy elements in the as-built specimens. Besides, the overlapping laser beam (re-scanning) may introduce high energy at the intersections thereby depleting some elements [22]. The complicated thermal processes experienced during SLM lead to cellular

solidification structure and epitaxial growth across different track boundaries.

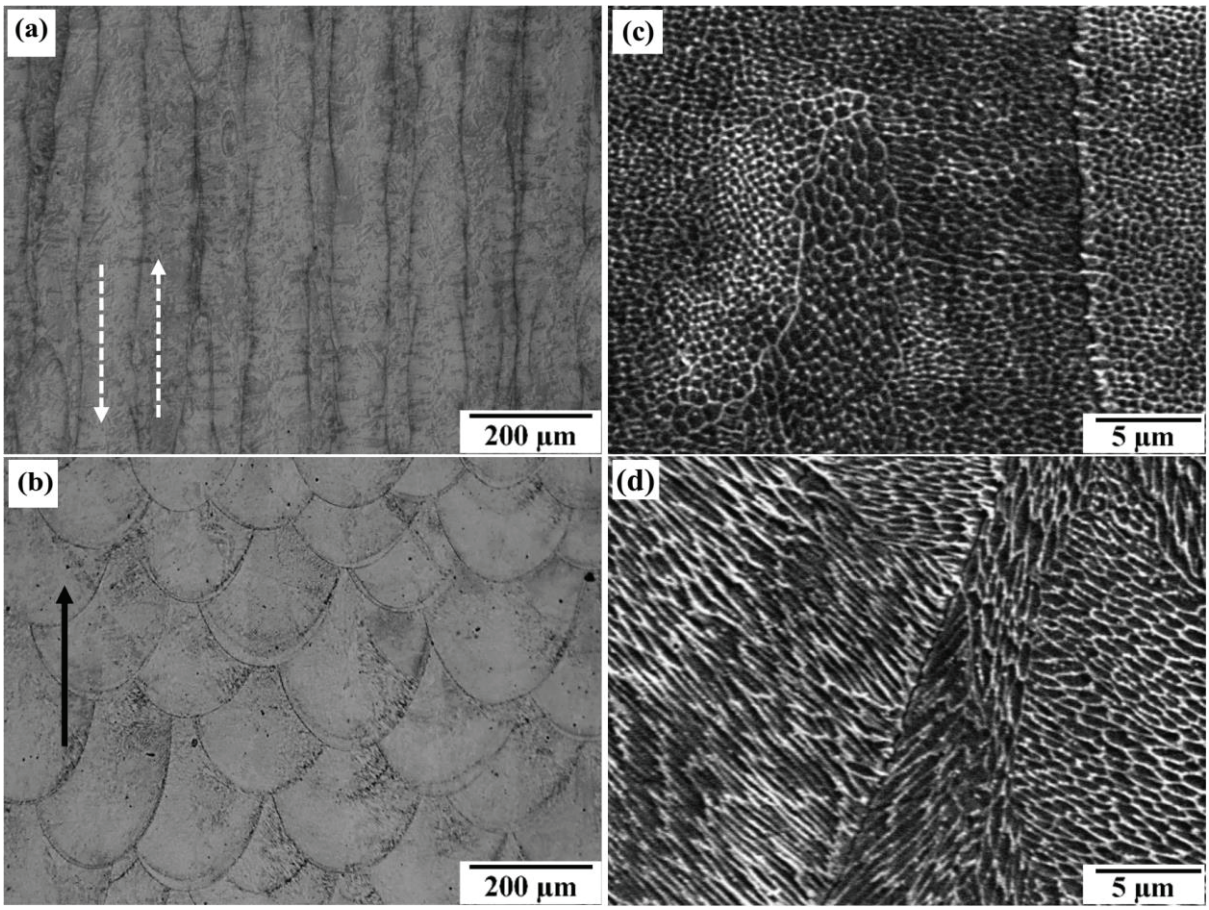

Fig. 3.7 (a) Horizontal and (b) vertical cross-sectional OM images, (c) horizontal and (d) vertical cross-sectional SEM images of as-built specimen fabricated at optimum process conditions. Bright dotted arrows show the laser scanning direction while the dark solid arrow indicates the building direction.

As shown in Fig. 3.7(c), the horizontal cross section of the as-built specimen consists of submicron sized cellular microstructure with intercellular spacing less than 1µm. This contributes to the excellent strength and hardness in SLMed maraging steel parts compared to their conventional counterparts. On the other hand, the microstructure in the vertical cross section (Fig. 3.7(d)) of the as-built specimen is characterized by fine columnar and/or dendritic grains due to rapid solidification of melt pool. The grains propagated away from the grain boundaries due to existence of higher thermal gradient at these interfaces.

Fig. 3.8 shows the EBSD data on horizontal cross section of the as-built specimen. From the phase map shown in Fig. 3.8(a), the as-built specimen was not fully martensitic as trace amount of γ phase remained. The high cooling rates exhibited during solidification resulted in the formation of predominantly martensite matrix and prohibited the precipitation of the intermetallic compounds. However, some alloying elements such Ni, Co, Mo, etc., remained in supersaturated solution (γ –phase) resulting in the trace amounts of austenite. The IPF map in Fig. 3.8(b) show the grain size, shape and orientation of the as-built specimen processed at the optimum conditions. The average grain size of the as-built specimen was 0.982 ± 0.961 μm. Clearly, it seems that some grains in the as-built specimen were oriented along the laser scanning direction (Fig. 3.8(b)), this might be the result of solidification of the melt pool because the temperature gradient reaches the maximum at the leading edge of the laser beam. The grain boundary map shown in Fig. 3.8(c) indicated that the as-built specimen had higher fraction (51.6%) of small angle grain boundaries (SAGBs) with misorientation angles of <15°. This may be due to its fine grain microstructure resulting from rapid epitaxial solidification during SLM process.

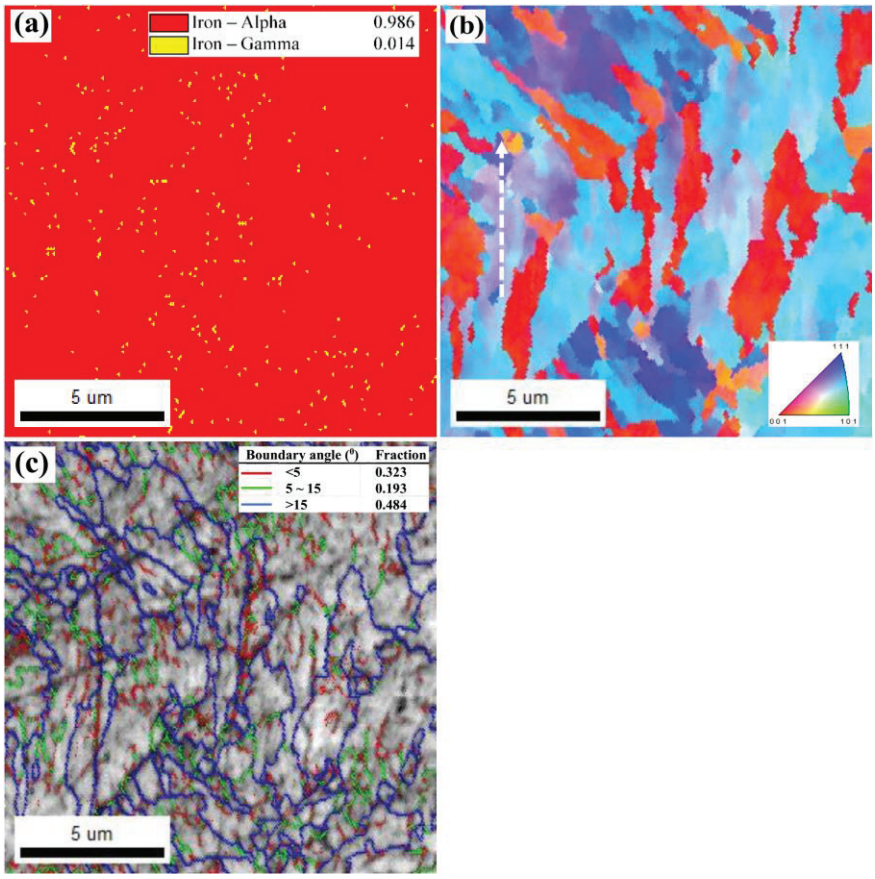

Fig. 3.8 EBSD data (a) phase, (b) IPF, and (c) grain boundary maps on horizontal cross sections of as-built specimen. Bright dotted arrow shows the laser scanning direction.

The variations of Vickers hardness of the as-built specimen as a function of energy density is shown in Fig. 3.9. It is evident that processing the specimen at low and high values of energy density resulted in low hardness values. The as-built specimens had Vickers hardness values ranging from 330-403 HV depending on the processing energy density. These values are characteristically higher compared with 280 HV of wrought maraging steel in as-built state [6].

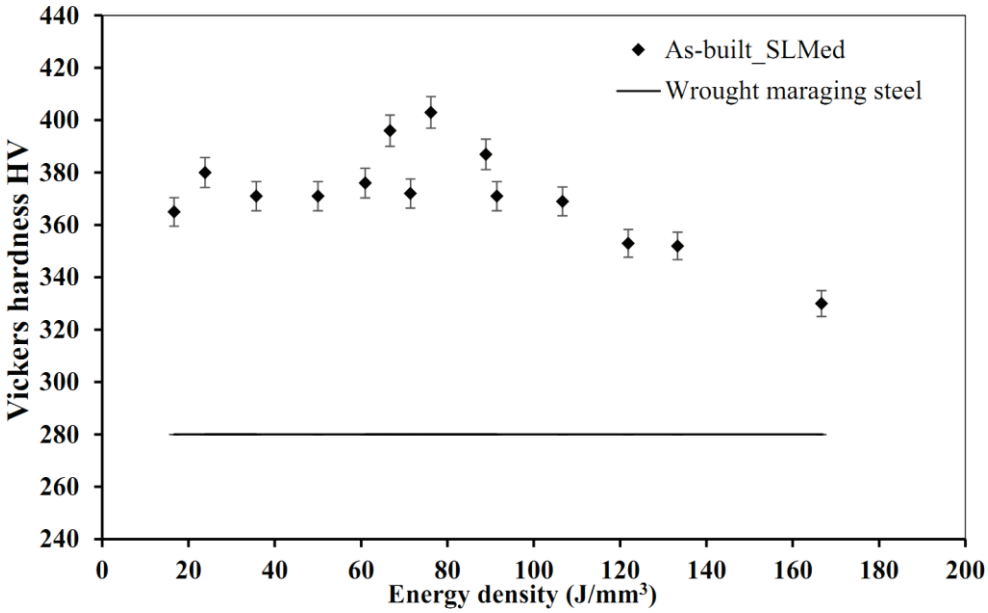

Fig. 3.9 Variations of Vickers hardness of as-built specimen as a function of energy density.

The high Vickers hardness value in SLMed maraging steel parts in as built state is attributed to the fine grain microstructure with intercellular spacing less than 1μm and the numerous small angle grain boundaries (SAGBs) with misorientation angles <15°, see Fig. 3.7(c) and (d) and Fig. 3.8(c). These small micron-sized intragranular sub-grains impede and block dislocation motion imposing a hardening effect on the as-built specimen.

3.4 Conclusions

In this chapter, the influence of process parameters, such as scan speed, laser power, spot diameter and pitch, on densification behavior and surface morphology of SLMed maraging steel has been investigated and a process map has been constructed. In the SLM of 18Ni maraging steel, there exists a relatively large processing window, where sound products with relatively high relative density, flatter scan tracks, and good surface quality can be obtained. For example, the optimum process conditions were found to be scan speed of 700 mm/sec, laser power of 300 W, overlap rate of 40%, and energy density of 71.43 J/mm^3.

These resulted in a maximum relative density of 99.8% and good surface quality with a roughness value of Ra= 35 μm. The as-built specimen was not fully martensitic since trace amount of γ phase remained after the solidification process. The average grain size of the as-built specimen was 0.982 ± 0.961 μm and were basically oriented along the laser scanning direction. Moreover, as-built specimen consists of submicron sized cellular microstructure with intercellular spacing less than 1μm. This contributes to the excellent strength and hardness in SLMed maraging steel parts. Processing the specimen at low and high values of energy density resulted in low hardness values. Vickers hardness values ranging from 330-403 HV were obtained in this study. These values were much higher that 280 HV of conventional maraging steel in the same state.

References

[1] Mutua, J., Nakata, S., Akao, T., Onda, T., and Chen, Z., 2017. Influences of processing parameters on microstructure and mechanical properties of SLMed maraging steel. In *4th International Conference on Powder Metallurgy in Asia APMA2017 Proceedings*. Hsinchu, Taiwan.

[2] Casalino, G., Campanelli, S.L., Contuzzi, N. and Ludovico, A.D., 2015. Experimental investigation and statistical optimisation of the selective laser melting process of a maraging steel. *Optics Laser Technology*, *65*, pp.151-158.

[3] Stwora, A. and Skrabalak, G., 2013. Influence of selected parameters of Selective Laser Sintering process on properties of sintered materials. *Journal of achievements in materials and manufacturing engineering*, *61*(2), pp.375-380.

[4] Habby, F., Siddiqui, T. N., Khan, S.H., ul Haq, A., and Kham, A. Q., 1992. Austenite determination by eddy current measurements in maraging steel. *NDT & I International*, *25*(3), pp.145-146.

[5] Marcisz, J. and Stępień, J., 2014. Short-time aging of MS350 maraging steel with and without plastic deformation. *Archives of Metallurgy and Materials*, 59(2), pp. 513-520. Retrieved 18 Apr. 2017, from doi:10.2478/amm-2014-0085.

[6] Kempen, K., Yasa, E., Thijs, L., Kruth, J.P. and Van Humbeeck, J., 2011. Microstructure and mechanical properties of Selective Laser Melted 18Ni-300 steel. *Physics Procedia*, *12*, pp.255-263.

[7] Tan, C., Zhou, K., Tong, X., Huang, Y., Li, J., Ma, W., Li, F. and Kuang, T., 2016. Microstructure and Mechanical Properties of 18Ni-300 Maraging Steel Fabricated by Selective Laser Melting.

[8] Casati, R., Lemke, J.N., Tuissi, A. and Vedani, M., 2016. Aging Behaviour and Mechanical Performance of 18-Ni 300 Steel Processed by Selective Laser Melting. *Metals*, *6*(9), p.218.

[9] Bauereiß, A., Scharowsky, T., Körner, C., 2014. Defect generation and propagation mechanism during additive manufacturing by selective laser melting. *Journal of Material Processing Technology, 214*, pp. 2522–2528.

[10] Gokuldoss, P.K., Kolla, S. and Eckert, J., 2017. Additive Manufacturing Processes: Selective Laser Melting, Electron Beam Melting and Binder Jetting—Selection Guidelines. *Materials*, *10*(6), p.672.

[11] Thompson, M.K., Moroni, G., Vaneker, T., Fadel, G., Campbell, R.I., Gibson, I., Bernard, A., Schulz, J., Graf, P., Ahuja, B. and Martina, F., 2016. Design for Additive Manufacturing: Trends, opportunities, considerations, and constraints. *CIRP Annals-Manufacturing Technology*, *65*(2), pp.737-760.

[12] Caitlin, O., 2017. Designing for Additive Manufacturing, Part II: Consideration for Manufacturability. *Precision Metal Forming Association, 3D Metal Printing Magazine,* winter 2017 *2(1),* pp. 26-28.

[13] Hong, M.H., Min, B.K. and Kwon, T.Y., 2016. The Influence of Process Parameters on the Surface Roughness of a 3D-Printed Co–Cr Dental Alloy Produced via Selective Laser Melting. *Applied Sciences*, *6*(12), p.401.

[14] Su, X. and Yang, Y., 2012. Research on track overlapping during selective laser melting of powders. *Journal of materials processing technology*, *212*(10), pp.2074-2079.

[15] Pupo, Y., Serenó, L., Delgado, J. and Ciurana, J., 2013, September. Study of the surface quality in multi-track to Selective Laser Melting with CoCrMo powders. In *High Value Manufacturing: Advanced Research in Virtual and Rapid Prototyping:*

Proceedings of the 6th International Conference on Advanced Research in Virtual and Rapid Prototyping, Leiria, Portugal, 1-5 October, 2013 (p. 273). CRC Press.

[16] Pilipović, A., Valentan, B., Brajlih, T., Haramina, T., Balič, J., Kodvanj, J., Šercer, M. and Drstvenšek, I., 2010. Influence of laser sintering parameters on mechanical properties of polymer products. In *3rd International Conference on Additive Technologies iCAT2010 Proceedings*. DAAAM International, Vienna.

[17] Gu, D.D., Meiners, W., Wissenbach, K. and Poprawe, R., 2012. Laser additive manufacturing of metallic components: materials, processes and mechanisms. *International materials reviews*, *57*(3), pp.133-164.

[18] Cherry, J.A., Davies, H.M., Mehmood, S., Lavery, N.P., Brown, S.G.R. and Sienz, J., 2015. Investigation into the effect of process parameters on microstructural and physical properties of 316L stainless steel parts by selective laser melting. *The International Journal of Advanced Manufacturing Technology*, *76*(5-8), pp.869-879.

[19] Das, S., 2003. Physical aspects of process control in selective laser sintering of metals. *Advanced Engineering Materials*, *5*(10), pp.701-711.

[20] Simchi, A. and Pohl, H., 2003. Effects of laser sintering processing parameters on the microstructure and densification of iron powder. *Materials Science and Engineering: A*, *359*(1), pp.119-128.

[21] Kruth, J.P., Froyen, L., Van Vaerenbergh, J., Mercelis, P., Rombouts, M. and Lauwers, B., 2004. Selective laser melting of iron-based powder. *Journal of Materials Processing Technology*, *149*(1), pp.616-622.

[22] Campanelli, S.L., Contuzzi, N., Angelastro, A. and Ludovico, A.D., 2010. Capabilities and performances of the selective laser melting process. In *New Trends in Technologies: Devices, Computer, Communication and Industrial Systems*. InTech.

Chapter 4 Effects of Post Heat Treatment on Microstructure and Mechanical Properties of Selective Laser Melted Maraging Steel

4.1 Introduction

Selective laser melted maraging steel specimens have been successfully fabricated using the optimum process parameters in Chapter 3. The SLMed specimens have excellent relative density of 99.8% and remarkable surface quality. However, their mechanical properties are quite low and therefore need further improvement. As a matter of fact, the mechanical properties of SLMed parts depend to a large extend on the microstructure inherited from the rapid cooling and any subsequent heat treatment subjected to them [1]. In addition, the complex thermal cycle exhibited during SLM cause an epitaxial solidification process which gives rise to fine microstructure in the as-built parts. This provide considerably high level of strength and hardness than that of conventionally manufactured counterparts in the non-heat-treated state [2]. The microstructure dynamics in maraging steel make them better candidates for SLM and applications in aerospace, tool and die making, and automotive industries [3, 4]. Maraging is a term coined from the martensite age hardening of low-carbon, iron-nickel lath martensite. These category of steels are dominated by martensite matrix and hence the only transformation that occurs at ordinary cooling rates is martensite formation. However, under some processing conditions such as SLM and aging, a duplex phase structure consisting of metastable martensite and austenite equilibrium phases may arise [5]. The martensite without carbon is quite soft, but heavily distorted by a high dislocation density. Hardening and strengthening of these steels are subsequently produced by aging the as-built parts for several hours at 450-510 °C, caused by precipitation of intermetallic phases such as Ni_3 (Ti, Mo) and the formation of a more stable phase Fe_2Mo that demands higher exposure times [4]. By subjecting the as-built SLMed specimens to post heat treatments such as solution treatment

and aging, the microstructure can be carefully controlled and the mechanical properties significantly improved to match or exceed those fabricated by conventional means [5]. Many earlier studies on maraging steels have focused on the precipitation behaviour and the effect of austenite reversion during the maraging heat treatment [1, 3, 6-11]. According to the researchers, segregation and precipitation of Ni, Mo, and Ti may occur at the grain boundaries due to different localized processing temperatures leading to formation of supersaturated solid solution (austenite phase) with the martensite matrix [3, 9, 11]. They asserted that, presence of reversed austenite in the SLMed parts could lead to reduced hardness, yield strength, and ultimate tensile strength but it would enhance the tensile ductility and impact strength in the initial stages of overaging [1, 12]. Therefore, as a remedy to austenite reversion, solution treatment and appropriate aging conditions ought to be adopted. With this in mind, the purpose of this chapter was to investigate the effects of solution treatment and aging heat treatment on the microstructure and mechanical properties of SLMed maraging steels.

In the current work solution treatment at 820 °C for 1 h followed by aging at 460 °C for 5 h lead to significant improvement in hardness, yield strength, tensile strength and the Young's modulus. These were attributed to the elimination of austenite phase during solution treatment and the precipitation of fine intermetallic compounds in the martensite matrix during the aging process.

4.2 Experimental procedure

4.2.1 Sample preparation

Nitrogen gas-atomized 18Ni (300-grade) maraging steel powder with an average particle size of 20 μm was used as the starting material. The chemical composition of the alloy is shown in Table 3.1. Matsuura LUMEX Avance-25 hybrid machine (Matsuura Machinery

Corporation, Japan) equipped with Yb fiber laser was used to prepare test specimens measuring 10 mm × 10 mm × 3 mm for microstructural examinations. Using different sets of laser power (*P*: 100 - 400 W), scan speed (*v*: 400 - 1000 mm/sec), pitch (*h*: 0.025 - 0.2 mm) and spot diameter (*d*: 0.05 - 0.3 mm), the powders were selectively melted layer after layer until the final 3D specimens were completed. The layer thickness (*t*) was maintained at 0.05 mm. In order to examine the effect of building direction on mechanical properties, horizontally and vertically oriented sheet tensile specimens with a gauge section of 34 mm in length, 6 mm in width, and 3 mm in thickness as shown in Fig. 4.1 were built with a set of process parameters chosen in terms of maximal density of as-built specimens and optimal laser energy density. The as-built specimens were removed from the steel base plate by wire EDM cutting.

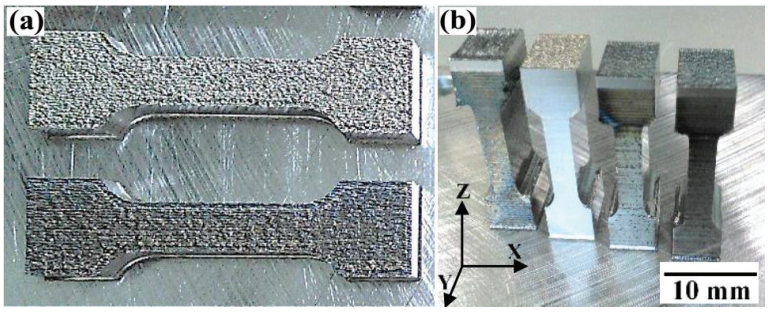

Fig. 4.1 (a) Horizontally and (b) vertically oriented standard tensile specimens fabricated at selected process parameters with Z and X axes as the building and laser scanning directions respectively.

4.2.2 Heat treatment

Some specimens were solution-treated (STed) at 820 °C for 1 h. Using design of experiment (DOE) approach, the specimens were aged at 460 - 600 °C for 0.5 - 24 h then cooled to room temperature.

4.2.3 Chacterization

Before microstructure characterization, the specimens were ground using sand paper (grit size 150-1500), followed by polishing with a set of decreasing size alumina suspensions on an emery cloth up to 1 μm in a Doctor-lap grinding machine (Maruto Instrument Co., Ltd., Japan) and finally polished in a VibroMet® 2 vibratory polisher (Buehler, US) for 1-2 h. Nital solution was used to etch polished specimens for 3 - 45s. The microstructure of the as-built, solution treated, and solution treated and aged specimens was then observed using Olympus BX60M optical microscope (OM) and JEOL JXA-8900RL (JEOL Ltd., Japan) Electron Probe Microanalyzer (EPMA)/ scanning electron microscope (SEM). Orientation imaging microscopy (OIM) analysis was performed using JOEL JSM-7001FA (JEOL Ltd., Japan) SEM equipped with an electron backscattered diffraction (EBSD) system. In order to obtain high resolution EBDS maps, vibration polishing was carried out for 2 h, and an acceleration voltage of 15 kV and scan step size of 0.1 μm were used. The OIM maps were obtained from analysis of EBSD data by the software TSL-OIM analysis 6.2. Phase identification was performed by X-ray diffraction (XRD, Rigaku, JAPAN) with Cu Kα radiation, in step scan mode with step size of 0.02°, time per step 3s, and angular interval 30-90°. The micro-hardness (HV) values of the as-built and aged specimens were measured using HMV-2000 micro-Vickers tester (Shimadzu Corporation, Japan) at 19.61 N and the results presented as the arithmetic means of twelve measurements at each processing condition. Tensile tests were carried out on the horizontally and vertically oriented specimens in as-built and solution treated and aged (STAed) conditions. The surfaces of all tensile specimens were polished until #1500 emery paper to reduce surface flaws. The tensile tests were performed at room temperature with a crosshead speed of 1 mm/min (corresponding to an initial strain rate of $4.90 \times 10^{-4} s^{-1}$) using a 50 kN Shimadzu universal testing machine. The strain was determined by measuring machine crosshead displacement during the tensile tests. At the same time, the

strain in the elastic deformation regions was simultaneously measured with a KFG-1-120-C1-23 strain gage (Kyowa, Japan). At least three specimens for each condition were tested. In addition, fractographic examinations on the tensile tested specimens were done to evaluate the failure behavior.

4.3 Results and discussion

4.3.1 Microstructure of as-built as well as solution-treated and aged specimens

Fig. 4.2 illustrates the XRD patterns of the raw powder, as-built, aged, and solution-treated/aged (STAed) specimens. Although the atomized maraging steel powder only contains the martensite (α') phase, a small peak corresponding to $(220)_\gamma$ of the austenite (γ) phase appears in the as-built specimen. After aging at 460 °C for 5 h, the intensity of $(220)_\gamma$ peak becomes stronger, revealing the formation of more γ phase during the aging. This suggests that the phase transformation from α' to γ occurs during the aging process. Furthermore, when as-built specimen was subjected to solution treatment (ST), the $(220)_\gamma$ peak completely disappeared, indicating that γ phase formed during ST at 820 °C is completely transformed into α' phase during cooling process. This is due, in part, to non-uniform processing temperatures throughout SLM process, which causes the martensite phase in the starting powder to transform into austenite during SLM. The segregation and heterogeneous distributions of alloying elements may promote reversion of martensite to austenite during cooling process. Similar phenomenon has also been found in some work [6, 8]. However, the solution treatment at 820 °C, which is higher than the austenite finish temperature (750 °C), makes the alloying elements to homogeneously dissolve into austenite solid solution. In the subsequent cooling, the austenite phase can be transformed into martensite completely (the martensite start temperature (M_s) and finish temperature (M_f) are 164 °C and 61 °C, respectively [4]).

On the other hand, when the STed specimens were subjected to aging at 460 – 600 °C for 0.5 – 5 h, no α'→γ phase transformation occurred and the $(220)_\gamma$ peak disappeared completely. This is because the STed specimens have homogeneous alloying compositions and martensite microstructure. In addition, the aging temperatures are lower than the austenite start temperature (650 °C). However, if the aging time is prolonged (>10 h), martensite decomposition to austenite may occur. This phenomenon has been reported in wrought maraging steel [5, 13-16], where excess heat treatment was performed.

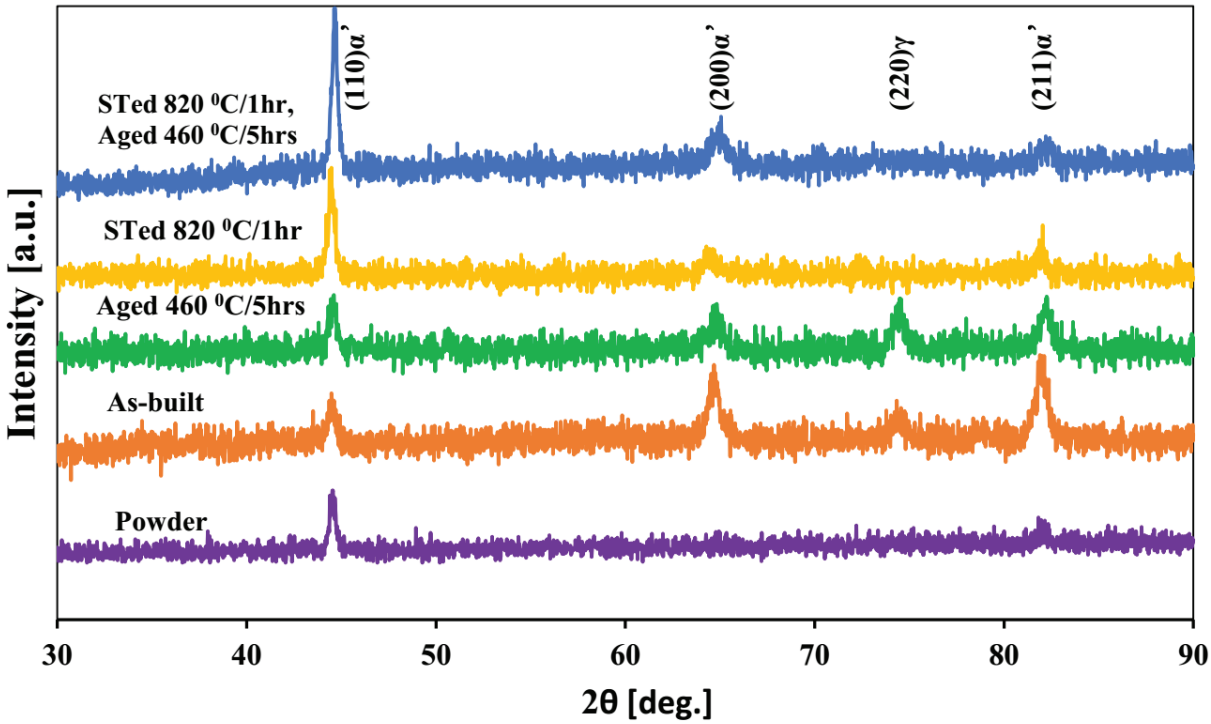

Fig. 4.2 XRD patterns of maraging steel powder and the specimens as-built and treated under different conditions.

Moreover, it seems that no evident change in the intensity of α' phase with (110) and (200) orientations occurs, but the intensity of (211) peak has been reduced after ST at 820 °C for 1 h and aging at 460 °C for 5 h. Note that no peaks from intermetallic compounds, such as Ni_3Mo, Ni_3Ti and Fe_2Mo, have been detected in aged specimens. This is presumably

associated with extremely small sizes of the intermetallic precipitates. Additionally, high cooling rates during solidification resulted in formation of α' phase and prohibited precipitation of the intermetallic compounds. Instead, the alloy elements such as Ni, Co, Mo, etc, remained in a supersaturated solid solution [17].

Solution treatment and aging of the as-built specimen (depicted in Fig. 3.7(a)-(d)) resulted in complete disappearance of scan tracks and solidification traces. The cellular structure was replaced by massive unstable martensite microstructure characterized by fine bundles of parallel, heavily dislocated laths as shown in Fig. 4.3(a) and (b).

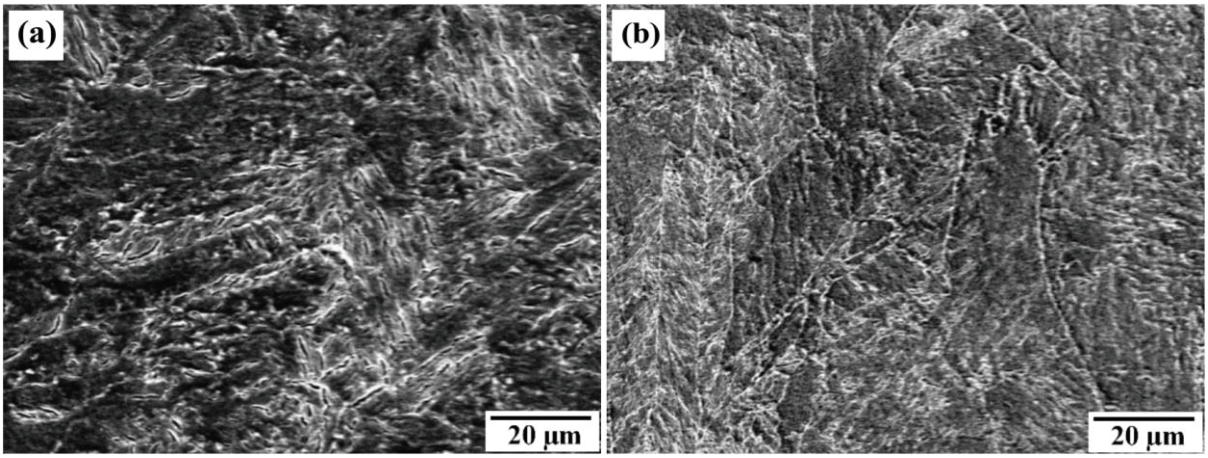

Fig. 4.3 (a) Horizontal and (b) vertical cross-sectional SEM images of the specimen solution-treated at 820 °C for 1 h and aged at 460 °C for 5 h.

Fig. 4.4 shows the EBSD data on horizontal cross sections of as-built, aged, and STAed specimens. From the phase maps shown in Fig. 4.4(a)-(c), the as-built specimen was not fully martensitic and trace amount of γ phase remained. After aging at 460 °C for 5 h, the quantity of γ phase increased (Fig. 4.4(b)). Solution treatment at 820 °C for 1 h and aging at 460 °C for 5 h led to substantial reduction of the γ phase (Fig. 4.4(c)). At the same time, it appears that trace amount of Ni_3Ti particles precipitated in the matrix during the aging. These findings are in good agreement with the XRD results shown in Fig. 4.2. However, it should

be noted that it is difficult to detect all precipitates because of their extremely small sizes. The quantity of precipitates is trivial as portrayed in Fig. 4.4(c) since the EBSD analysis used in this research could be performed for only Ni_3Ti precipitates. The other possible precipitates including Ni_3Mo and Fe_2Mo were included in the martensite matrix.

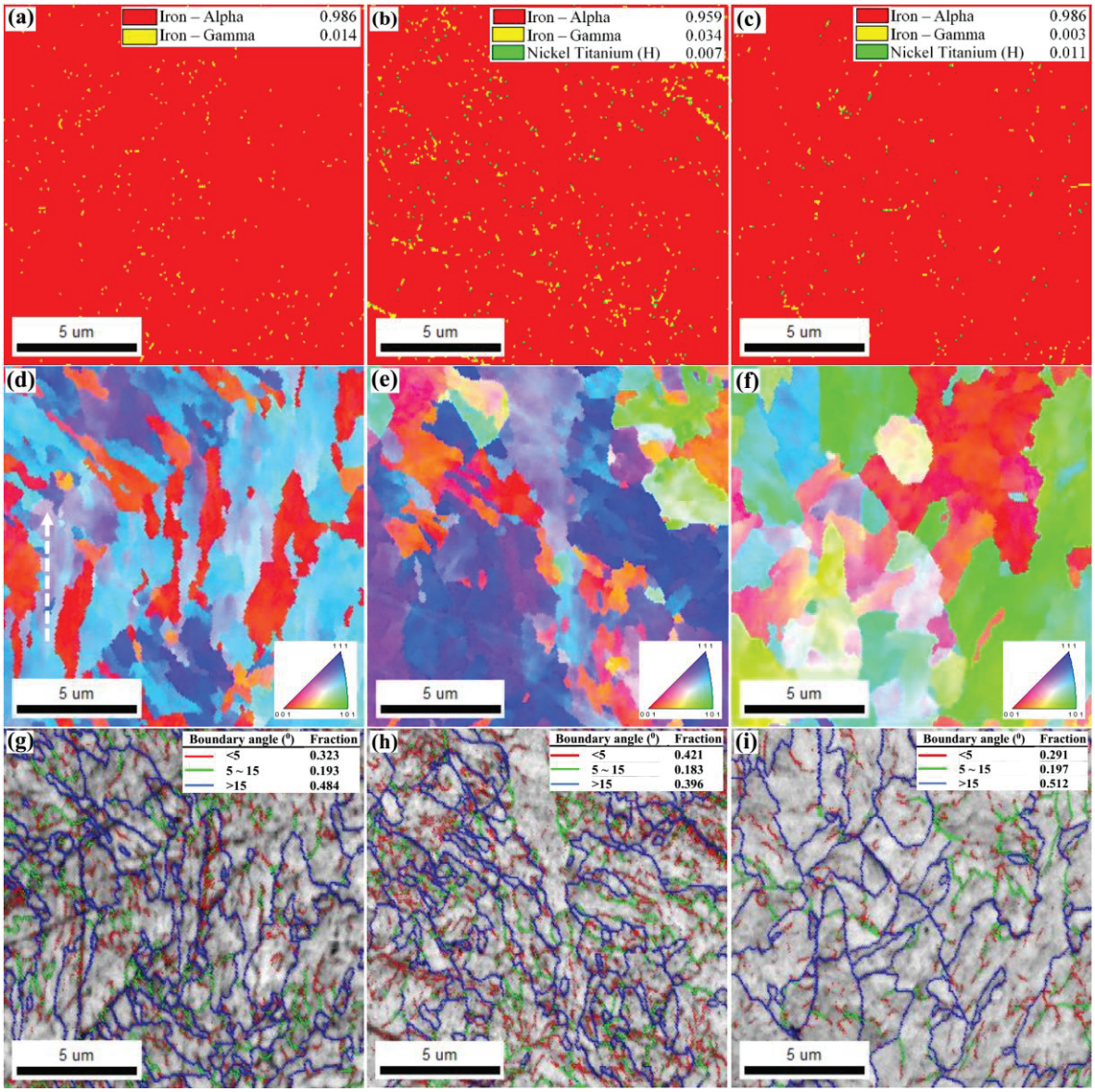

Fig. 4.4 EBSD data on horizontal cross sections of (a), (d), and (g) as-built, (b), (e), and (h) aged (460 °C for 5 h), and (c), (f), and (i) STAed (STed at 820 °C for 1 h and aged at 460 °C for 5 h) specimens. (a)-(c) phase maps, (d)-(f) IPF maps, and (g)-(i) grain boundary maps. Bright dotted arrow shows the laser scanning direction.

The IPF maps in Fig. 4.4(d)-(f) show the grain size, shape and orientation in as-built, aged, and STAed specimens. The average grain sizes for the as-built, aged, and STAed specimens were 0.982 ± 0.961 μm, 0.951 ± 0.905 μm, and 1.272 ± 1.238 μm, respectively. The as-built and aged specimens exhibited almost the same average grain size, while the STAed specimen had a larger grain size due to grain growth during solution treatment at a high temperature. On the other hand, it seems that some grains in the as-built specimen were oriented along the laser scanning direction (Fig. 4.4(d)), this might be the result of solidification of the melt pool because the temperature gradient reaches the maximum at the leading edge of the laser beam. However, this elongated grain morphology became weak after aging. As shown in Fig. 4.4(f), the solution treatment and aging resulted in a significant change in grain orientation. This change in orientation is believed to be attributed to the solution treatment during STA process. A high heating temperature and long soaking time during the solution treatment lead to all alloying elements being dissolved into the matrix to form a supersaturated solid solution (austenite phase). Moreover, the cooling rate is quite slow during the solution treatment process. These certainly result in a different grain orientation from both as-built and aged specimens (Fig. 4.3(d) and (e)).

The grain boundary maps shown in Fig. 4.4(g)-(i) indicated that the as-built specimen had higher fraction (51.6%) of small angle grain boundaries (SAGBs) with misorientation angles of <15°. This may be due to its fine grain microstructure resulting from rapid epitaxial solidification during SLM process. Furthermore, the aged specimen had the highest fraction (60.4%) of SAGBs, presumably due to formation of extremely small precipitates which impede movement of dislocations [18, 19]. On the other hand, the STAed specimen contained a large fraction (>51%) of high angle grain boundaries (HAGBs) due to slow cooling after solution treatment. These results are in good agreement with the IPF findings.

4.3.2 Effects of solution treatment and aging on mechanical properties

Maraging steels are age-hardenable through aging in a temperature range of 400-650 °C [12, 17]. Aging at temperatures below 450 °C produces ordered and coherent precipitated phases, while rapid and intense aging takes place at temperatures between 450 and 600 °C [15, 16]. Fig. 4.5 illustrates the variations of Vickers hardness as a function of energy density.

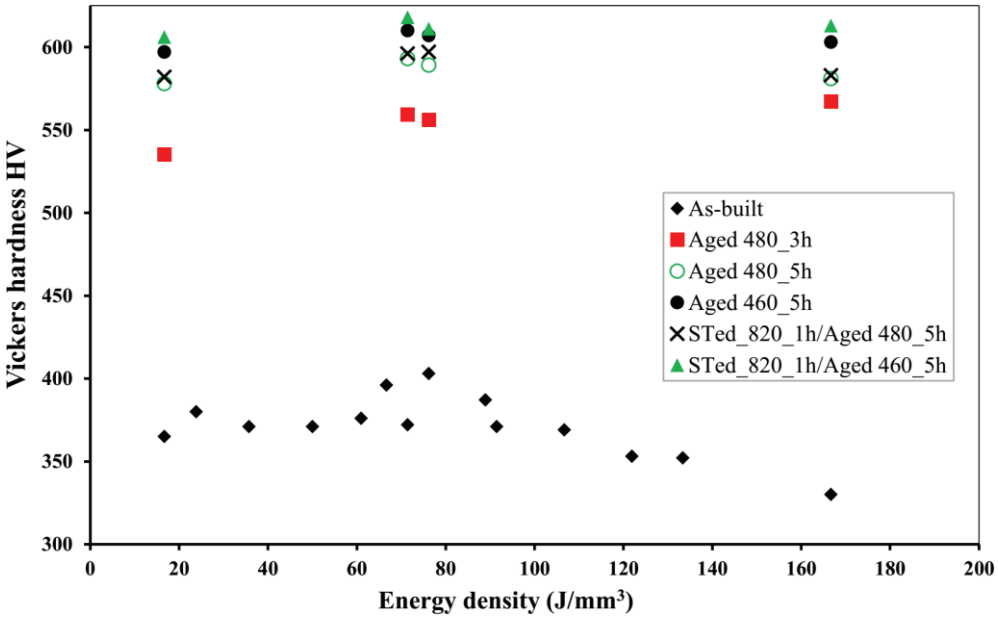

Fig. 4.5 Variations of Vickers hardness of as-built, aged and STAed specimens as a function of energy density.

Compared to conventional maraging steel products, which have a hardness value of 280 HV in martensite state [13], all the as-built specimens showed higher hardness values (330-403 HV) although the hardness depends on the energy density delivered. The higher hardness values of the as-built specimens are attributed to fine columnar and/or dendritic microstructure obtained during rapid cooling in the SLM process, see Fig. 3.7(c) and (d). When the as-built specimens were subjected to aging treatment at different temperatures or times, the hardness tremendously increased due to the formation of fine precipitates of

intermetallic compounds such as Ni_3Ti in the martensite matrix as mentioned above. For example, when the as-built specimen prepared using an optimum energy density of 71.43 J/mm^3 was aged at 480 °C and 460 °C for 5 h, the hardness values increased to 593 HV and 610 HV, respectively. These values are close to or slightly higher than 594 HV of conventional age-hardened maraging steel [1]. Nevertheless, from the XRD and EBSD results shown in Figs. 4.2 and 4.4, some retained γ phase existed in as-built and aged specimen, which results in reduction of hardness. Therefore, to further improve the hardness value, solution treatment seems to be necessary prior to aging. As shown in Fig. 4.5, after solution treatment at 820 °C for 1 h, the aging treatment at 480 °C and 460 °C for 5 h led to higher hardness values compared to the aged samples without solution treatment.

Fig. 4.6 shows the dependence of Vickers hardness on aging temperature and time for the samples which were built at the optimum energy density and solution-treated at 820 °C for 1 h, followed by aging at different temperatures and times. The initial aging caused a rapid increase in hardness at all the aging temperatures. The aging treatment at 460 °C exhibited a high hardness level and the maximum hardness value attained was 618 HV after aging at 460 °C for 5 h. Prolonging the aging time to 24 h caused a gradual decline in hardness.

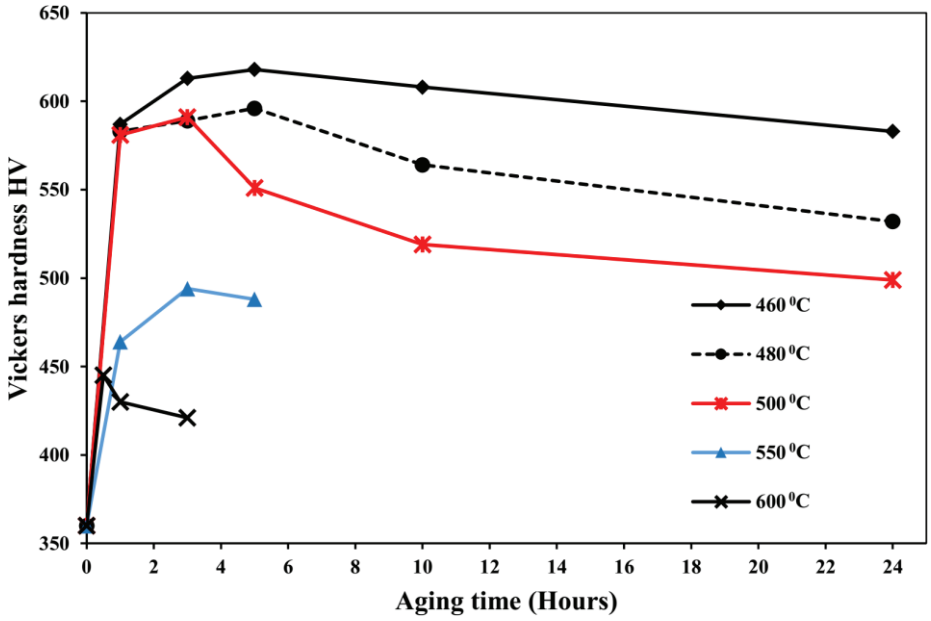

Fig. 4.6 Dependence of Vickers hardness on aging temperature and time for the specimens built at optimum energy density and solution-treated at 820 °C for 1 h.

Moreover, the aging at temperatures above 550 °C showed much lower hardness values. The main reason for hardness reduction at longer times and higher temperatures is believed to be due to particle coarsening of the precipitating phases, *i.e.*, overaging [13]. Another reason may be the precipitation of Fe_2Mo and partial dissolution of the $Ni_3(Ti,Mo)$ intermetallic compound giving rise to formation of and Ni-rich γ phase [15-17].

Fig. 4.7 shows the stress-strain curves obtained from tensile tests in different loading directions for the as-built and STAed specimens. The as-built specimens exhibited good ductility (10.38 %), low tensile strength (1125 MPa), and low values of Young's modulus (163 GPa). However, solution treatment and aging led to significant increase in tensile strength, slight rise in Young's modulus (185 GPa), and a drastic reduction in ductility (5.27 %). The maximum tensile strength obtained was 2033 MPa after STA. This significant enhancement in strength is due to precipitation of fine intermetallic compounds in the martensite matrix during the aging process. Moreover, the increase in Young's modulus in the solution treated/aged specimens is also associated with the formation of large amount of

fine-sized intermetallic precipitates during the STA process. This is because various intermetallic compounds distributed in the STAed specimens have much higher Young's modulus than the martensite matrix.

With regard to the influence of building direction on mechanical properties, as shown in Fig. 4.7, the vertical specimens with the building direction parallel to the loading direction had slightly lower tensile strength and much lower elongation than the horizontal specimens with the building direction perpendicular to the loading direction. This is because, in the horizontal specimens, failure occurs due to layer shearing at significantly high elongation offering more load bearing capabilities unlike in the vertical specimens, where failure is due to layer separation at minimal elongation.

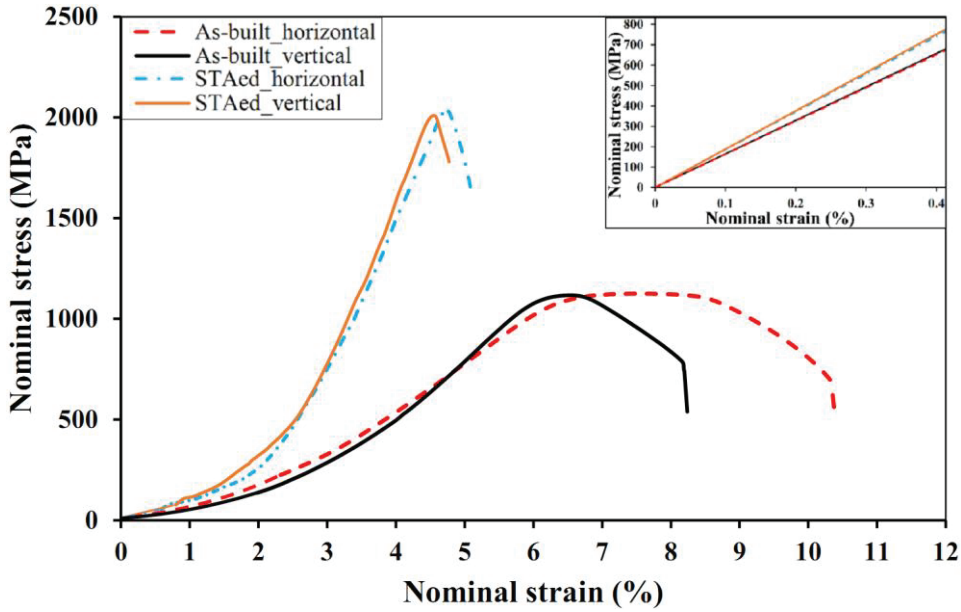

Fig. 4.7 Nominal stress - strain curves for as-built with optimum process parameters and STAed (STed at 820 °C for 1 h and aged at 460 °C for 5 h) specimens. The tensile tests were performed with loading directions perpendicular (horizontal) and parallel (vertical) to the building direction. The inserted figure shows the stress-strain curves in elastic deformation regions obtained by using strain gages.

Fig. 4.8 shows fracture surfaces of the tensile specimens in as-built and STAed conditions. It is evident that the fracture surface of the as-built specimen consisted mainly of fine dimples as shown in Fig. 4.8(a). This depicts an entirely transgranular rupture mode referred to as micro void coalescence [20]. On the other hand, the rupture in the STAed specimen showed brittle appearance characterized by quasi-cleavages (Fig. 4.8(b)). In addition, specimens processed at low and high energy density exhibited brittle fracture due to fusion inefficiencies while those processed at the optimum energy density of 71.43 J/mm^3 had a ductile fracture.

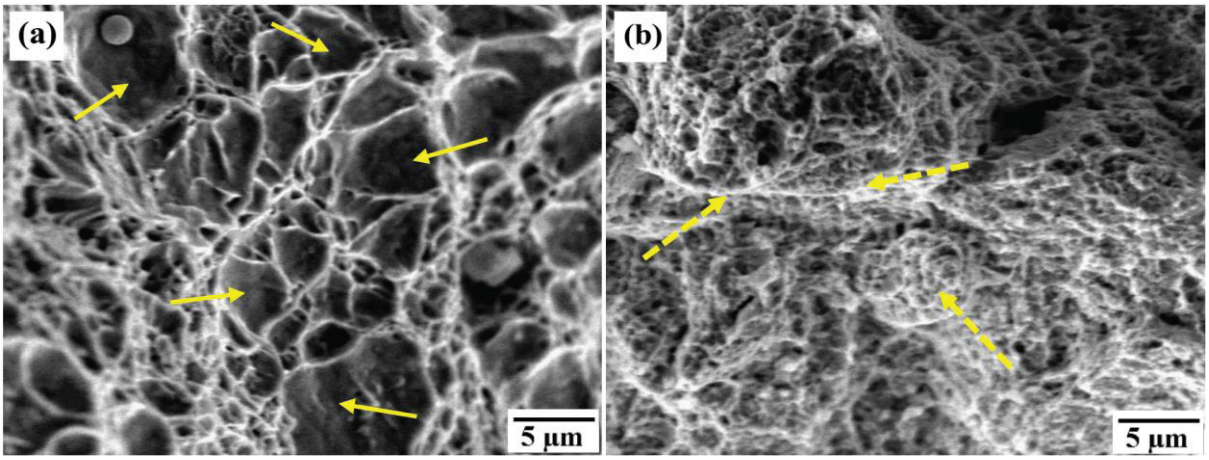

Fig. 4.8 SEM images showing fracture surfaces of (a) as-built and (b) STAed specimens. Solid arrows indicate dimples while dotted arrows show fracture cleaves.

Charpy impact test was also carried out on the SLMed specimens in as-built and STAed conditions. As shown in Fig. 4.9, the impact energy is much higher (94 J) in the optimized specimen in the as-built state than in the specimens processed at minimum (16.67 J/mm^3) and maximum (166.67 J/mm^3) energy density, 13 J and 45 J, respectively. Evidently, STA leads to a significant decrease in the impact energy (Fig. 4.9), and a transition from ductile to brittle rupture in the optimized specimen, see Fig. 4.10. The decrease in impact energy and

occurrence of brittle fracture in the STAed specimens is due to the precipitation of fine intermetallic compounds which limit their ductile deformation.

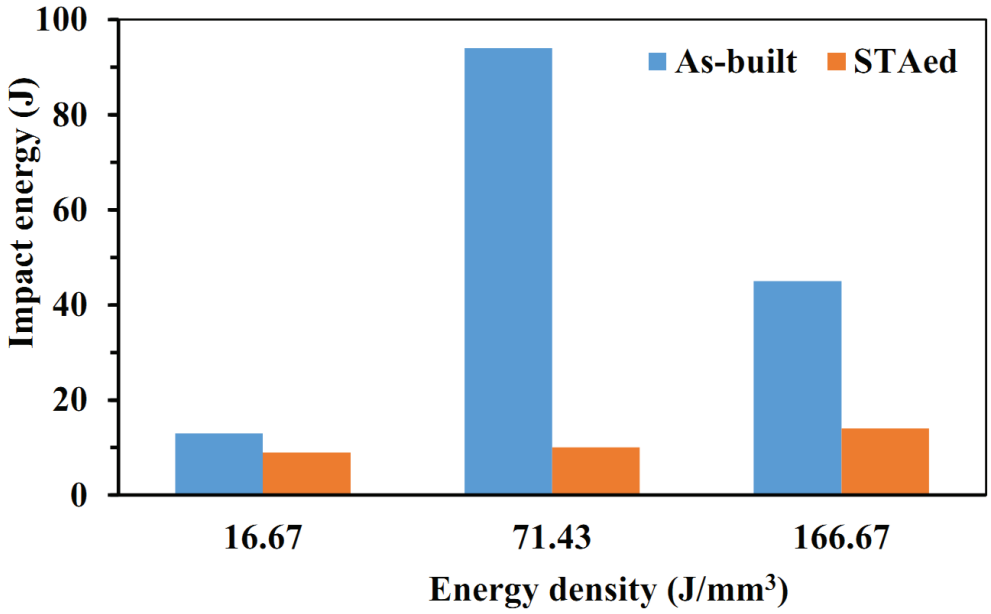

Fig. 4.9 Charpy impact energy of the as-built and STAed specimens processed at minimum (16.67 J/mm^3) optimum (71.43 J/mm^3), and maximum (166.67 J/mm^3) energy density.

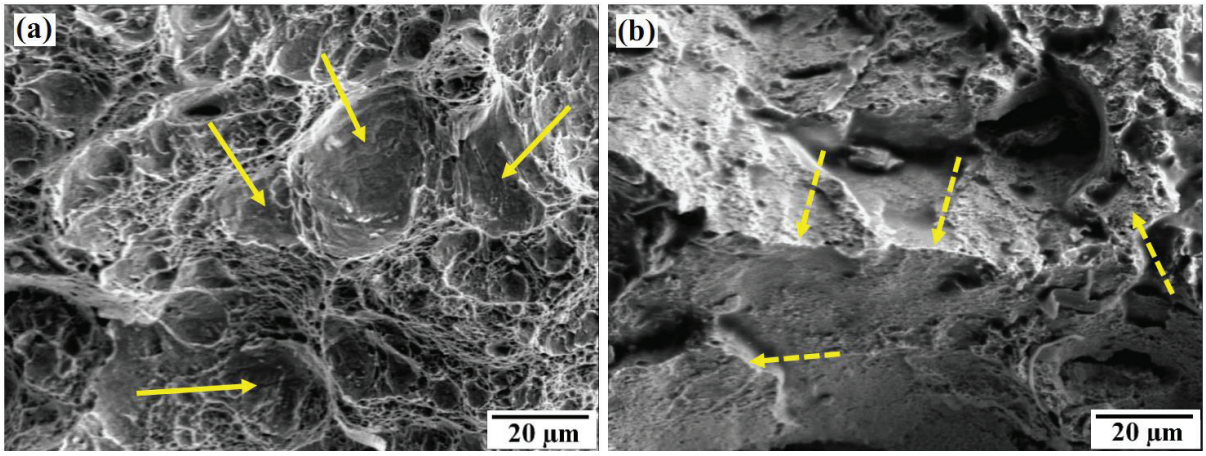

Fig. 4.10 SEM images showing Charpy impact test fracture surfaces of (a) as-built and (b) STAed specimens. Solid arrows indicate dimples while dotted arrows show quasi-cleavages.

4.4 Conclusions

In this chapter, the effect of solution treatment and aging heat treatment on the microstructure and mechanical properties of SLMed maraging steels has been investigated. It has been found that, the as-built specimens consisted of predominantly martensite with trace amount of austenite phase. During aging, the quantity of austenite phase increased due to reversion of martensite to austenite. To optimize the microstructure and mechanical properties, it is necessary to perform solution treatment prior to aging for SLMed products. It has been found that the solution treatment caused almost complete disappearance of austenite phase in subsequently aged specimens. Furthermore, the microstructure of as-built specimens was characterized by fine columnar and/or dendritic grains with a submicron order due to rapid solidification of melt pool. Solution treatment and aging resulted in grain growth of the martensite matrix and a significant change in grain orientation.

With regard to the mechanical properties, the SLMed products exhibited higher strength and hardness than conventionally fabricated ones in their martensite state. The maximum hardness value obtained in this research was 618 HV after solution treatment at 820 °C for 1 h and aging at 460 °C for 5 h. As-built specimens exhibited ductile fracture while aging and STA prompted brittle fracture on the SLMed specimens. When as-built specimen was subjected to solution treatment and aging, the maximum tensile strength obtained was 2033 MPa, while the tensile ductility significantly decreased from 10.38 % to 5.27 %. Moreover, the SLMed specimens with the building direction parallel to the loading direction had slightly lower tensile strength and much lower elongation than those with the building direction perpendicular to the loading direction. The as-built specimen in optimized conditions had higher impact energy of 94 J compared to 13 J and 45 J of specimens processed at minimum and maximum energy density, respectively. In addition, it exhibited ductile rupture

characterized by dimples while STA led to a significant decrease in impact energy and occurrence of brittle rupture in all the specimens irrespective of the processing conditions.

References

[1] Casati, R., Lemke, J.N., Tuissi, A. and Vedani, M., 2016. Aging Behaviour and Mechanical Performance of 18-Ni 300 Steel Processed by Selective Laser Melting. *Metals*, *6*(9), p.218.

[2] Kempen, K., Thijs, L., Van Humbeeck, J. and Kruth, J.P., 2012. Mechanical properties of AlSi10Mg produced by selective laser melting. *Physics Procedia*, *39*, pp.439-446.

[3] Ooi, S.W., Hill, P., Rawson, M. and Bhadeshia, H.K.D.H., 2013. Effect of retained austenite and high temperature Laves phase on the work hardening of an experimental maraging steel. *Materials Science and Engineering: A*, *564*, pp.485-492.

[4] Reis, A.G., Reis, D.A.P., Abdalla, A.J., Otubo, J. and Sandim, H.R.Z., 2015. A dilatometric study of the continuous heating transformations in maraging 300 steel. In *IOP Conference Series: Materials Science and Engineering* (Vol. 97, No. 1, p. 012006). IOP Publishing.

[5] Belyakov, L.N., Nikol'skaya, V.L. and Ryzhak, S.S., 1968. The α→ γ transformation in maraging steel N18K9M5T. *Metal Science and Heat Treatment*, *10*(6), pp.438-442.

[6] Jägle, E.A., Choi, P.P., Van Humbeeck, J. and Raabe, D., 2014. Precipitation and austenite reversion behavior of a maraging steel produced by selective laser melting. *Journal of Materials Research*, *29*(17), pp.2072-2079.

[7] Yadroitsev, I., Bertrand, P., Antonenkova, G., Grigoriev, S. and Smurov, I., 2013. Use of track/layer morphology to develop functional parts by selective laser melting. *Journal of Laser Applications*, *25*(5), p.052003.

[8] Herzog, D., Seyda, V., Wycisk, E., and Emmelmann, C., 2016. Additive manufacturing of metals. *Acta Materialia*, *117*, pp.371-392.

[9] Viswanathan, U.K., Dey, G.K. and Asundi, M.K., 1993. Precipitation hardening in 350 grade maraging steel. *Metallurgical Transactions A*, *24*(11), pp.2429-2442.

[10] Liu, K., Shan, Y., Yang, Z., Liang, J., Lu, L., and Yang, K., 2007. Effect of aging on microstructure and mechanical property of 1900 MPa grade maraging stainless steel. *Journal of Material Science and Technology, 23* (3)*,* pp.312-318.

[11] Tan, C., Zhou, K., Tong, X., Huang, Y., Li, J., Ma, W., Li, F. and Kuang, T., 2016. Microstructure and Mechanical Properties of 18Ni-300 Maraging Steel Fabricated by Selective Laser Melting.

[12] Casalino, G., Campanelli, S.L., Contuzzi, N. and Ludovico, A.D., 2015. Experimental investigation and statistical optimisation of the selective laser melting process of a maraging steel. *Optics Laser Technology*, *65*, pp.151-158.

[13] Kempen, K., Yasa, E., Thijs, L., Kruth, J.P. and Van Humbeeck, J., 2011. Microstructure and mechanical properties of Selective Laser Melted 18Ni-300 steel. *Physics Procedia*, *12*, pp.255-263.

[14] Campanelli, S.L., Contuzzi, N., Angelastro, A. and Ludovico, A.D., 2010. Capabilities and performances of the selective laser melting process. In *New Trends in Technologies: Devices, Computer, Communication and Industrial Systems*. InTech.

[15] Viswanathan, U.K., Dey, G.K. and Asundi, M.K., 1993. Precipitation hardening in 350 grade maraging steel. *Metallurgical Transactions A*, *24*(11), pp.2429-2442.

[16] Pardal, J.M., Tavares, S.S.M., Fonseca, M.C., da Silva, M.R., Neto, J.M. and Abreu, H.F.G., 2007. Influence of temperature and aging time on hardness and magnetic properties of the maraging steel grade 300. *Journal of materials science*, *42*(7), pp.2276-2281.

[17] Davis, J.R., Metals Handbook: Structure/Property Relationships in Irons and Steels, 2nd edition. pp.153-173, 1998 *ASM International.*//http:www.asminternational.org.

[18] Shi, J. and Zikry, M.A., 2009. Grain–boundary interactions and orientation effects on crack behavior in polycrystalline aggregates. *International Journal of Solids and Structures*, *46*(21), pp.3914-3925.

[19] Read, W.T. and Shockley, W., 1950. Dislocation models of crystal grain boundaries. *Physical review*, *78*(3), p.275.

[20] Liu, K., Shan, Y., Yang, Z., Liang, J., Lu, L., and Yang, K., 2007. Effect of aging on microstructure and mechanical property of 1900 MPa grade maraging stainless steel. *Journal of Material Science and Technology, 23* (3), pp.312-318.

Chapter 5 Optimization of Selective Laser Melting Parameters and their Influences on Microstructure and Hardness of SUS316L Stainless Steel

5.1 Introduction

As described in Chapter 3, SLMed parts should possess mechanical properties superior to or comparable with those produced by conventional processes. Such mechanical properties often depend not only on the materials but also on the process parameters adopted. Improper combination of process parameters results in less dense and porous products which do not meet design specifications. Unlike conventional manufacturing techniques where the properties of finished parts are predictable, selective laser melted (SLMed) products are characterized by fluctuating properties which depend partly on process parameters, cold working, and post annealing conditions [1]. SLMed parts possess high compactness close to 100% and mechanical property near to wrought piece. This has significantly contributed to the paradigm shift of AM technologies from rapid prototyping to generation of end-use parts and the needs of personalized customization for example in implant tooth, artificial bone, and medical guide [2]. With SLM, functional parts can be produced using low cost powders such as brass, copper, Ti alloys, and stainless steels [3].

SUS316L stainless steel is in the category of austenitic stainless steels that cannot be strengthened by heat treatment. They are essentially non-magnetic in the annealed state and can be hardened by cold working. Their excellent cryogenic properties coupled with good high-temperature strength, oxidation and corrosion resistance makes them valuable in a diversified range of uses, including nuclear reactor vessels, heat exchangers, components for chemical processing and pulp and paper industries, domestic appliances, and household utensils [4]. However, conventional manufacture of SUS316L parts is time consuming, costly, and limited in terms of complexity and customization. Consequently, SLM has been adopted

in the production of stainless steel bone scaffold, titanium alloy tooth, aircraft engine parts, among other components with a view to exploit the merits of flexible/ intricate geometry, short cycle times, reduced cost and tooling associated with the process [2, 5, 6]. Recent studies on SLM of SUS316L stainless steel have focussed on the relationship between process parameters and mechanical properties [6-8]. However, optimization of the process parameters, their effects on the microstructure and corrosion behavior is still not well studied yet [8, 9].

In this chapter, the process parameters including laser power, scan speed, pitch, and spot diameter were varied and their effects on relative density, surface quality, microstructure, and hardness of SLMed SUS316L stainless steel were investigated. The purpose was to optimise the process parameters so as to obtain high-quality SLMed products and contribute new knowledge towards SLMed stainless steel parts.

5.2 Experimental procedure

5.2.1 Sample preparation

Nitrogen gas-atomized SUS316L stainless steel powder (Matsuura stainless 316L) with an average particle size of 21 μm as shown in Fig. 5.1 was used as the starting material. The chemical composition of the alloy is shown in Table 5.1.

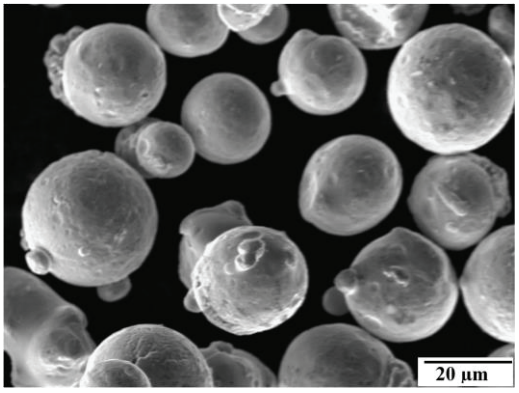

Fig.5.1 SEM image of SUS316L stainless steel powder.

Table 5.1 Chemical composition of SUS316L stainless steel powder used in the experiment.

Alloying element	Cr	Ni	Mo	Si	Mn	P	C	S	Fe
wt %	17.50	12.53	2.10	0.91	0.80	0.024	0.017	0.011	Balance

Matsuura LUMEX Avance-25 hybrid machine (Matsuura Machinery Corporation, Japan) equipped with Yb fiber laser was used to prepare test specimens measuring 10 mm × 10 mm × 3 mm for microstructural examinations. The design of experiment (DOE) approach was adopted in the optimization of the process parameters. Using different sets of laser power (*P*: 100 - 400 W), scan speed (*v*: 400 - 1000 mm/sec), pitch (*h*: 0.025 - 0.2 mm) and spot diameter (*d*: 0.05 - 0.3 mm), the powders were selectively melted layer after layer until the final 3D specimens were completed. The layer thickness (*t*) was maintained at 0.05 mm. The as-built specimens were removed from the steel base plate by wire EDM cutting.

5.2.2 Characterization

A non-contact laser reflectance VHX-5000 digital microscope (Keyence, Japan) was used to evaluate the surface roughness (Ra) of the as-built specimens. An average of six Ra measurements was taken after filtering to eliminate background noise at each processing condition. The relative density of the specimens was determined using the Archimedes method and the results were presented as the arithmetic means of three different measurements at each processing condition. V2A etchant (100 ml hydrochloric acid, 100 ml water, 10 ml nitric acid) was used to etch polished specimens at room temperature for 5-7 min. The microstructure was observed using optical microscope (OM) and scanning electron microscope (SEM). The micro-hardness (HV) values of the as-built and aged specimens were measured using HMV-2000 micro-Vickers tester (Shimadzu Corporation, Japan) at 19.61 N

and the results presented as the arithmetic means of twelve measurements at each processing condition.

5.3 Results and discussion

5.3.1 Effects of process parameters on relative density and surface quality

As shown in Fig. 5.2(a), when the scanning speed was increased from 400 to 700 mm/sec, the relative density increased from 97.9 to 99.2%. Above 700 mm/sec, the relative density decreased to 98.8% at the maximum scanning speed of 1000 mm/sec. At a laser power of 100 W, the relative density of the specimen was 98.6%, and as the laser power increased, the relative density increased to 99.2% at 320 W, see Fig. 5.2(b). Beyond 300 W, the relative density decreased to 99.2% at the maximum laser power of 400 W. From Fig. 5.2(c), small and large values of the pitch had significant impact on the relative density of the specimen. Indeed, setting the pitch at 0.05 mm resulted in a low relative density of 98.5% while increasing the pitch to 0.12 mm, the relative density gradually increased to 99.2%. Any further increase in the pitch led to a drastic reduction in the relative density. Critically low value of relative density was obtained when the pitch was increased to 0.02 mm, a value equal to the spot diameter.

The relative density remained fairly constant for small values of spot diameter (i.e., less than 0.1 mm). However, beyond 0.1 mm, the value of relative density increased to 99.2% when the spot diameter was 0.2 mm. Further increase in spot diameter led to a decrease in relative density as shown in Fig. 5.2(d). To evaluate the influence of derived parameters on relative density of the as-built specimen, overlap rate which relates spot diameter and pitch as expressed in Eq. (1) in Section 3.3.1 was considered. The results depicted in Fig. 5.2 (e) indicates that, at 0% overlap rate, critically low value of relative density (93.3%) was

obtained. When the overlap rate was increased to 20%, the relative density rapidly increased to 99.0%. It is evident that, the relative density remained fairly constant for overlap rates between 20 and 62.5% with peak value of 99.2% at an overlap rate of 40%. Further increase in overlap rate led to a gradual drop in the values of relative density.

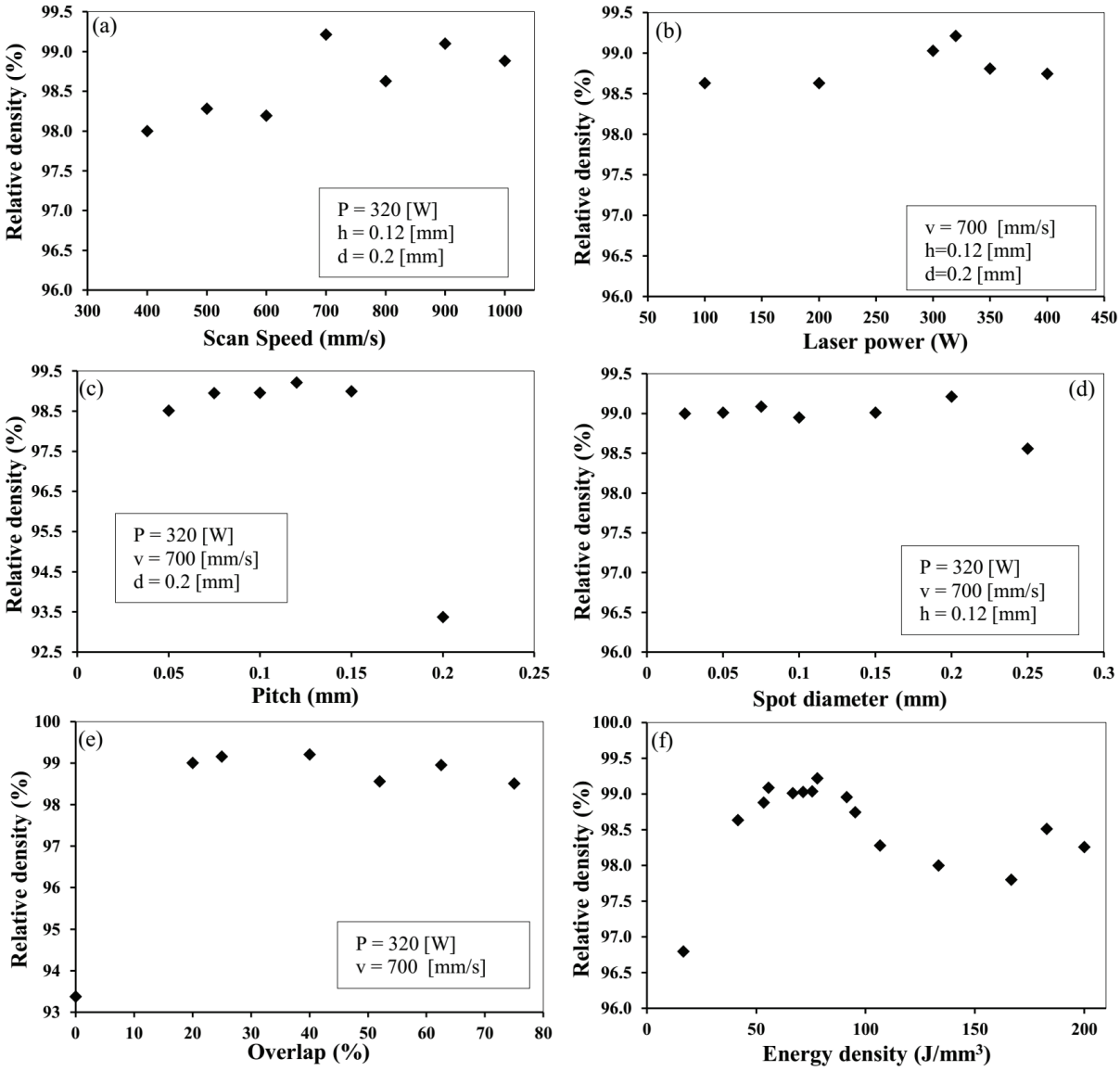

Fig. 5.2 Effects of process parameters on relative density of as-built SLMed specimens.

Energy density (E) is an important parameter in SLM. It relates to laser power (P), scan speed (v), pitch (h), and layer thickness (t) and can be calculated using Eq. (2) in Section 3.3.1. The amount of laser energy delivered should be large enough for the powders to

completely melt, undergo epitaxial solidification, and form fully dense parts. As shown in Fig. 5.2(f), higher energy density resulted in higher relative density. However, excessively high energy density caused reduction of relative density of the SLMed specimens. The maximum relative density attained was 99.2% at an energy density of 77.92 J/mm^3, which corresponds to scan speed of 700 mm/sec and laser power of 320 W. Processing the specimens at very low energy density (16.67 J/mm^3) and exceedingly high energy density (200.98 J/mm^3) resulted in low values of relative density.

Fig. 5.3 shows the optical microscopy (OM) images on the horizontal cross sections of as-built specimens, revealing the shape and distribution of pores with varying energy density. It is evident that, specimens processed at low energy density had large number of irregular-shaped pores while those processed at high energy density had many crevice-like pores elongated along the laser scanning direction. The presence of these pores resulted in lower values of relative density (96.8% and 98.2%) as shown in Fig. 5.3(a) and Fig. 5.3(c) respectively. On the other hand, as-built specimen processed at an energy density of 77.92 J/mm^3 had hardly any pores resulting in maximum relative density of 99.2%, see Fig. 5.3(b). At high energy density, extended crevice-like pores persisted in the as-built specimen, this may be due to the residual thermal internal stresses generated by rapid epitaxial solidification. Moreover, the alloying elements in the steel composition may have different thermal coefficients which upon heating may result in a thermal miss-match that generates stress. These stresses could cause micro-cracks inside the steel microstructure as shown in Fig. 5.3(c).

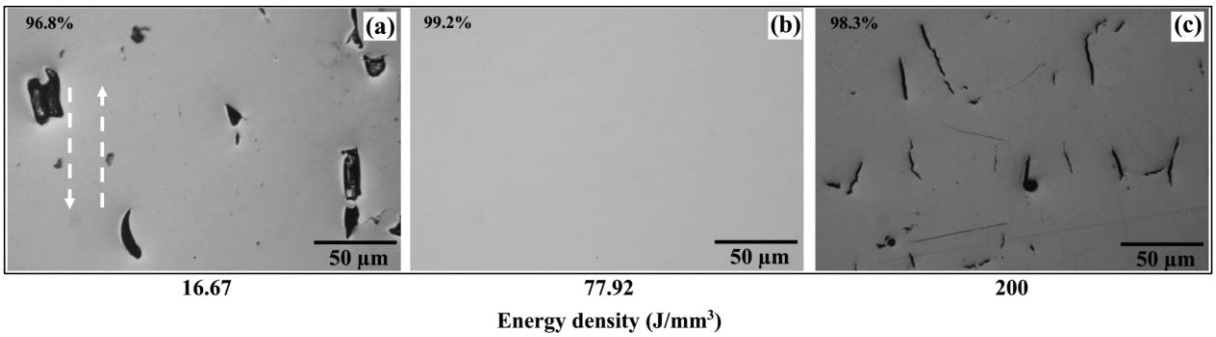

Fig. 5.3 OM images on horizontal cross section of as-built specimens showing the distribution of pores and changes in relative density with variations in energy density. The dotted arrows indicate laser scanning direction.

The surface quality of SLMed SUS316L steel is instrumental in the overall performance of the parts. Poor surface quality may be a source failure (e.g., corrosion start point, crack initiation zone etc.) when the specimens are in use [10]. The SEM images in Fig. 5.4 show the top-surface morphologies of the as-built specimens. Rougher surfaces were observed at the minimum (16.67 J/mm^3) and maximum (200 J/mm^3) values of energy density, as shown in Fig. 5.4(a) and (c), respectively. At lower energy density, insufficient fusion causes the formation of distinct scan tracks with visible gaps and macro pores (as indicated by the arrows in Fig. 5.4(a)) between two neighboring scan tracks. Moreover, macro pores containing some powder particles (marked by a rectangle) can be seen on the surface. These particles are believed to arise from un-melted powder due to lower energy density, which results in low relative density of the as-built specimen. On the other hand, some larger spherical particles (balls) and circumstantial cracks remained on the surface (Fig 5.4(c)) under the conditions of high energy density. Similar particles appear small in both size and number on the as-built specimen processed at optimum condition (Fig. 5.4(b)). The formation of these particles (balling) is extensively discussed in Section 3.3.1.

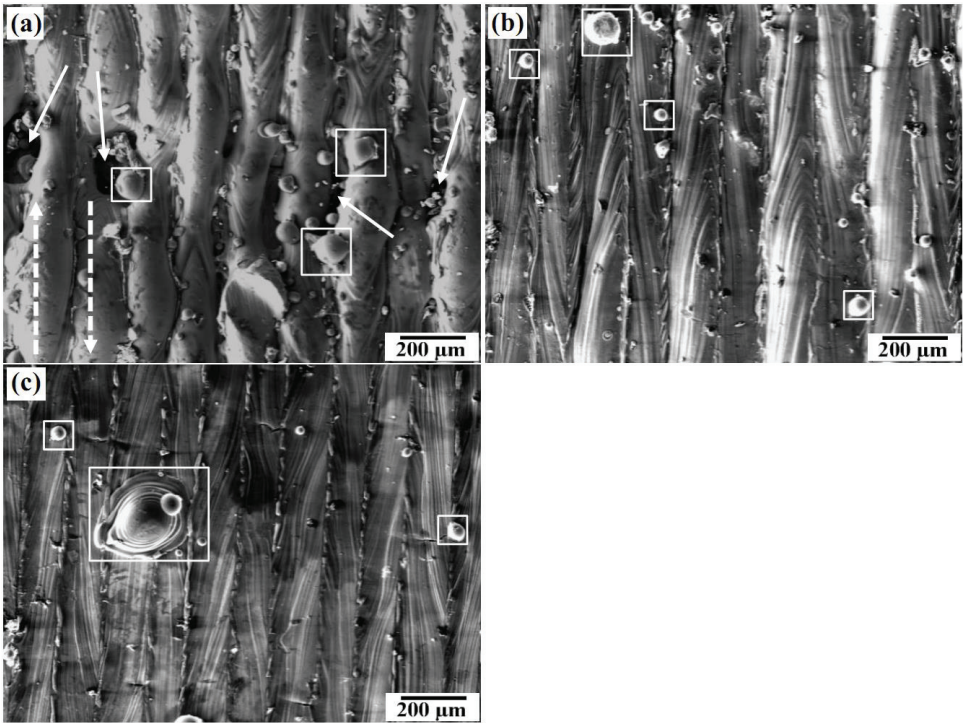

Fig. 5.4 SEM images on top surfaces of as-built specimens processed at (a) minimum (16.67 J/mm^3), (b) optimum (77.92 J/mm^3), and (c) maximum (200 J/mm^3) energy density. The complete arrows indicate gaps and macro pores between scan tracks while the rectangles show resultant surface balling. The dotted arrows indicate laser scanning direction.

As depicted in Fig. 5.4 (c), newly formed large particles with crevices appear on the surface. This could be due to the formation of large melt pool and prolonged cooling time at maximum energy density resulting in spheroidization and cracking. Proper melting was attained at the optimum energy density (77.92 J/mm^3) leading to reduced balling and well spread scan tracks (Fig. 5.4 (b)).

The surface roughness of SLMed SUS316L steel is greatly influenced by the energy density and overlap rate as discerned in Fig. 5.5(a) and (b) respectively. Clearly, low and high values of energy density resulted in poor surface qualities. In this study, relatively smooth surface with a surface roughness of 10.16 µm was obtained for as-built specimens processed at an energy density of 77.92 J/mm^3, see Fig. 5.5 (a). From Fig. 5.5(b), a zero (0%) overlap rate resulted in poor surface, increasing the overlap rate led to a significant improvement in

the surface roughness. Indeed, relatively smooth surface with a roughness value of Ra= 9.95 μm was obtained at 40% overlap. Further increase in overlap rate led to deterioration of the surface quality (Fig. 5.5 (b)). Based on condition of optimal relative density (99.2%) and surface quality (9.95 μm), the optimized process parameters were found to be laser power of 320 W, scan speed of 700 mm/s, energy density of 77.92 J/mm^3, and overlap rate of 40%.

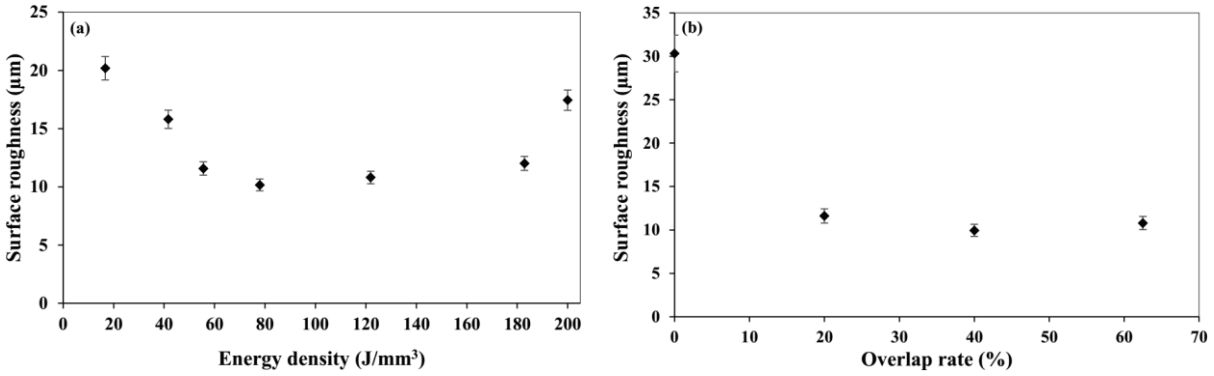

Fig. 5.5 Variations of surface roughness of as-built specimens with (a) energy density and (b) overlap rate.

5.3.2 SLM Processing window of SUS316L stainless steel

From the preliminary results in Section 5.3.1, the interactions among laser power, scan speed, and energy density have been used to successfully develop a process map based on the formability of SUS316L powders for fabricating single layer and multi-layer 3D parts.

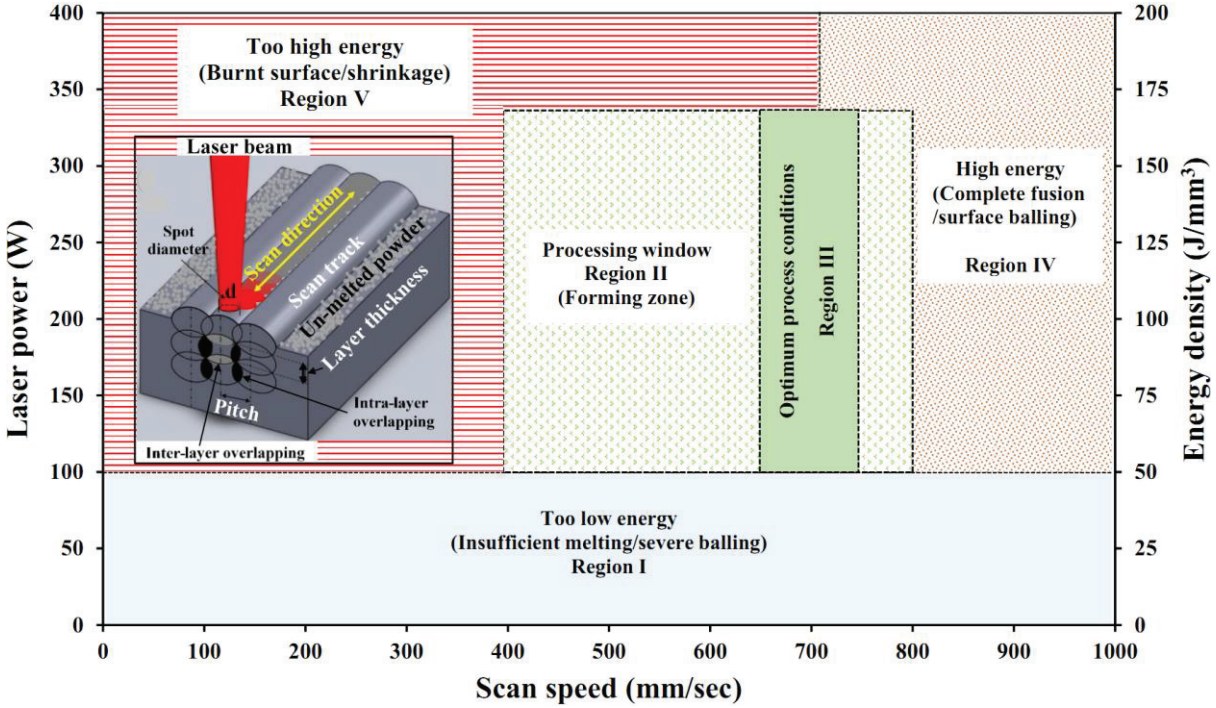

Fig. 5.6 Schematic illustration of SLM process integrated with a process map that relates laser power, scan speed, and energy density.

Clearly, there exists several processing regions which correspond to different relative density values, microstructure, and hence mechanical properties of SLMed SUS316L products. The too low energy zone demarcated in Region I is elicited by the lowest energy density for all the scan speeds used combined with relatively low laser power. As a result, the melting temperature of SUS316L powder (1400 °C) may not be reached which results in partial melting of the powders. The laser energy density is insufficient to generate adequate liquid phase and consequently leads to a poor bond neck between the particulates. Even though there was some fusion between the particles during the SLM process, fragile samples without mechanical strength are obtained and numerous un-melted powder fragments (balling) existed on the surface. Specimens fabricated using the process parameters in this zone have many defects such as balling, delamination, brittle fracture, and high porosity as shown in Fig. 5.4(a). A relatively large processing window is obtained in Region II (forming

zone) where adequate powder fusion occurs. The laser power and scan speed in this region are high enough to cause sound metallurgical bonding of the powders resulting in high quality products with relatively high density, flatter scan tracks, and improved surface finish without obvious macro-defects.

Our experimental results revealed that the relative density values of the samples obtained range from 98 to 99% in this region. It can be deduced that, the good range of energy densities in the forming zone increase the powder bed temperature, while reducing the viscosity of the melt pool such that the melt can be spread properly on the previously processed powder layer, thereby facilitating more efficient densification with solid powdered particles. Within Region II, there is a limited zone, Region III, which provides optimum processing region where the SLM products have high density and good surface quality. The relatively high laser power and scan speed in this region enable proper fusion of the powders, thus leading to high relative density values of more than 99% and well-spread scan tracks with good surface quality. In fact, the as-built specimens with very high relative density (99.2%) and good surface roughness (9.95 μm) (Figs. 5.4(b) and 5.5(b)) were obtained at a laser power of 320 W, scan speed of 700 mm/sec, and energy density of 77.92 J/mm^3 which falls within this region. Regions IV and V represent high energy input zones, where high energy density is delivered causing excessive powder fusion, probable evaporation, and ionization of the powders. This may result in well-spread scan tracks, large melt pools, and large surface balling due to the rapid cooling cycle during SLM process (see Fig. 5.4(c)). At a laser power of larger than 400 W, the energy input is so high that the powder is blown off resulting in no track formation or at times burnt product surfaces.

5.3.3 Effects of process parameters on microstructure and micro-hardness

The horizontal cross-sectional OM image of polished/etched as-built specimen shown in Fig. 5.7(a) revealed clear scan tracks and discontinuous nature of the melting process induced by pulsating laser beam. Distinct pools pertaining different layers are visible on the same track The SEM image in Fig. 5.7(b), taken at high magnification reveal the expected cellular solidification microstructure and evidence of epitaxial growth across different track boundaries. More rich structural features can be found at an even smaller; sub-micron and nano levels. As seen in the SEM image of etched specimen shown in Fig. 5.7(b), inside the smaller micro-grains, intragranular 0.5-1μm-sized sub-grains with a cellular structure exist. These sub-grains are confined by the bigger micro-grains of size 5-10 μm. The sub-grains formed have a cellular/columnar structure which contributes to the excellent strength and hardness in SLMed SUS316L stainless steel parts compared to their conventional counterparts.

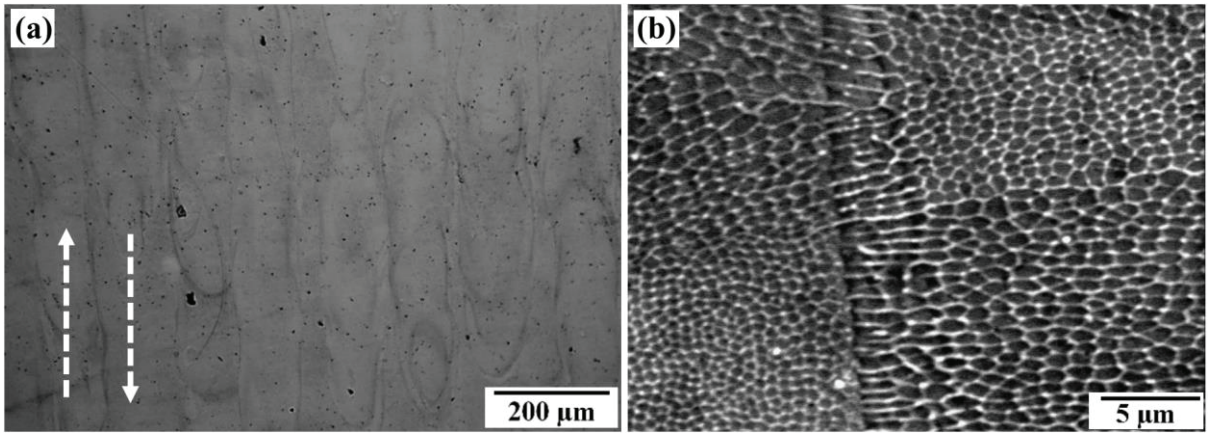

Fig. 5.7 Horizontal cross-sectional (a) OM (b) SEM images of as-built specimen fabricated at optimum process conditions. Bright dotted arrows show the laser scanning direction.

Fig. 5.8 shows the XRD patterns of the SUS316L stainless steel raw powder and the as-built specimen. Clearly, nitrogen gas atomized SUS316L powder consists of entirely austenitic phase with a preferred orientation of $(111)_{\gamma}$. Similarly, SLMed parts had singular

austenitic phase, without any traces of secondary ferrite phase or iron oxide. This is due to the high cooling rate which inhibits any time for diffusion to take place and therefore avoids any transformation or secondary phase formation. However, the crystallographic texture is seen to significantly change to $(220)_{\gamma}$ presumably due to the influences of the scanning strategy and building direction.

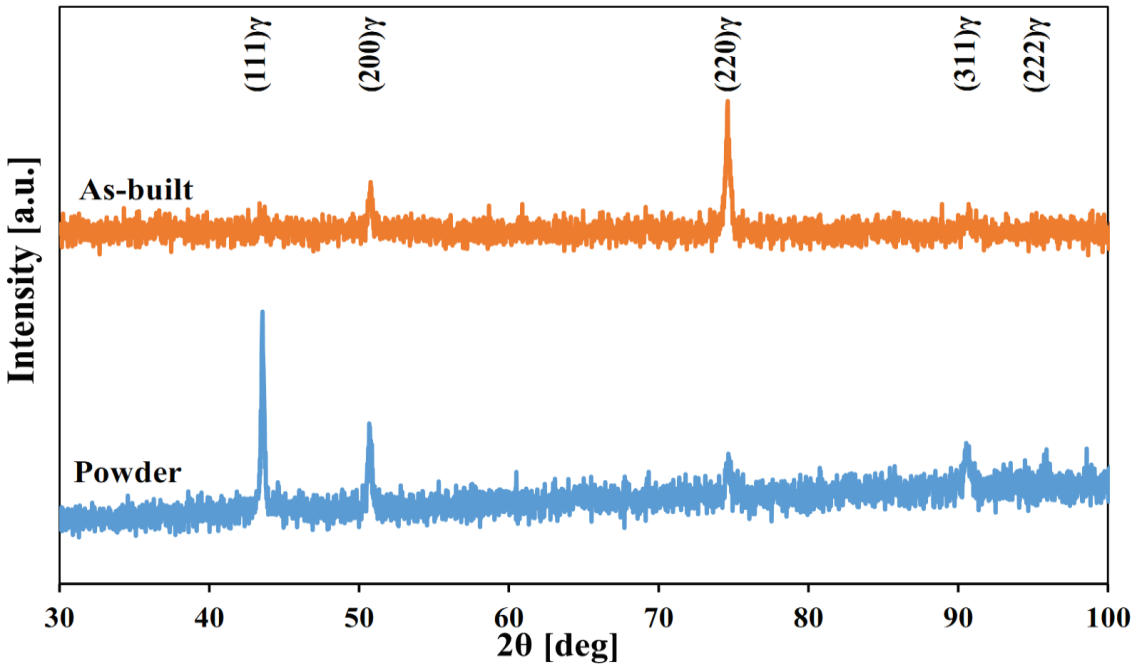

Fig. 5.8 XRD patterns of SUS316L stainless steel powder and the SLMed specimen in as-built condition.

The micro-hardness of the as-built specimen shown in Fig. 5.9 indicates that, SLMed specimen (with maximum relative density) in the as-built state had a micro-hardness of around 241 HV which is slightly higher compared with that of conventionally fabricated SUS316lL specimen (150-200 HV) [11].

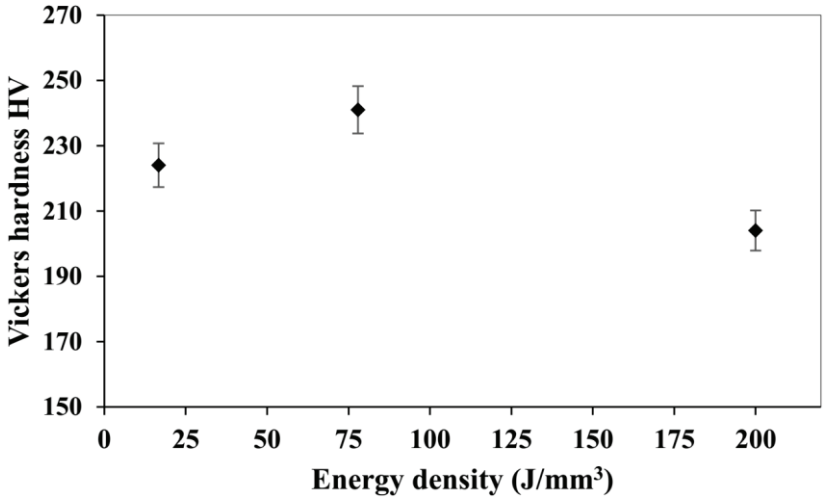

Fig. 5.9 Variations of Vickers hardness of as-built specimen as a function of energy density.

The high micro-hardness can be attributed to the numerous grain boundaries of the small micron-sized intragranular sub-grains which impede and block dislocation motion imposing a hardening effect on the as-built specimen. Hardness of metals and alloys can be directly related to yield strength as both are mechanical properties that are related to resistance of material to deformation.

5.4 Conclusions

The process parameters including laser power, scan speed, pitch, and spot diameter were varied and their effects on relative density, surface quality, microstructure, and hardness of SLMed SUS316L stainless steel have been established. The optimized process parameters that resulted in high-quality SLMed products with relative density of 99.2%, surface roughness of 9.95 μm, micro-hardness of 241 HV were found to be; Laser power of 320 W, scan speed of 700 J/mm^3, and overlap rate of 40%. A formative process map on the SLM of SUS316L stainless steel has been constructed. There exists a relatively large processing window, where sound products with relatively high relative density, flatter scan tracks, and good surface quality can be obtained. For example, the optimum process conditions were found to be scan speed of 700 mm/sec, laser power of 320 W, overlap rate of 40%, and

energy density of 77.92 J/mm^3. These resulted in a maximum relative density of 99.2% and good surface quality with a roughness value of Ra= 9.95 μm.

In addition, as-built specimen consists of sub-micron sized cellular microstructure with intercellular spacing less than 1μm. This contributes to the excellent strength and hardness in SLMed SUS316L stainless steel parts.

References

[1] Tsopanos, S., Mines, R.A.W., McKown, S., Shen, Y., Cantwell, W.J., Brooks, W. and Sutcliffe, C.J., 2010. The influence of processing parameters on the mechanical properties of selectively laser melted stainless steel micro lattice structures. *Journal of Manufacturing Science and Engineering*, *132*(4), p.041011.

[2] Zhang, Y., Liu, F., Chen, J. and Yuan, Y., 2017. Effects of surface quality on corrosion resistance of 316L stainless steel parts manufactured via SLM. *Journal of Laser Applications*, *29*(2), p.022306.

[3] Yasa, E. and Kruth, J.P., 2011. Microstructural investigation of Selective Laser Melting 316L stainless steel parts exposed to laser re-melting. *Procedia Engineering*, *19*, pp.389-395.

[4] Davis, J.R., 1998. Metals handbook; desk edition, pp.362-386.

[5] Hao, L., Dadbakhsh, S., Seaman, O. and Felstead, M., 2009. Selective laser melting of a stainless steel and hydroxyapatite composite for load-bearing implant development. *Journal of Materials Processing Technology*, *209*(17), pp.5793-5801.

[6] Choi, J.P., Shin, G.H., Lee, H.S., Yang, D.Y., Yang, S., Lee, C.W., Brochu, M. and Yu, J.H., 2017. Evaluation of Powder Layer Density for the Selective Laser Melting (SLM) Process. *Materials transactions*, *58*(2), pp.294-297.

[7] Simchi, A. and Pohl, H., 2003. Effects of laser sintering processing parameters on the microstructure and densification of iron powder. *Materials Science and Engineering: A*, *359*(1), pp.119-128.

[8] Song, B., Dong, S., Deng, S., Liao, H. and Coddet, C., 2014. Microstructure and tensile properties of iron parts fabricated by selective laser melting. *Optics & Laser Technology*, *56*, pp.451-460.

[9] Kruth, J.P., Mercelis, P., Van Vaerenbergh, J. and Craeghs, T., 2007, September. Feedback control of selective laser melting. In *Proceedings of the 3rd international conference on advanced research in virtual and rapid prototyping* (pp. 521-527).

[10] Singh, R. and Dahotre, N.B., 2005. Tribology of laser modified surface of stainless steel in physiological solution. *Journal of materials science*, *40*(21), pp.5619-5626.

[11] Outokumpu Stainless, A.B., 2013. Handbook of Stainless Steel. *Espoo: Outokumpu Oyj*.

Chapter 6 Summary

During product development, nothing communicates an idea more than a model. 3D additive manufacturing (AM) technologies are used to generate and optimize design models (through rapid prototyping) as a proof of concept before actual product fabrication. Through this processes, prototypes and/or fully functional parts can be generated using different material including polymers, metals, ceramics, and composites etc. However, some of these parts (for example from non-structural resins) have inferior mechanical properties compared to conventionally manufactured ones. This may be due to intrinsic material properties, choice of AM process and associated process parameters, and the post process operations. Therefore, materials and AM process must be carefully selected to yield requisite properties, in addition, proper post process treatment must be carried out to improve on these properties to suit design specifications. In the present work, high-performance materials including CFR-ABS composites, 18Ni (300-grade) maraging and SUS316L stainless steels were processed through fused deposition modelling and selective laser melting, respectively. The purpose was to optimise the FDM and SLM process parameters, so as to obtain high-quality FDMed/SLMed products. The main results obtained in the present research can be summarized as follows.

Chapter 1 described the background of present research highlighting the limited literature on surface roughness and process parameter optimization on high-performance materials (such as CFR-ABS composites, super alloys and Ni, Co rich alloy materials processed by laser sintering). In order to supplement this deficit, it was proposed to investigate the influences of different processing parameters on CFR-ABS composite and 18Ni (300-grade) maraging and SUS316L stainless steels, respectively processed through FDM and selective laser melting (SLM) with a view to optimise them. In addition, different additive manufacturing technologies, processes/methods, materials, challenges, and gaps

have been discussed. The purpose of the present research was to determine the effect of the various printing process parameters on the quality of the product, and to identify the optimum process parameters and material properties for applications in FDM of carbon fiber reinforced plastic composites and SLM of 18Ni (300-grade) maraging and SUS316L stainless steels.

In Chapter 2, the effects of process parameters such as printing speed, layer thickness, and raster direction on the microstructure and mechanical properties of 3D printed ABS and CFR-ABS materials have been investigated. It was found that low and high printing speed resulted in low tensile strength and ductility while small layer thickness resulted in high tensile strength. However, increasing the layer thickness led to a decrease in both tensile ductility and strength. In addition, specimens printed at a raster direction of zero degree (0°) had better mechanical properties compared to those at 45° and 90°. Reinforcing the ABS material with carbon fiber led to better dimensional stability, decreased tensile strength, and onset of brittleness. The best printing conditions were found to be printing speed of 3200 mm/min, layer thickness of 0.1 mm, and raster direction of zero degrees (0°). This resulted in relatively high tensile strength of 55.86 MPa and 49.03 MPa for 3D printed ABS and CFR-ABS specimens respectively. Specimens printed at a raster direction of 0° exhibited ductile rupture dominated by dimples while those printed at raster direction of 45° and 90° had brittle rupture characterized by quasi-cleavages. In addition, entirely brittle fracture is observed for all specimens printed with CFR-ABS material.

In Chapter 3 optimization of selective laser melting parameters has been extensively deciphered. The influences of various process parameters including laser power, scan speed, pitch, and spot diameter on densification behavior, surface morphology, microstructure, and mechanical properties of selective laser melted (SLMed) maraging steel have been investigated. A process map for the SLM of maraging steel has been constructed. There exists a relatively large processing window, where sound products with relatively high relative

density and good surface quality can be obtained. For example, the optimum process conditions were found to be scan speed of 700 mm/sec, laser power of 300 W, overlap rate of 40%, and energy density of 71.43 J/mm^3. These resulted in a maximum relative density of 99.8% and good surface quality with a roughness value of Ra= 35 μm.

Chapter 4 focused on the influence of post heat treatment on microstructure and mechanical properties of maraging steel. As-built specimens contained martensite matrix with trace amount of austenite phase. The quantity of austenite phase increased during aging treatment due to reversion of martensite to austenite. Solution treatment/aging resulted in elimination of the austenite phase and formation of intermetallic precipitates in the martensite matrix. The as-built and aged specimens exhibited almost the same average grain size, while solution treatment/aging resulted in grain growth of the martensite matrix and a significant change in grain orientation. The results indicated that the SLMed specimens with the building direction parallel to the loading direction had much lower elongation than those with the building direction perpendicular to the loading direction. The maximum tensile strength and hardness obtained were 2033 MPa and 618 HV respectively, after solution treatment at 820 °C for 1 h and aging at 460 °C for 5 h.

Finally, in Chapter 5, process parameters including laser power, scan speed, pitch, and spot diameter were varied and their effects on relative density, surface quality, microstructure, and hardness of SLMed SUS316L stainless steel were established. The optimized process parameters that resulted in high-quality SLMed products with relative density of 99.2%, surface roughness of 9.95 μm, micro-hardness of 241 HV were found to be; Laser power of 320 W, scan speed of 700 mm/sec, overlap rate of 40%, and energy density of 77.92 J/mm^3. These results were summarized in a process map which could provide instructions in choosing proper process parameters for subsequent SLM of SUS316L stainless steel parts.

Therefore, the optimized process parameter on 3D printing of CFR-ABS composites and SLM of 18Ni maraging and SUS316L stainless steels, and the generated process maps for maraging and SUS316L steels will contribute new knowledge towards a comprehensive material property database and testing methodology on FDM and SLM as key AM processes.

Recommendations for future work

For this study, further experiments on process parameter during FDM of CFRP-Composites with different weight percentages (wt%) and investigate how this affects the mechanical properties are recommended.

In general, nearly all 3D printing machines as well as designs treat each layer of powder the same without giving considerations to thermal properties of the powder and structural requirement of the design. In an ideal situation, different layers would demand different laser scanning speeds and powders since the powder environment changes as the layer-by-layer build up proceeds. For a more robust process control and optimization of 3D printing process, the future focus should be on how to process a 3D part by instructing the machine on the right powder and laser parameters for each layer. In addition, more emphasis should be put on the in-situ measurement of temperature, cooling rate, and residual stresses in order to command the machine to adjust the process parameters to conform to design specifications.

Achievements

Journal publication

1. James Mutua, Shinya Nakata, Tetsuhiko Onda, Zhong-Chun Chen, Optimization of Selective Laser Melting Parameters and Influence of Post Heat Treatment on Microstructure and Mechanical Properties of Maraging Steel. *Material & Design.* Vol. 139, 5 Feb. 2018, Pages 486-497.
2. James Mutua, Souhei Yamane, Tetsuhiko Onda, Zhong-Chun Chen, Microstructure and Mechanical Properties of 3D Printed Carbon Fiber Reinforced Plastic Composites. *Composite Science and Technology.* To be published.
3. James Mutua, Souhei Yamane, Tetsuhiko Onda, Zhong-Chun Chen, Process Optimization and Mechanical Properties of 18Ni Maraging Steel Fabricated by Selective Laser Melting. To be published
4. James Mutua, Souhei Yamane, Masahiro Hayashi, Tetsuhiko Onda, Zhong-Chun Chen Optimization of Selective Laser Melting Parameters and their Influences on Microstructure and Hardness of SUS316L Stainless Steel. To be published

International conferences

1. James Mutua, Nakata, S., Akao, T., Onda, T., and Chen, Z., 2017. Influences of processing parameters on microstructure and mechanical properties of SLMed maraging steel. In *4th International Conference on Powder Metallurgy in Asia APMA2017 Proceedings.* Hsinchu, Taiwan.
2. Shinya Nakata, James Mutua, Takahiro Akao, Tetsuhiko Onda, Zhongchun Chen, Effects of Processing Parameters on Microstructure and Mechanical Properties of Maraging Steel Fabricated by Laser Additive Melting. *The 6th Joint Symposium on Mechanical and*

Materials Engineering between Northeastern University and Tottori University, Sept. 2016, Tottori, Japan.

Domestic conferences

1. Souhei Yamane, James Mutua, Shinya Nakata , Tetsuhiko Onda, Zhongchun Chen, Additive Manufacturing of Maraging Steel Using 3D Printer. *60th Japanese Steel Association and 57th Chugoku Shikoku Branch Meeting of Japan Institute of Metals and Materials*, Aug. 2017, Kochi, Japan.
2. James Mutua, Shinya Nakata, Souhei Yamane, Tetsuhiko Onda, and Zhongchun Chen, Selective Laser Melting, Microstructure, and Mechanical Properties of Maraging Steel. *The 2017 Japanese Spring Conference for the Technology of Plasticity,* June 2017, Gifu, Japan.
3. James Mutua, Shinya Nakata, Souhei Yamane, Tetsuhiko Onda, Zhongchun Chen, Microstructure Evolution and Mechanical Properties of Selective Laser Melted Maraging Steel. *Spring Meeting of Japan Society of Powder and Powder Metallurgy*, June 2017, Waseda-Tokyo, Japan.
4. Shinya Nakata, James Mutua, Souhei Yamane, Takahiro Akao, Tetsuhiko Onda, Zhongchun Chen, Additive Manufacturing of Maraging Steel Using 3D Printer. *H28 Chugoku Shikoku Branch Meeting of the Japan Society for the Technology of Plasticity*, Dec. 2016, Okayama, Japan.
5. James Mutua, Shinya Nakata, Takahiro Akao, Tetsuhiko Onda, Zhongchun Chen, Effects of Processing Parameters on Surface morphology &Microstructure of 18Ni Maraging Steels Fabricated by Additive Manufacturing. *Annual Autumn Meeting of the Japan Institute of Metals and Materials*, Sept. 2016, Osaka, Japan.

6. Shinya Nakata, James Mutua, Souhei Yamane, Takahiro Akao, Tetsuhiko Onda, Zhongchun Chen, Effect of Processing Parameters on Microstructure and Hardness of Maraging Steels Fabricated by Laser Additive Manufacturing. *Annual Autumn Meeting of the Japan Institute of Metals and Materials*, Aug. 2016, Shimane, Japan.
7. James Mutua, Shinya Nakata, Takahiro Akao, Tetsuhiko Onda, Zhongchun Chen, Effects of Processing Parameters on Densification Behavior and Microstructure of Maraging Steels Fabricated by Laser Additive Manufacturing. *Annual Spring Meeting for Powder and Powder Metallurgy*, June 2016, Kyoto, Japan.

Acknowledgements

This research would not have been possible without the extraordinary genius of Professor Zhong-Chun Chen. I am indebted to him for giving me the chance to study with him. Under his steadfast guidance, advices, and discussions the foundation and success of this work was established. More importantly, his care and help saw me through the three years of foreign life.

I would like to thank Dr. Tetsuhiko Onda for his invaluable suggestions and assistance in conducting some of the experiments. My special thanks also goes to Mr. Yasuhide Nishimura of Kurayoshi Institute of Technology for his experimental help and fruitful discussion.

To my fellow graduate students in *Laboratory of Materials Engineering*, *Tottori University* thank you all for providing a cohesive research family. Especially MSc. Candidates Mr. Shinya Nakata and Mr. Souhei Yamane, I greatly treasure your assistance both in my research and wellbeing throughout the study period.

I am really obliged to JICA and Amada Foundation for the financial support which made the research a success. Shimane University, Yonago Industrial Technology Center, and Industry Personnel Training Center-Kurayoshi cannot go unmentioned for their technical support they offered to me in executing the practical part of the research, I amiably say thank you.

In a special way, I sincerely thank my family especially my dear wife Jane Kavata and our beloved children Sheila Ndanu Mutuku and Abel Muuo Mutuku, my mother, father, brother and sisters. Thank you for being at my side despite the distance always offering prayers, love, and support throughout the research period.

Finally, I humbly thank the almighty God for always giving me the strength to strive for the best and persevere against all odds.